Engineering a Physical Microenvironment to Control Stem Cell Fate and Function through Mechanical Cues

van Boekel, D.W.G.

Award date:
2021

Graduation Project

Final Report

Engineering a Physical Microenvironment to Control Stem Cell Fate and Function through Mechanical Cues

Master	Manufacturing Systems Engineering
Department	Mechanical Engineering
Research Group	Microsystems/Neuro-Nanocale Engineering
Student	Daan van Boekel
Identity Number	0895893
Thesis Supervisor	dr. Regina Luttge
Date	August 18, 2021

Eindhoven, August 18, 2021

Contents

1 Introduction **1**

2 Background **2**
2.1 Neuronal Networks and Mechanotransduction . . . 2
2.1.1 Introduction . . . 2
2.1.2 Polarization and Network Formation . . . 2
2.1.3 Cytoskeleton and Nucleoskeleton . . . 3
2.1.4 Mechanical Cues . . . 4
2.1.5 Mechanosensing . . . 4
2.1.6 Conclusion . . . 5
2.2 Alzheimer's Disease . . . 6
2.2.1 Introduction . . . 6
2.2.2 Cure Development . . . 6
2.2.3 Conclusion . . . 7
2.3 Brain-on-Chip . . . 7
2.4 Conclusion . . . 8

3 Designing and Fabricating Mechanical Cues in 3D Micropores **9**
3.1 Introduction . . . 9
3.2 Alzheimer's Disease Assay - a Mechanotransduction Approach . . . 9
3.3 Mechanical Cue Configurations and Fabrication Process . . . 10
3.4 Configurations of Patterns . . . 10
3.4.1 Approach of Design . . . 10
3.4.2 Selection of Configurations . . . 12
3.4.3 Fabrication . . . 13
3.5 Results . . . 14
3.5.1 Laser Ablation from the Front . . . 14
3.5.2 Laser Ablation from the Rear . . . 14
3.5.3 Laser Ablation from Two Sides . . . 15
3.5.4 Size of the Through Hole . . . 16
3.6 Conclusion . . . 16

4 Numerical Modelling of Mechano-Induced Stress in Cells **17**
4.1 Introduction . . . 17
4.2 Modeling Approach . . . 17
4.2.1 Cell Models in Literature . . . 17
4.2.2 Modeling Software . . . 18
4.2.3 Continuous Cell Model . . . 18
4.2.4 Tensegrity Cell Model . . . 19
4.2.5 Determining the Mechanical Properties of the Cell Elements . . . 20
4.2.6 Modeling the Micropores . . . 22
4.3 Results . . . 23
4.3.1 Micropores Ablated from the Front versus from the Rear . . . 23
4.3.2 The Tensegrity Structure in Concavity . . . 24
4.3.3 Method for Dividing the Configurations . . . 25
4.3.4 Divided Configurations . . . 26
4.4 Conclusion . . . 28

5 Application of the Numerical Model **29**
5.1 Introduction . . . 29
5.2 Simulation Results . . . 29
5.2.1 Conical . . . 29
5.2.2 Chessboard-like . . . 29

5.2.3 TopoChip . . . 30
5.2.4 Grooved Substrate . . . 31
5.3 Conclusion . . . 32

6 Discussion **33**
6.1 Towards a BoC Device for Single Cell Analysis & Cell Fate Control . . . 33
6.2 How the Results of this Study can Benefit AD Treatment Development . . . 33
6.3 What the Results of this Study Mean for the Future of the Microsieve . . . 35

7 Conclusion & Recommendations **36**

Bibliography **37**

A Appendix A **43**
A.1 Hydrodynamics . . . 43
A.2 Microsieve Electrode Array . . . 44
A.3 Alternative Methods for Electrical Measurements in Microsieves . . . 46

B Appendix B **47**
B.1 Cell Fate Control in Practice . . . 47
B.1.1 Nanogrooves . . . 47
B.1.2 Patterning of Cell Adhesion Molecules . . . 47
B.1.3 Physical Confinement . . . 48
B.1.4 Aligned Nanofibers . . . 48
B.1.5 Topochip . . . 49
B.2 Micropatterning the Substrate Surface . . . 49
B.3 Lab-Scale Manufacturing Process Overview . . . 50
B.4 Manufacturing Process Time Estimates . . . 51
B.5 Production Units . . . 52

C Appendix C **54**
C.1 Material Properties in Literature . . . 54
C.1.1 Membrane . . . 54
C.1.2 Cytoplasm . . . 54
C.1.3 Nucleus . . . 54
C.1.4 Microtubules . . . 54
C.1.5 Actin Filaments . . . 55
C.1.6 Intermediate Filaments . . . 55
C.1.7 Nuclear Lamina . . . 55
C.1.8 Chromatin . . . 55

D Appendix D **56**
D.1 Micropore Without Ablation . . . 56
D.1.1 Unablated Configuration . . . 56
D.2 Micropores with One Ablation . . . 57
D.2.1 Configuration FM . . . 57
D.2.2 Configuration FE . . . 57
D.2.3 Configuration FS . . . 57
D.2.4 Configuration RM . . . 58
D.2.5 Configuration RE . . . 58
D.2.6 Configuration RS . . . 58
D.3 Micropores with Two Ablations . . . 59
D.3.1 Configuration F2_1 . . . 59
D.3.2 Configuration F2_2 . . . 59
D.3.3 Configuration F2_3 . . . 59

D.3.4 Configuration F2_4 . . . 60
D.3.5 Configuration R2_1 . . . 60
D.3.6 Configuration R2_2 . . . 60
D.3.7 Configuration R2_3 . . . 61
D.3.8 Configuration R2_4 . . . 61
D.4 Micropores with Three Ablations . . . 62
D.4.1 Configuration F3_1 . . . 62
D.4.2 Configuration F3_2 . . . 62
D.4.3 Configuration F3_3 . . . 62
D.4.4 Configuration F3_4 . . . 63
D.4.5 Configuration F3_5 . . . 63
D.4.6 Configuration F3_6 . . . 63
D.4.7 Configuration F3_7 . . . 64
D.4.8 Configuration F3_8 . . . 64
D.4.9 Configuration R3_1 . . . 65
D.4.10 Configuration R3_2 . . . 65
D.4.11 Configuration R3_3 . . . 65
D.4.12 Configuration R3_4 . . . 66
D.4.13 Configuration R3_5 . . . 66
D.4.14 Configuration R3_6 . . . 66
D.4.15 Configuration R3_7 . . . 67
D.4.16 Configuration R3_8 . . . 67
D.5 Micropores with Adjusted Position of the Edge Ablation . . . 68
D.5.1 Configuration FFE . . . 68
D.5.2 Adjusted Configuration RRE . . . 68
D.5.3 Configuration RR2_1 . . . 68
D.5.4 Configuration R2_3 . . . 69
D.5.5 Configuration R3_1 . . . 69
D.5.6 Configuration R3_3 . . . 69
D.5.7 Configuration RR3_5 . . . 70
D.5.8 Configuration RR3_7 . . . 70
D.6 Chessboard-like Topographies . . . 70
D.6.1 ch4 . . . 71
D.6.2 ch10 . . . 71
D.6.3 ch12 . . . 71
D.6.4 ch14 . . . 72
D.6.5 ch16 . . . 72
D.6.6 ch18 . . . 72
D.6.7 ch20 . . . 73

1 Introduction

In 2019, about 50 million people suffered from dementia worldwide [1], which means someone is diagnosed with the neurodegenerative disease every 3 seconds [2]. In 2050, this number is expected to be between 105-150 million, which corresponds to 1 in 85 people [3]. Besides the social impact that this has on society, there are also significant financial consequences. The annual societal costs of dementia are estimated to be around 600 billion USD, which is approximates 1% of the worlds gross domestic product [4, 5]. With the amount of patients doubling or even tripling between now and 2050, these costs will also keep rising. Even though Alzheimer's disease was already first described by Alois Alzheimer in 1906 [6], no cure has been found to date. This is because current animal models are inaccurate, expensive and unethical [7] and the brain is in general one of the least understood organs in the human body [8]. As a result, the failure rate for clinical drug trials for AD is 99.6% [7]. By using Brain-on-Chip devices, it is possible to mimic the behaviour of the human brain *in vitro* and potentially make better predictions about the efficacy of a drug or treatment, even before the clinical trials. Such devices do not only help to increase our understanding of the human brain, but they can lead to a significant cost reduction in the process of researching drugs for Alzheimer's disease.

The particular Brain-on-Chip on which this research focuses is the microsieve. Using this device, it is possible to capture single cells in a pyramid-shaped micropore, such that the cells keep their 3D morphology. One such microsieve consists of a structured array of many micropores, so the cells can connect to each other. Using microfabrication to change the shape of the micropore, a mechanical cue could be applied to the cell, influencing the direction in which it will form connections. By doing so, similar cell structures can be created each time, which reduces the amount of changing variables when researching the effects of drugs and brain cells in general.

Although it is known that topographical cues influence the intracellular process and eventually its morphology, it is not yet known how this happens exactly. There are indications that cells most likely form connections from the point where they experience the most stress [9, 10]. Therefore, the fabrication process of a NOA81 microsieve as introduced by Moonen et al. [11] and improved by Sabahi-Kaviani and Luttge [12], was analysed to find out how the topography of the micropores could be changed to give mechanical cues to the cell. So, the research question was stated as follows:

> *How can the NOA81 microsieve, as introduced by Moonen et al. [11] and improved by Sabahi-Kaviani and Luttge [12], be produced with the quality parameters as such that the micromechanics in the micropore can control cell fate?*

This thesis is structured to answer the research question in the following manner. First in Chapter 2, the background literature on neurons and network formation, Alzheimer's disease and Brain-on-Chip is presented. Next, Chapter 3 will explain how mechanical cues can influence the cell's morphology. This is then linked to the fabrication process of the NOA81 microsieve, by examining where in the process there is room for changing the topography of the micropore. Currently, this microsieve is fabricated using a combination of replica molding and laser ablation. It was found that the laser ablation step was the most appropriate way in our lab for influencing the topographical cues of the micropore. So several topographies for the micropore were selected and fabricated. To probe the most suitable configurations of the multiple options without running cell experiments, a 3D finite element model of a cell was created. In Chapter 4, it is explained how this model was made and of what components it consists. This cell model was then applied to the micropores with different topographies and the results are presented. In Chapter 5, the model is applied to other geometries than micropores, to see how it responds to those. Finally in Chapter 6, it is discussed what the results mean and in Chapter 7 the conclusions and recommendations are given.

2 Background

In this Chapter, the relevant background literature is summarized and probed in order to provide insight in the knowledge gap in the state of the art with respect to the application of mechanical cues controlling stem cell fate and function in Alzheimer disease (AD) *in vitro* models. First, a general introduction about neurons, network formation and mechanotransduction is given. Then, AD and the problems in finding a cure are introduced. Novel approaches to solve these problems are rising by means of Brain-on-Chip technology. Among several engineering directions in the design of advanced brain models, like organoids [13] and microfluidic channel structures (e.g. Mimetas [14]), one such system considers the culture of neurons in a grid of 3D micropores, whereas the connections of the neurons are supported and formed across a simple 2D culture substrate, i.e. a microsieve. The main developments taking place in Brain-on-Chip will be discussed and briefly introduce the microsieve technology for the design of a neuronal cell culture assay.

2.1 Neuronal Networks and Mechanotransduction

2.1.1 Introduction

In the human brain, approximately 86 billion neurons are present. These transmit and receive electrical and chemical impulses and thereby form the communication and computation network of the brain. The biologically evolved functionality of mammalian brain is technically unprecedented but emulating smaller neuronal circuits either *in silico* or *in vitro* is a growing research field [15]. The basic element of such circuits are neurons. In nature, neurons generally consist of four main parts: the cytoskeleton (see Section 2.1.3), the soma, multiple dendrites and one axon. The soma forms the body of the cell, at the dendrites the neuron receives signals from other neurons and via the axon the neuron can send signals (Figure 2.1). The axons and dendrites contact each other at the synapses. Here, in a 20-40 nm wide gap between the two, electrical signals from the axon are converted into chemicals called neurotransmitters [16]. Stem cells forming into neurons start out without axons and dendrites, these develop in a process called polarization [17].

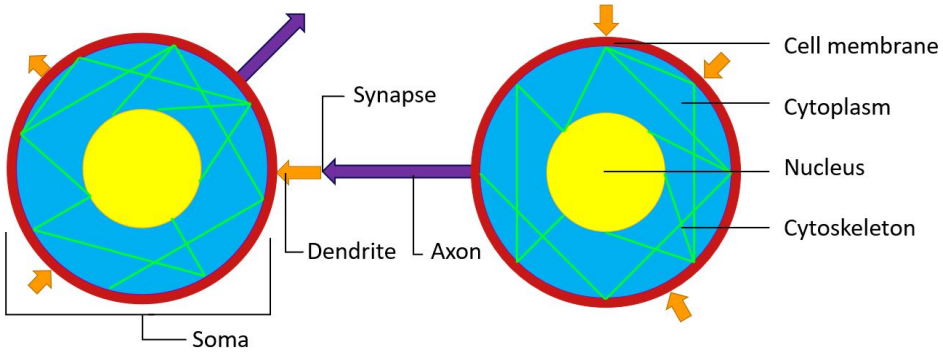

Figure 2.1: Schematic image of a neuron with the soma, consisting of the cell membrane (red), cytoplasm (blue) and nucleus (yellow). The axons (purple) connect to the dendrites (orange) and the synapse. The cytoskeleton is show in green.

2.1.2 Polarization and Network Formation

The process of polarization is the process of a neuron forming one axon and multiple dendrites. In a dissociated neuron without any external influences, this process is stochastic. However, using external cues, this process can be influenced, see Section 2.1.4. In the literature, neural polarization is described as a process consisting of five steps [18]:

1. After making contact with a surface, a cell adheres to it by forming its lamellipodium (a dense network of actin filaments).
2. From the lamellipodium, in some hours several neurites emerge.

3. The neurites grow at similar speeds, until after approximately 24h the symmetry is disrupted and one grows longer than the rest. This neurite will become the axon, while the other neurites stop growing or shrink.
4. Over the course of a week, the remaining neurites turn into dendrites.
5. The axon matures further and forms synapses with the dendrites or axons of other neurons.

Axons can vary in length over several length scales up to a meter. When growing and forming new connections, they are guided by so-called guidance proteins, which either attract or repel the axon. The axon can detect these proteins using the growth cone at the tip of the axon. For part of its path the axon is usually part of an axon bundle, which is a strand of axons of different neurons [19].

2.1.3 Cytoskeleton and Nucleoskeleton

Just like humans have bone skeletons, cells themselves also have skeletons. Such a cytoskeleton (literally *cell skeleton*) gives structural support, facilitates movement of, and supports transport within the cell. The three main components of the cytoskeleton (CSK) are actin filaments, microtubules and intermediate filaments (IFs) [20].

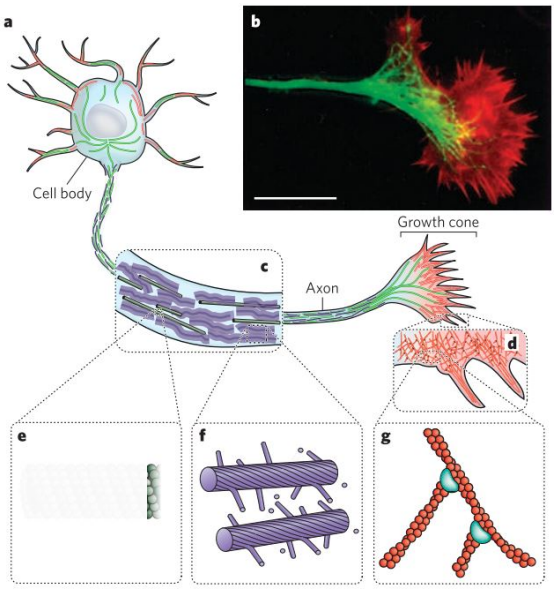

Figure 2.2: The cytoskeleton a) Neuron with microtubules (green), intermediate filaments (purple) and actin filaments (red) b) Fluorescence optical micrograph of a growth cone c) Schematic close up of the axon and its components d) Schematic close up of the growth cone with its actin filaments e) Schematic close up of a microtubules, showing its hollow tube structure f) Enlarged schematic drawing of the intermediate filaments g) Enlarged schematic drawing actin filaments arranged in a network [21].

The actin filaments are important for movement and change of the cell shape. Also, they help the cell adhere to a substrate through the lamellipodium. The microtubules form the transport network of the cell. The intermediate filaments are stable structures, which give the cell its mechanical properties, make it capable of withstanding tension and most importantly they anchor the nucleus. In the nucleus, a similar structure as the CSK is present: the nucleoskeleton (NSK). The proteins that make up the NSK, mainly lamina and chromatin, determine the mechanical properties of the nucleus [22].

2.1.4 Mechanical Cues

The CSK is of importance for the morphology of cells, but external influences also play a role. The behaviour of a cell can be altered through influences of its microenvironment. External mechanical influences on a cell can be grouped into four categories [9]:

1. **Compressive or tensile stress:** *in vivo*, cells maintain a force balance induced by external forces from the ECM and other cells, which are internally countered by the CSK. These forces change the cell shape and thereby stimulate expression of certain genes and resultingly cell behaviour [23].
2. **Substrate stiffness:** tissues in the human body vary greatly in mechanical properties, stiffnesses range from 1 kPa (brain tissue) to 100 kPa (calcified bone) [24]. So unsurprisingly, substrate stiffness also influences the cell shape and behaviour of the cell (Figure 2.3).
3. **Dynamic shear stress:** such shear stress can be present in both solid and liquid tissues. Examples of the first are in bending of bones and of the latter in vascular systems. With tissues damage, shear stress steers cells towards the injury and makes them react appropriately [25].
4. **Substrate topography:** the features of the ECM vary from nanometers to centimeters in size. Stem cells sense these topographical features and regulate their behaviour accordingly. There has also been shown that surface topography plays an important role in the alignment of neuronal outgrowths [26, 27].

Influences on the behaviour include migration, proliferation, differentiation, gene expression, and apoptosis [28]. *In vivo*, this means that the ECM influences the behaviour of all cells, so also neurons [29]. By simulating certain cell microenvironments using for example polymers, the differentiation of stems cells can be influenced [30]. The study of mechanobiology specializes in how cells sense and react to external forces and how these mechanical cues are transformed into chemical activity within a cell, respectively called mechanosensing and mechanotransduction [31].

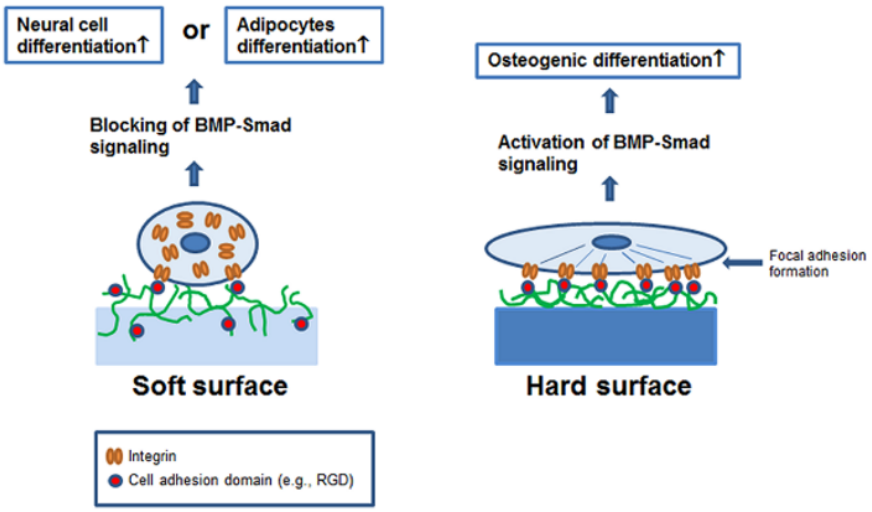

Figure 2.3: The influence of substrate stiffness on cell morphology visualized. On a hard surface the cell will try to pull harder on the environment and thereby flattens, while on a soft surface the cell has a rounder morphology [30].

2.1.5 Mechanosensing

As described in Section 2.1.4, cells are influenced by their microenvironment. So far this has been made out as a passive process, but cells actually actively probe their environment in a process called mechanosensing. All cells form their morphology based on many intermediate decisions, which are in their turn based on testing of and reacting to its microenvironment. Cells periodically form a sensory module, which takes in the order of minutes to determine the rigidity of the microenvironment [28]. This can be triggered by cell

stretching or other types of physical activity, hormones and cycles within the cell. Through integrin, a protein which facilitates cell-ECM adhesion, cells apply forces to their microenvironment. Depending on stiffness of the matrix, the morphology of the adhesions and also the polymers within the cell will change and thereby influence the morphology of the entire cell. This cycle of activation, effectors working, mechanotesting and mechanoresponse as shown in Figure 2.1.5, repeats itself until a steady state is achieved. This morphology in its turn determines gene expression and cell behaviour.

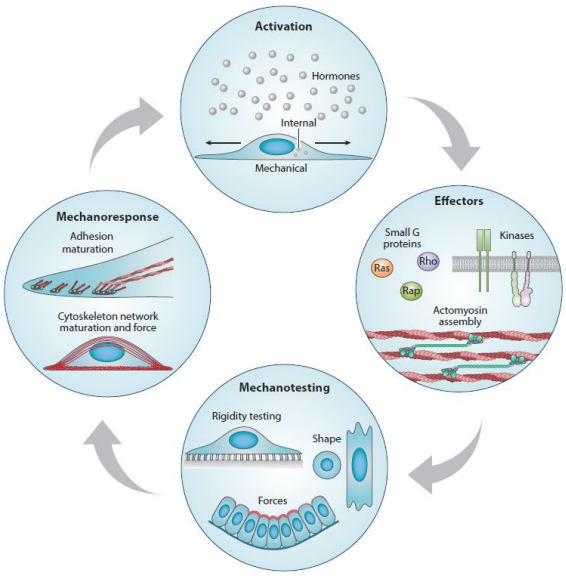

Figure 2.4: In this diagram, the mechanosensing cycle is shown. Usually, intrinsic processes *activate* the start of morphology changes in cells. Then, through different biochemical *effectors* (actomyosin, kinases and G proteins), the cells tug on the ECM or neighboring cells, in a process called *mechanotesting*. The result of such a test will initiate a *mechanoresponse* in the cells, changing its morphology. This cycle repeats until a steady state of the cells morphology is achieved. One such cycle generally takes in the order of 10 minutes [28].

Unfortunately, there is still only a basic understanding of mechanosensing processes, and their influence on cell morphology. Particularly the mechanoresponse step requires an elaborate understanding of the intracellular processes. Moreover, in a few hours, many cycles occur after one another which all contribute to the development of the cell. The be able to understand the processes within a cell which determine its final morphology, extensive monitoring of the intracellular processes is required. Each of the many cycles a cell goes through before reaching its steady state after a few days would have to be understood. This would require monitoring of the morphology, forces, biochemical processes, adhesions etc. over a period of multiple days.

2.1.6 Conclusion

Neurons are an important part of the communication network of the brain. In the polarization process, there is determined which outgrowth will form the outgoing connection (axon) and which the incoming connections (dendrites). The CSK is internally important for the morphology of the cell, but external influences play a role as well. Forces from the ECM, can change the cell shape and stimulate gene expression. Other factors which induce such *mechanical cues* are substrate stiffness, dynamic shear stress and surface topography. Cells sense their environment through a process called mechanosensing, which is a process that repeats itself until a steady state is reached. By controlling the physical microenvironment of a cell, the mechanical cues can be used to influence the cell such that the polarization process happens in a certain way or that specific genes are expressed, which has been explored in this project.

2.2 Alzheimer's Disease

2.2.1 Introduction

AD is a brain disorder which is characterized by progressive dementia, changes in behaviour and mood swings [32]. AD is strongly linked to age, 90% of cases occur in patients aged 65 or over [33]. The average life expectancy of AD patients is on average 8-10 years after the diagnosis. However, someone may already suffer from AD long before the first signs show.

In AD, the intricate neuronal network is disrupted. The exact workings of this neurodegenerative disease remain unclear, but it is known that two things play a major role in its progression: plaques and tangles (Figure 2.5) [34]. Plaques are deposits of β-amyloid-protein (Aβ), which stick together. These deposits block communication between cells and trigger immune reactions. Tangles are aggregates of the protein tau. Normally these proteins help to stabilize the microtubules, but in AD, the tau molecules form tangles which block, and later even disintegrate the microtubules. In the end, this leads to cell death [35, 36]. One approach to elucidate the mechanisms and potential therapeutic means of this disease is using *in vitro* biology as envisaged in this thesis.

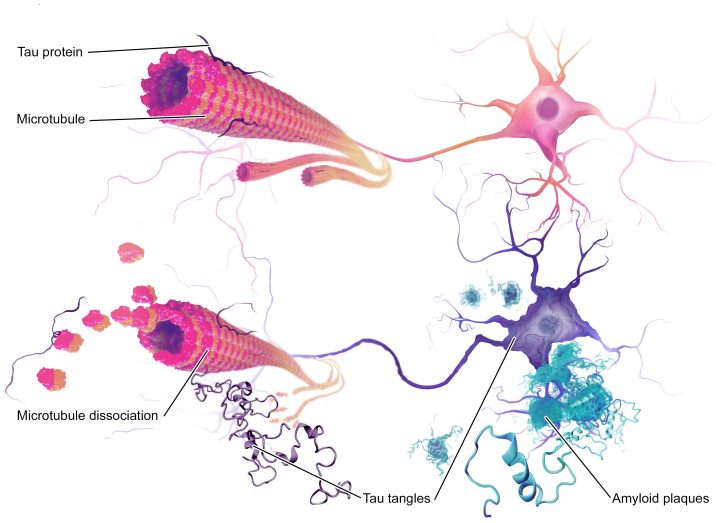

Figure 2.5: Two neurons and their connection. The upper neuron in healthy condition, while in the lower the impact of AD can be seen in the form of plaques and tangles [37].

2.2.2 Cure Development

AD was first described by Alois Alzheimer in 1906 [6]. Yet, despite its large social and financial impact on society and its severe symptoms, no cure has been found to date. There are several factors which contribute to this:

1. Generally, in the preclinical phase *in vitro* test are done using 2D cell culture systems and *in vivo* tests are done in animals. With *in vitro*, 2D and even 3D cell cultures do not accurately replicate the complex physical environment. Moreover, animal test are expensive, unethical and do not accurately predict the outcome in human trials [38, 39, 27]. It is also not possible to fully predict toxicity and efficacy of drugs using animal models, demanding carefully planned clinical trials [7].
2. The human brain is very complex and one of the least understood organs in the human body. For disorders of the central nervous systems (CNS), there is little pathophysiological understanding of the conditions. This makes targeting the correct molecules and treating the disease via a pharmaceutical approach difficult [8].
3. Placebos play an important role in CNS trials. Improvements in memory or mood are subjective and difficult to quantify. Also, the effects are difficult to differentiate from the effects of therapy [40].

4. The blood-brain-barrier (BBB), forms a highly selective semipermeable border to the CNS. Its high selectivity is responsible for issues in drug penetration. Drugs with promising early results are often unable to cross the BBB. In fact, 100% of large molecule drugs cannot cross this border and this number is 98% for smaller molecule drugs [41].

All of this often results in failure in the clinical phase after success in the preclinical phase [42]. Between 2002 and 2012 the failure rate of drug development for AD was 99.6% [7]. Moreover, current treatments only alleviate the symptoms, but they do not target the underlying cause [43]. Altogether, the pharmaceutical industry has spent over 3.5 billion USD in AD research to date [8].

2.2.3 Conclusion

These numbers - the amount of people suffering from dementia and the corresponding cost - suggest a high medical need for an improvement of the treatment of AD patients. This comprises better detection of the disease, being able to slow down its progression or curing the disease altogether. Currently, animal models are unable to accurately model the effects of new drugs in development, therefore, making the development of new drugs financially unattractive. Hence, there is an urgent request for novel systems that describe the disease and prematurely test drug efficacy *in vitro*.

2.3 Brain-on-Chip

Brain-on-Chip (BoC), or more generally speaking, Organ-on-a-Ohip (OoC) technology can be seen as the next big step in cell culturing technologies. Conventional 2D cell cultures in e.g. petri dishes stem from almost a century ago and are limited when it comes to accurately predicting *in vivo* results and they do not allow tissue-specific functions of many cell types [44, 45]. *In vivo*-like cell cultures have connections and interactions coming from all three dimensions, which creates a very different system. Because of the lack of extracellular scaffolding, cells do not form tissue-like structures on hard 2D surfaces [46].

Their successor, 3D cell culturing, though already 50 years old [44], incorporates more functionality [47]. By using hydrogels, networks of polymers swollen by water absorption, the effect of the extracellular matrix (ECM) is replicated. As mentioned in Section 2.4, the ECM is the structure around the cells which is present in all forms of tissues. It is responsible for the physical scaffolding of cellular constituents and of importance for many processes [48]. With this in mind, the two main improvements are achieved in mimicking *in vivo* drug responsiveness and tissue function [49]. However, this technique still lacks when it comes to tissue-tissue interface functionality, which is crucial for nearly all organ and disease models. Also, normal mechanical effects like shear and pressure are not incorporated yet. Moreover, mechanistic observations of tissue-scale phenomena probed at the level of a single cell within its unique cellular microenvironment are not easily possible with 3D cell culturing technologies. Finally, the interaction between blood and immune cells cannot be studied accurately without the presence of fluid flow [50]. OoCs use microfluidics and can thereby better emulate tissues by incorporating essential parts of the vasculature, too, and allow for other types of controlled manipulations such as applying shear. Overall, these efforts can help to overcome the limitations of established 2D and 3D cell culturing methods.

OoCs can be described as microfluidic culture devices containing living cells in the form of tissue structures, which synthesize one or more organ functions for *in vivo* testing purposes [51]. By linking more than one OoC, more complex pathophysiological studies can be done. Current applications of OoCs already simulate the arteries, spleen, BBB, kidney, lung, gut, heart, liver and brain [52, 53].

Among the different types of BoCs, the microsieve offers a novel route to handle neurons in culture (Figure 2.6). A microsieve is a passive mechanical structure with 3D micropores in each of which one cell can be trapped using microfluidic action [54, 55], see Appendix A.1. By trapping these cells in the 3D micropores, the cells are in a controlled configuration with a defined distance and organization. It facilitates experiments which require high spacial control [56].

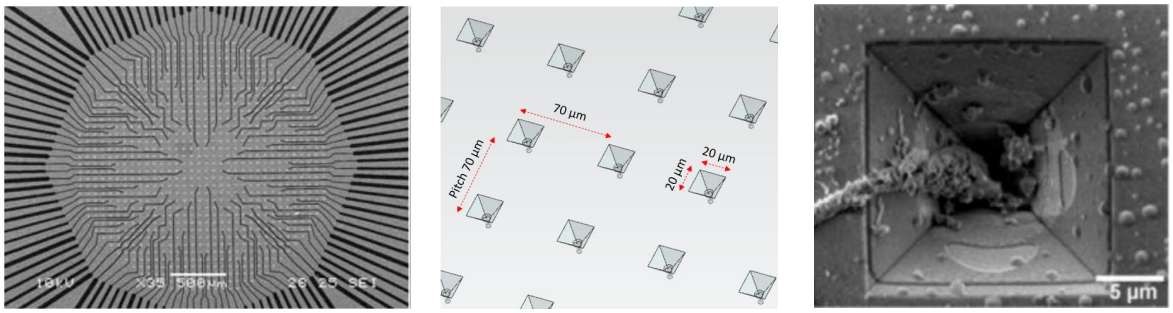

(a) Microsieve electrode array [39]. (b) 3D model microsieve. (c) SH-SY5Y cell in micropore [57].

Figure 2.6: Overview of the µSEA created by Schurink et al.

A microsieve electrode array (µSEA) was designed and fabricated by Schurink et al. (Figure 2.6a) [39]. The µSEA is discussed in more detail in Appendix A.2. Using this µSEA as a mold Moonen et al. designed a fabrication process for a microsieve made of NOA81 [11], which was then improved by Sabahi-Kaviani and Luttge [12]. NOA81, compared to PDMS (which is often used for cell culturing [58]), has better resistance against organic solvents, is impermeable to air and water vapor, is less prone to swelling upon contact with fluids and surface treatments are more stable [59].

2.4 Conclusion

In Alzheimer's disease, the intricate communication network of the brain is disrupted. There is a basic understanding of the mechanisms that play a role in this neurodegenerative disease, but many steps still have to be taken before the exact workings of the disease are understood and a treatment can be developed. Moreover, the current methods for drug development are inaccurate and expensive.

A novel solution for this problem can be found in the Brain-on-Chip, which is on its ways to replace the current 2D and 3D cell culturing models. In such devices is it possible to change the mechanical cues (compressive/tensile stress, substrate stiffness, dynamic shear stress and substrate topography) such that the gene expression and polarization process of the cell can be influenced. However, the intracellular processes are not well understood yet. So, the influence of each of these mechanical cues on the cell morphology has to be researched more extensively.

To be able to understand the influence of mechanical cues on the cell, it is important to understand how these cues actually effect the cell mechanically. This can be done through experimentation or simulation of the cell in a specific physical microenvironment. Either way, the forces and stresses which act on the cell need to be known to create a complete overview of the mechanosensing process. By first understanding how the processes within a single cell work, it is then possible to understand its role within a network of multiple cells. This brings us closer and closer to also understanding neurodegenerative diseases like Alzheimer's.

3 Designing and Fabricating Mechanical Cues in 3D Micropores

3.1 Introduction

In this Chapter together with Chapter 4, the design process and experimental method used to answer the research question is described. Here, the design process of mechanical cues in 3D micropores and their fabrication are described. The pores form the basic elements of a novel type of microsieve. The aim is to design these topographical features of the microsieve in a repetitive array in such a manner that they collectively control neurite outgrowth's direction in a neuronal cell assay. Consequently, ensembles of the topographical features can give rise to unique connectivity with a stem cell-derived neural network. Next, the state of the art of currently used NOA81 microsieves (Sabahi-Kaviani et al. [12]) is given and how these type of device can be used in Alzheimer's Disease (AD) modelling. The latter results in suggestions for changes in the laser ablation process which are discussed in order to gain systematic variations of mechanical cues. Finally, different configurations of mechanical cues are presented.

3.2 Alzheimer's Disease Assay - a Mechanotransduction Approach

When researching the workings of AD and potential treatments developed by means of *in vitro* drug screening, among many, three aspects are particularly important.

1. Being able to replicate the relevant neuronal process containing hallmarks of AD and being able to distinguish such hallmarks from healthy cultured tissues within the complexity of the biological systems emerging in the dish, when stem cell-derived neurons are employed.
2. Repeatability of experiments with sufficient statistical power.
3. Having a setup which facilitates screening of the relevant hallmarks in a cost-effective manner that is fit for established pharmaceutical workflows in the industry.

The first, second and third can be achieved by using the already existing microsieve (Sabahi-Kaviani & Luttge and potentially similar devices). With a microsieve, it is possible to research single cell behaviour and especially its role within the neuronal network in more detail. However, the workings of the brain are not yet understood and the first aspect is therefore being researched at Neuro-Nanoscale Engineering by means of microsystems, which also led to this master project. One hypothesis is that through *steering* the behaviour of the neurons and their network formation, it will be easier to standardize the culture format. A second hypothesis relates to mechanical cues which influence the cell fate through mechanotransduction.

In the literature, many examples of setups can be found, whereby network formation of neurons is influenced using topographical cues [60, 46, 61, 62, 30]. Appendix B.1 provides an example from the research performed at Neuro-Nanoscale Engineering, which introduces such mechanotransduction processes by means of nanogrooves. Most of these setups steer the direction of the axons once they have already begun growing. While it is also a hypothesis that neurons are bidirectionally polarized on nanogrooves, leading to stratisfying network connectivity also in an aligned fashion on these nanoscale surface features, it is still unknown how the cell induces axon definition from the neurites being grown from the soma during differentiation. By influencing the polarization process of the cell in a 3D spatially locked position, i.e., a micropore, there is hence investigated here, how such a physically engineered microenvironment to control cell fate can be provided. In turn, such simple mechanical patterns will then also potentially improve statistical power by unifying the readout of such microsieve scaffold-assisted assay.

Although the exact workings of intracellular processes are not completely understood yet, there are indications that cells will polarize towards the point of the most stress [9, 10]. This idea is also supported by the knowledge that cells will *pull* stronger on hard surfaces [28, 30], because at the point of the highest stress on the cell membrane, the contact force will be the highest and the cell will experience the surface as being harder and at a local level the surface will be more compressed. Hence, the design process introduced here utilizes the existing NOA81 microsieve platform and seeks to find a technical solution to systematically varying such mechanical cues in the 3D micropores of a single microsieve with the goal to find a set of features that uniquely control the point of most stress in a cell, and also control polarization of the cell.

3.3 Mechanical Cue Configurations and Fabrication Process

A combination of replica molding and laser ablation is used to fabricate microsieves [12]. In Figure 3.1, the lab-scale manufacturing process for this NOA81 microsieve is shown. In Appendix B.3, this fabrication process is extensively described, and in Appendix B.4 an overview is given of the time that each manufacturing step takes. Moreover, in Appendix B.5 all process steps are mapped visually and divided into production units, which is useful for making the manufacturing process more efficient.

The lab-scale manufacturing process is a double replica moulding process, using the µSEA as an original mold to make a *negative* secondary mold in PDMS. This step produces semi-finished microsieves in NOA81 containing the pyramidal shapes gained by anisotropic wet etching in single crystal silicon. Some level of cost reduction can be expected compared to the fabrication of the original µSEA structures in silicon, and besides, such a replica technique now offers us the opportunity to modify the shape per micropore employing a laser ablation process. This process offers several parameters which can be altered in order to influenced the physical landscape within the 3D geometry of the pyramid-shaped micropore, see Section 3.4.

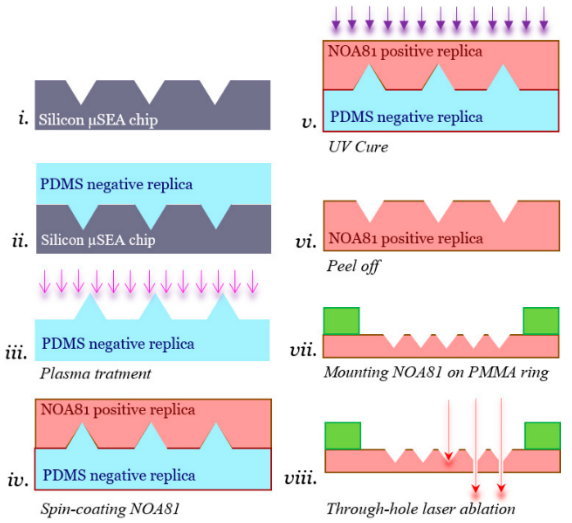

(a) Schematic overview of the fabrication process [12].

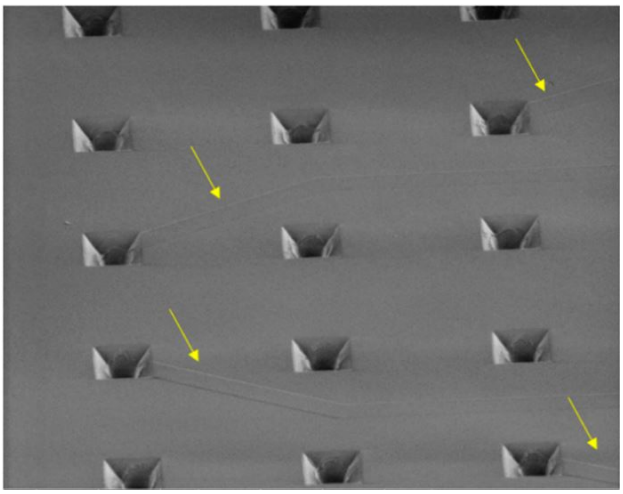

(b) SEM image of resulting NOA81 microsieve [12].

Figure 3.1: Overview of the NOA81 microsieve.

3.4 Configurations of Patterns

3.4.1 Approach of Design

In the µSEA and in the NOA81 of Moonen et al. the through-hole was shot in the middle of the micropore and from the front. By changing the position and point of entry of the laser either from the front or the rear of the semi-finished NOA81 microsieve, different geometries can be created to induce stress on the single cell level. The first proposed alterations of the laser ablation process can be seen in Table 3.1. A green dot indicates a through-hole shot from the front and pink from the rear.

Table 3.1: Proposed alterations of the through-hole of the NOA81 microsieve.

Position	Middle		Edge		Slope	
Entry Point	Front	Rear	Front	Rear	Front	Rear
Top View Schematic						
Top View with Cell						
Cross Section	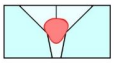	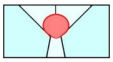	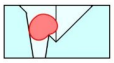	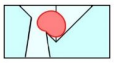	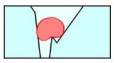	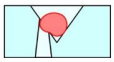

Table 3.1 depicts the schematic configurations in a top view and the expected cell response in top and cross-sectional view. When the holes are ablated in the center, the mechanical cues are symmetric, so no preferred direction for polarization is expected. This may influence how likely the cell is to form an axon which grows out of the micropores, while the soma itself stays in there. When the holes are ablated on an edge or slope, the mechanical stimuli are not the same in all directions. This may give rise to a preferred direction of polarization and resultingly axonal outgrowth.

The ablation process does not result in a cylindrical through-hole, but a conical shape with a draft angle of 18°. Therefore, it is also interesting to shoot the through-hole from the rear as well. Cells are easily deformable, so when the hole is shot from the front, the entire cell might end up in the cone, thereby still being subjected to symmetric mechanical cues. When the hole is shot from the rear there will be, depending on the position, a smaller opening which prevents this from happening.

In Table 3.1, six different ways of ablation of a hole in the microsieve are introduced. Besides these six combinations, it is also possible to make combinations of more than one hole to create a range of different topographies. In Figure 3.2, all the possible configurations are given for a micropore with two through-holes. When ablating two holes in one micropore, 8 different configurations are possible and 32 when the laser entry point is included.

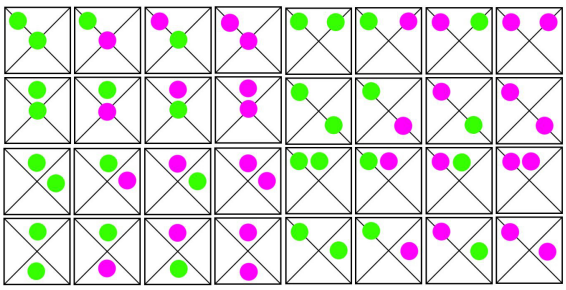

Figure 3.2: Schematic top view of all the possible configurations for a micropore with two through-holes. The green dots indicate holes ablated from the front, the pink dots from the rear.

In Figure 3.3, all the possible configurations are given for a micropore with three through-holes. When ablating three holes in a micropore, 16 different configurations are possible and 128 when the laser entry point is included.

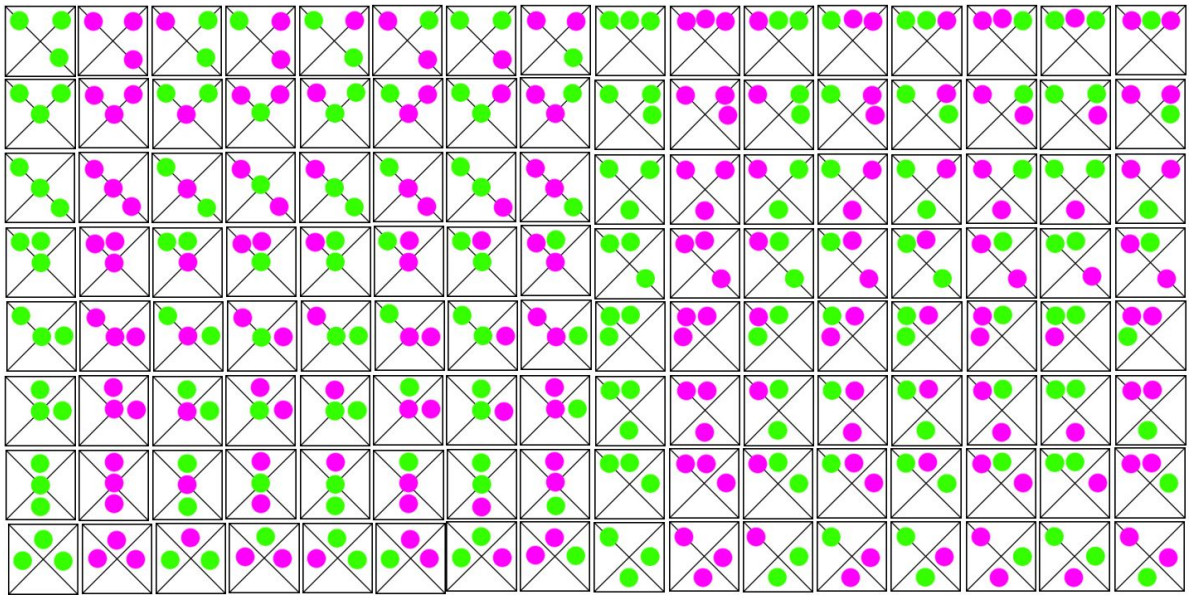

Figure 3.3: Schematic top view of all the possible configurations for a micropore with three through-holes. The green dots indicate holes ablated front, the pink dots from the rear.

3.4.2 Selection of Configurations

All the possible one-, two-, and three-hole configurations together, amount to a total of 166 different possibilities. For a first exploratory test, this number is too high to make and test them all, so a selection was made. Configurations were dismissed because of three reasons. First of all, there are some configurations which can be considered duplicates (though sometimes mirrored), which do not have to be tested both (Figure 3.4 on the left). Then there are also some configurations which do not really give a clear directional mechanical cue to a cell due to symmetry or complete lack thereof (Figure 3.4 in the middle). Finally, the configurations with three holes are already quite complex. With those, combinations of ablation from the front and the rear in an alternated fashion are not taken into account yet (Figure 3.4 on the right).

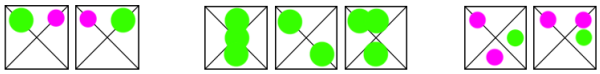

Figure 3.4: Examples of configurations which where dismissed. Left) due to symmetry, middle) due to unclear directional cue and right) due to excessive complexity, three holes and different point of entry.

After dismissing configurations using the three criteria above, 38 configurations were left (Figure 3.5a). To get a better idea of what their geometry would come to look like, a 3D model was made using NX 12.0 (Figure 3.5b).

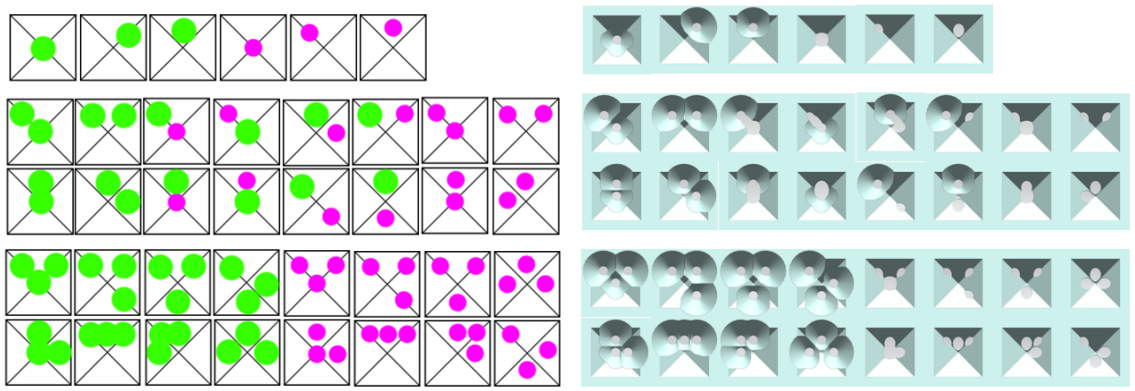

(a) (b)

Figure 3.5: Top view of the 38 configurations chosen to fabricate a) schematic, where the green dots indicate holes ablated from the front and pink from the rear, and b) modeled in 3D using NX 12.0

3.4.3 Fabrication

For the laser ablation of the NOA81 microsieves, the unablated semi-finished sieves were kindly provided by Rahman Sabahi-Kaviani, who is the student at Neuro-Nanoscale Engineering working on this topic towards his PhD. These microsieves were spin coated at 800 RPM and therefore had a thickness of 20 µm [12]. The holes were ablated using a krypton fluoride (KrF) excimer laser, available as a laser micromachining tool at the Microfab/lab at TU/e. The laser was focused on the flat surface of the microsieve and 1500 pulses were shot at 150 Hz (Figure 3.6). Each of the 38 configurations was executed in threefold, to be able to evaluate differences and to account for inaccuracies. As the 114 ablated micropores were spread over the microsieve, regularly the laser was refocused on the surface. This was done as the sieve may not have a homogeneous thickness all over, or may not sit completely leveled in the laser setup.

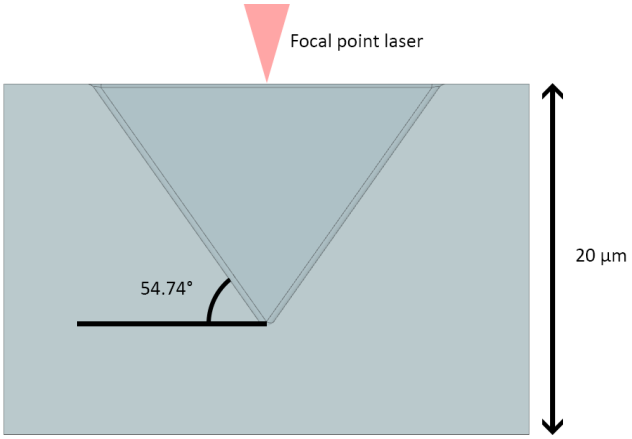

Figure 3.6: Cross-section of the unablated cavity with dimensions and laser focal point.

3.5 Results

In this Section, the fabricated structures as chosen in Section 3.4.2 are evaluated. Each configuration was executed three times, which is why from each micropore there is an upper, middle and lower version in the Tables 3.2, 3.3 and 3.4. Of the ablation results, images were taken from the front and rear, as it is difficult to evaluate a geometry in one focal depth. For the images from the front and rear two different optical microscopes were used for the best image quality. From the upper micropore two images were also taken from the front side at two focal depths.

3.5.1 Laser Ablation from the Front

In Table 3.2, an overview can be seen of the micropores which were ablated from the front. The configurations with one hole all yielded proper through-holes. In the configurations with two and three holes, the holes appear to overlap resulting in one big hole. This is undesirable as cells are more likely to slip through the opening. With the two and three hole configurations, the order of operation is important. Because the holes overlap, a different order of laser shots can give an entirely different geometry. Moreover, these configurations were more difficult to image as the holes are in different focal planes.

Table 3.2: Configurations with holes ablated from the front, schematic, in 3D and optical microscopy images.

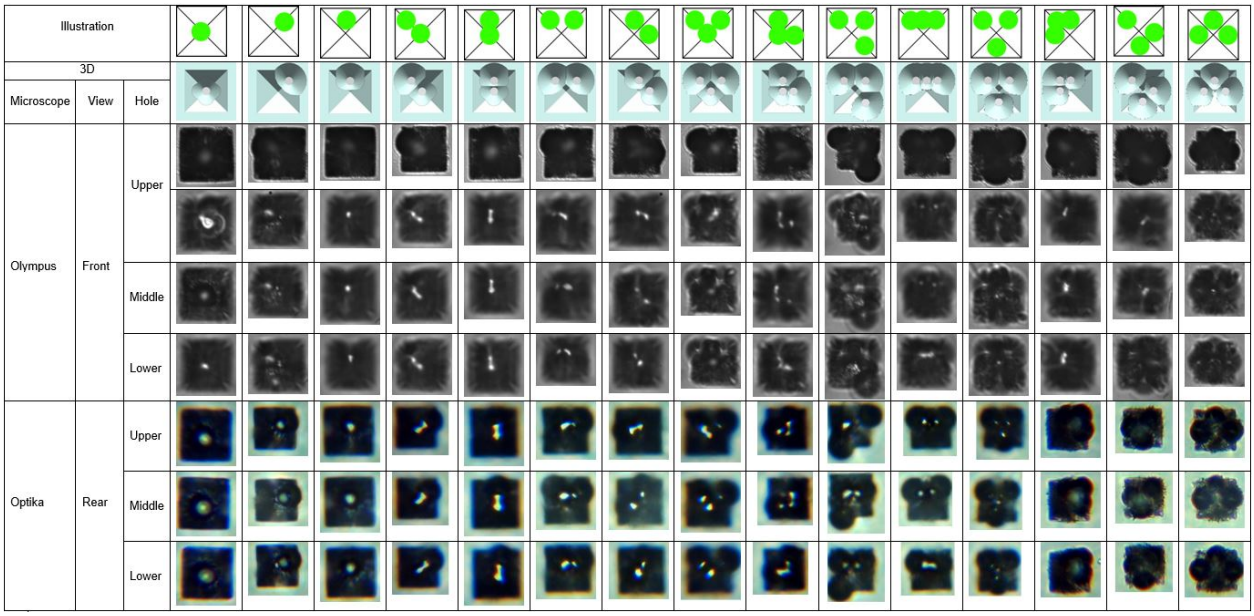

At all configurations, it can be seen that the holes have an offset to the bottom left. This is probably because the focal plane is at the surface and not at the plane where the hole is actually ablated, which can cause an offset in the position of the point of ablation. As a result, it is difficult to aim the laser shots on the middle and slope. Therefore, the cell may experience a similar cue in both cases. By shooting the hole closer to the edge of the pyramid-shaped, the difference can be made more distinct. It can also be seen that the images in the upper row, which were made at the focal depth of the surface, the conical shape matches well with the 3D models.

3.5.2 Laser Ablation from the Rear

In Table 3.3, an overview can be seen of the micropores which were ablated from the rear. Compared to Table 3.2, it can be clearly seen that all images look a lot “cleaner”. The holes are positioned more accurately and are also rounder and have a slightly larger diameter than the sieves ablated from the front. When shooting holes from the rear, the surface is the focal plane. This reduces the offset of the holes and also more energy is absorbed into the NOA81, resulting in larger holes.

Table 3.3: Configurations with holes ablated from the rear, schematic, in 3D and optical microscopy images.

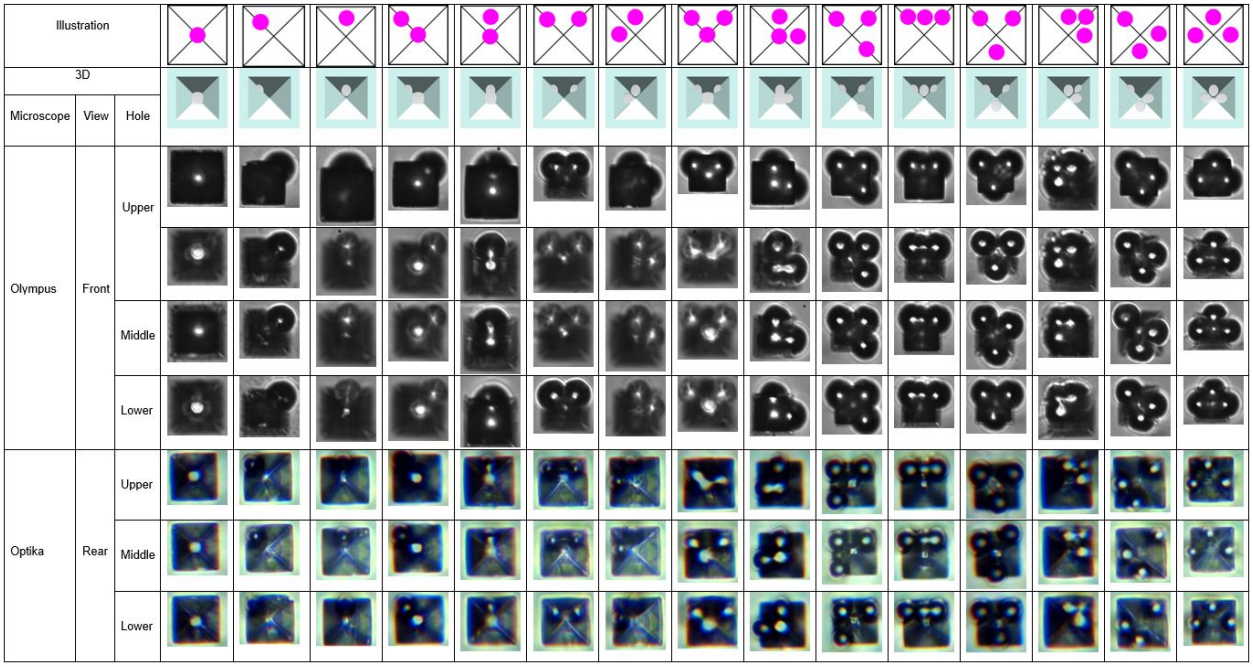

Again, the configurations with one hole all yielded proper through-holes. But in this case, the two holes configurations do not overlap and the three hole configurations only overlap in a few cases. Still, the order of operations remains important. Compared to holes ablated from the front, now the pyramidal shape is altered much less. When shooting from the front, an entire cone is added to the topography, while here only the end holes are added to the topography.

3.5.3 Laser Ablation from Two Sides

Table 3.4: Configurations with holes ablated from two sides, schematic, in 3D and optical microscopy images.

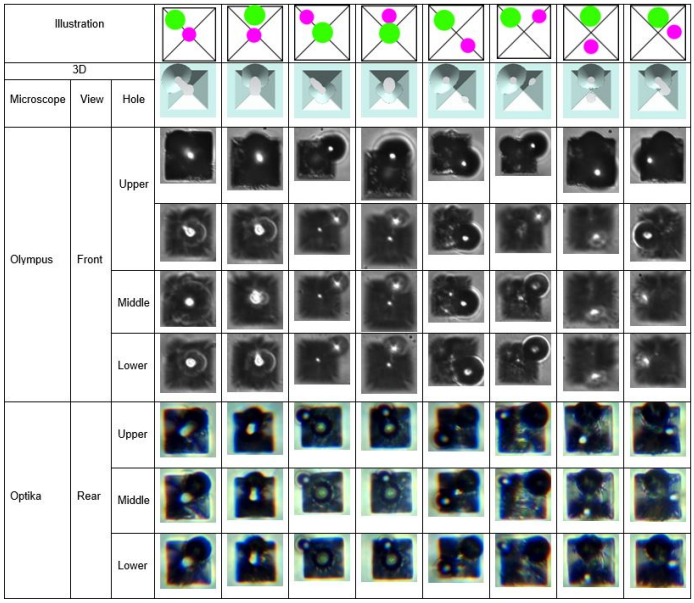

In Table 3.4, an overview can be seen of the micropores which were ablated from two sides. In the first four configurations, the 3D models were correct as the holes overlapped here. When shooting holes from two sides, the cone-shaped holes are more likely to form one bigger hole. Moreover, it can be seen that the holes are in a completely different focal depth and thereby difficult to image.

3.5.4 Size of the Through Hole

For the micropores ablated from the front, a focal point at the surface of the sieve makes it difficult to properly position the holes. As a result, the configurations with one hole yield proper through-holes while the other configurations are very likely to overlap. The ablation from the rear gives better positional accuracy and makes it less likely to overlap the holes. Both options give a very different topography for the cells. In the micropores ablated from two sides, the holes most likely overlap.

Table 3.5: Diameters through-holes in µm, depending on position and entry point of laser ablation.

Entry Point	Position	1	2	3	Average
Front	Middle	2.9	3.0	3.0	3.0
	Edge	2.3	2.7	2.7	2.6
	Slope	2.4	2.6	2.8	2.6
Rear	Middle	3.1	3.6	3.2	3.3
	Edge	2.4	2.8	2.9	2.7
	Slope	2.6	2.8	2.7	2.7

It was found that the through-holes have different sizes depending on the position and entry point. Hence, for each option the size of the through-hole was measured at three different micropores, to get an average value which could be used for further improving the 3D model. In Table 3.5, it can be seen that the holes ablated from the front are smaller, which is due to the focal depth which is not aligned with the micropore. Moreover, the holes in the middle are larger than those on the edge and slope. This is not a surprise, as at the middle the sieve is thinner and at the edge and slope the sieve has the same thickness.

3.6 Conclusion

For researching the working of AD and potential treatments, a microsieve can be used to allow 1) replication of relevant neuronal processes, 2) repeatability of experiments and 3) facilitating screening in a cost effective manner fit for established workflows in the industry. There are indications that cells polarize towards the point where they experience the most stress. In the double replica molding fabrication process of the NOA81 microsieve, the position of the laser ablation hole is flexible and can be used to create topographical cues for stress concentrations in cells. The through hole can be ablated from the front or the rear, in different places of the cavity to form a unique 3D micropore. Combinations of multiple holes can be used to create specific topographical cues. From all possible one-, two- and three-hole configurations, 38 options were selected and fabricated. The configurations with holes ablated from the front were more difficult to fabricate accurately than those ablated from the rear, because of the position of the focal point. The configurations ablated from both sides yielded the most inaccurate results and are therefore not further considered. The position and entry point of the laser ablation also has an influence on the size of the through hole. These changes in size were incorporated when the cell behaviour in the remaining 30 configurations was simulated, see Chapter 4.

4 Numerical Modelling of Mechano-Induced Stress in Cells

4.1 Introduction

In our research providing physically engineered microenvironments at the length scale of a single cell (described in Chapter 3), a stem cell's deformation upon locally-induced mechanically stresses in the cytoskeleton as a means to influence its differentiation behavior was considered. Since biological experiments, i.e. cell culture, are time consuming and resource intensive, there is here aimed for a numerical modeling approach. The study should assist in discriminating features of interest from the many potential topographies that can be fabricated by the combination of micromolding of an inverted pyramidal shape and laser micromachining. To be able to predict the influence of the mechanical cues that these configurations would give, we proposed doing experiments *in silico*. To this end, a 3D finite element model of a cell was created. In this Chapter, first the general modeling approach is introduced. This approach is based on existing atomic force microscopy (AFM) indentation FEM modeling methods, but extended to incorporate the influence of gravity, friction and the complete dynamic behaviour of the cell [63, 64]. Next, we discuss the two components of the model: the continuous model for the membrane, cytoplasm and nucleus as well as the tensegrity model to describe cytoskeleton, nucleoskeleton and intermediate filaments. Then, there is also summarized how the parameters of the material properties of this extended model were determined and how the micropores were modeled. Finally, the results from the simulations are shown and the criteria for selecting topographic configurations will be discussed.

4.2 Modeling Approach

4.2.1 Cell Models in Literature

In the literature, many papers can be found about the modelling of cells. Most of these models describe the biological processes of cells, represent 2D simplifications, or are only about specific parts and processes of the cell [65, 66, 67, 68, 69, 70, 71, 72, 73]. Such models are not useful when evaluating the mechanical stresses which a cell experiences, when put into a certain physical three-dimensional environment with solid boundary conditions being of the same length scale as the cell soma size. To be able to do that, 3D FEM-modeling is a useful tool. No suitable 3D, completely dynamic FEM-model could be found in the literature so far, but modeling methods used to simulate atomic force microscopy (AFM) indentations on static cells formed a useful starting point [74, 63, 75, 64]. However, these models show two limitations in the evaluation of how the cell deforms in a micropore. The first is that in the AFM indentation models, the cell is connected to the substrate and therefore cannot move freely. The second is the probe being the only acting force, excluding gravity or friction forces. The former did not require large alterations however, as cells of different shapes, sizes and areas of connection to the substrate were found in the literature. In contrast, the latter needed larger ramifications, as the lack of gravity results in a model with significantly different values for the mechanical properties of the cell elements (Section 4.2.5). In the AFM indentation models in the literature, three types of approaches to the modeling of the individual cell behaviour are most common:

1. The continuum method describes the cell as a continuous medium, by meshing it into finite elements [70, 71, 76]. Usually, the cell is then subdivided into three components: the membrane, cytoplasm and nucleus. This method gives some insight in cell mechanics, but it does not include the influence of the cytoskeleton (CSK). The CSK is called the skeleton for a reason. It forms the backbone of the cell and is the main determining factor of the mechanical properties of a cell.

2. The tensegrity (tension - structural integrity) method describes the cell as a network of struts and cables, as a means to model the CSK [64]. These struts and cables represent the intricate polymer network within a cell. Due to this network, forces applied to cells will be spread throughout the cell, instead of just having a local effect. This method can vary in complexity from only modeling the microtubules and actin filaments, to also including intermediate filaments (IFs) and even the nucleoskeleton (NSK).

3. A hybrid approach combines the methods defined in point 1 and 2 to create a more realistic cell model. In such models, the mechanical behaviour still mostly depends on the CSK [74, 75, 63, 77].

To be able to accurately mimic the mechanics of a live cell nesting into a 3D micropore, the hybrid method was used as a foundation for the model described in this study. For the continuous part of the cell, the lipid bilayer (membrane), cytoplasm and nucleus were included. The tensegrity part of the cell includes the CSK, NSK and intermediate filaments.

In the model, there are two acting forces present: gravity and friction. The gravity has an acceleration of 9.81 m/s^2. The friction coefficient between the NOA81 micropore and the membrane is set at 0.45 [78]. It is already known that the cells would end up in the micropore, and therefore the influence of the hydrodynamic flow was excluded as it would significantly complicate the simulation [11, 57].

4.2.2 Modeling Software

For the FEM-model, two software packages were used: NX 12.0 and Marc Mentat 2018.1.0. NX was used to model the continuous cell model and the micropores with the ablated holes at different positions. These 3D geometries were then imported into Marc Mentat. The tensegrity cell model and the simulations were respectively modeled and run in there. Marc Mentat works node-based, which makes it suitable for adding the intricate tensegrity model into the continuous model. Moreover, this FEM software was chosen for its compatibility with large strain non-linear analyses [79]. Similar software packages, like SolidWorks and NX Nastran, both lack the ability to dynamically model the intricate geometry. When it comes to NX Nastran, the appropriate licenses for large strain nonlinear analysis are not available at the TU/e.

4.2.3 Continuous Cell Model

The continuous cell model which incorporates the membrane, cytoplasm and nucleus, was created in NX 12.0 (Figure 4.1a). From there, the components were exported as parasolids and then imported into Marc Mentat. In Marc Mentat, the components were meshed into elements (Figure 4.1b).

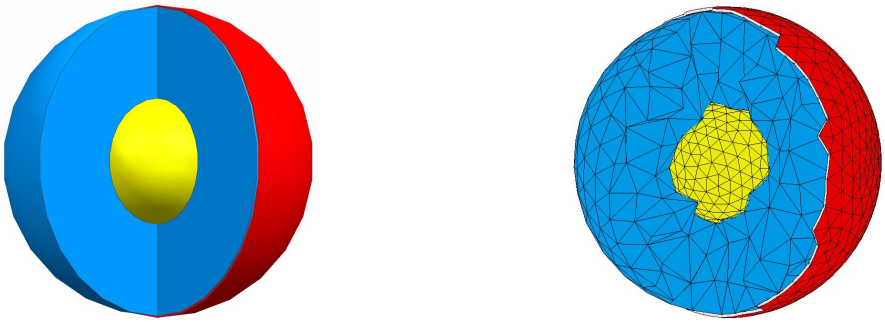

(a) Continuous 3D Model in NX 12.0 (b) Meshed continuous cell in Marc Mentat 2018.1.0

Figure 4.1: Overview 3D models of the continuous parts of the cell, the cell has a diameter of 10 µm. The membrane with a thickness of 0.1 µm is in red, the nucleus in yellow has a diameter of 4 µm and the cytoplasm in blue is between them.

The nucleus was meshed into 929 linear tetra4 elements, the cytoplasm into 3425 linear tetra4 elements and the membrane was modeled as a shell with 1644 quadratic tria6 elements. This is a relatively coarse mesh, which is necessary to be able to support large deformations, even though it decreases the accuracy. For the cytoplasm and nucleus, linear elements were chosen. These do not capture bending and have fewer nodes, which makes them less accurate than quadratic elements. However, in large deformation analyses, bending of elements becomes a problem as the extra node on the edge of each element can cause it to turn inside out (Figure 4.2). This is highly undesirable as it will stop the simulation. As mentioned before, the continuous cell model is relatively irrelevant when it comes to the mechanical properties of the complete cell compared to the CSK, so the decreased accuracy of the elements does not influence the simulation significantly. Besides, finding the exact values of the maximum stresses is not the goal of the simulation, finding their location is.

(a) Linear tetra4 element. (b) Quadratic tetra10 element.

Figure 4.2: The difference between linear and quadratic elements.

For the membrane, quadratic elements were used because it is desirable to know the stresses at the contact points with a more accurate micropore. As the membrane is thin compared to its surface area, it could be modeled as a shell. This is essentially a 2D surface which Marc Mentat treats as a 3D object. By modeling it this way, computation time is reduced, but more importantly, elements are less likely to turn inside out.

The membrane, cytoplasm and nucleus were all *glued* to one another. While deforming, these three elements should not break contact as under normal circumstances no hollow cavities are present within the cell. If instead the components would have had the *touch* contact option, empty cavities can form during the simulation which would mimic air bubbles appearing within the cell out of nowhere.

4.2.4 Tensegrity Cell Model

The tensegrity cell model which incorporates the CSK, NSK and IFs, was added to the continuous cell model in Marc Mentat (Figure 4.3). The basic structure for a tensegrity model of a sphere consist of 6 struts and 24 cables. In this structure the struts carry the compressive forces, while the cables are under tensile stress. Hence, the area of the cross section of the struts is about one order of magnitude larger than that of the cables. The struts form three parallel pairs, each of which is orthogonal compared to the other two pairs. The struts have a unit length A and the struts in the pairs are at a distance $0.5A$ from each other. The end of each strut is connected to the ends of the four closest struts using cables, except to the closest parallel strut. These cables each have a unit length of $\sqrt{0.375}A$ [80].

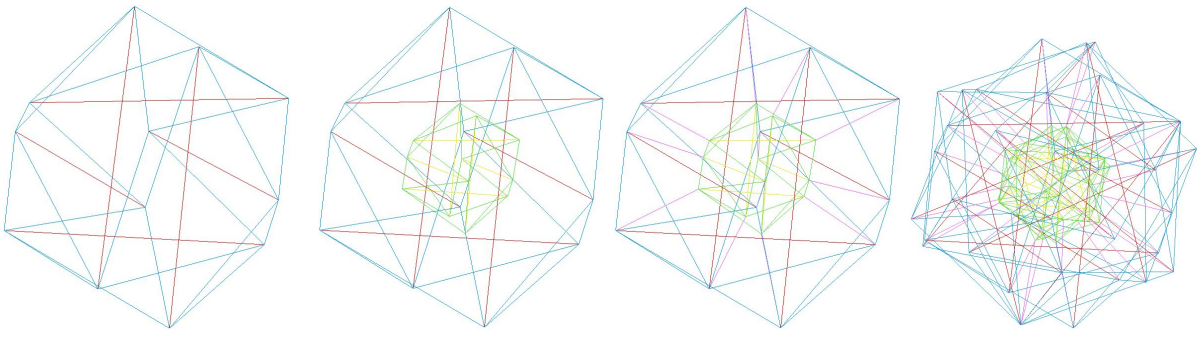

(a) Microtubules and actin form the CSK. (b) Lamina and chromatin form the NSK. (c) IFs couple the CSK and NSK. (d) Model copied twice, rotated 60° and 120°.

Figure 4.3: Tensegrity model of the cytoskeleton, nucleoskeleton and intermediate filaments. With the microtubules in red, actin in blue, nuclear lamina in yellow, chromatin in green and intermediate filaments in voilet.

As a basis for the tensegrity model, the approach by Xue et al. [63] was used. This approach incorporates one spherical tensegrity model consisting of microtubules and actin for the CSK, and another smaller spherical tensegrity model consisting of nuclear lamina and chromatin for the NSK. These two structures were then

connected to each other by the IFs. The implementation of the tensegrity model into the continuous model was done in four steps:

1. To create the CSK, six microtubules (struts) were attached to the nodes at the vertices of the elements of the membrane. Between those 6 nodes, another 24 elements were added forming the actin cables (Figure 4.3a).
2. To create the NSK, six lamina (struts) were attached to nodes at the surface of the nucleus. Between those 6 nodes, another 24 elements were added forming the chromatin cables (Figure 4.3b).
3. For the IFs, twelve elements were added between the closest nodes from the CSK and NSK (Figure 4.3c). This is what connects the CSK and NSK and thereby anchors the nucleus within the cell.
4. To make sure that the model behaves symmetrically when loaded from different directions, the model of Figure 4.3c was duplicated twice. These two copies were then respectively rotated 60° and 120° around their Z-axis, (Figure 4.3d). The three structures were not connected to one another, as this would significantly influence the mechanical behaviour of the model.

4.2.5 Determining the Mechanical Properties of the Cell Elements

Both the continuous and tensegrity elements were modeled as linear elastic elements. However, the continuous parts behave more like viscoelastic elements. The use of linear elastic elements was chosen because of the following: first, there is very little information on the viscoelastic mechanical properties of cells, especially of their individual components. In the literature related to 3D FEM-models of cells, generally linear elastic models are used and their mechanical property values differ several orders of magnitude (Appendix C.1). The second reason has to do with what it actually means to use a viscoelastic model. In Figure 4.4, a linear elastic and two very common viscoelastic models, Maxwell and Kelvin-Voight, are qualitatively shown [81]. The latter two are the same as the linear elastic model except for the addition of a so-called dashpot, which represents the viscosity of the medium. When a force is subjected to the linear elastic model, it will reach its steady-state almost instantly. With the two viscoelastic models, there is relaxation time η/E, but in the steady-state the outcome will be the same as or very similar to the linear elastic model [82]. Moreover, specifically for 3D FEM models of cells, this approach has also been validated [70]. With the FEM-model of the cell, the goal is to find out how the cell settles in the micropore. Hence, the more computationally efficient simplification to a linear elastic model was used.

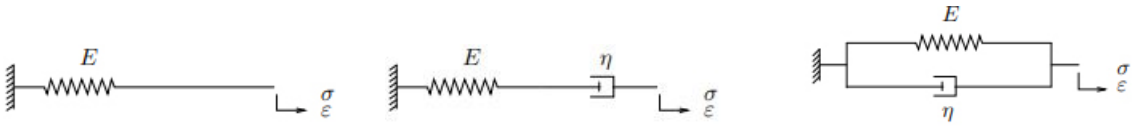

(a) Linear elastic model. (b) Maxwell viscoelastic model. (c) Kelvin-Voight viscoelastic model.

Figure 4.4: Linear elastic model and the Maxwell viscoelastic model. E represents the Young's modulus, σ the stress, ϵ the strain and η the viscosity [81].

When considering the values of the Young's moduli of the continuous parts of the cell model in Appendix C.1, it can be seen that these values are very low. This is due to the absence of the gravity force. The only acting force in these models is the AFM probe. In Figure 4.5, it can be seen that using material properties from Wang et al. [74] results in spikes in the tensegrity structure once a gravity load of only 20% is applied. Besides the fact that this is not what cells look like, it also means that the continuous cell elements cannot spread the influence of the tensegrity structure throughout the model.

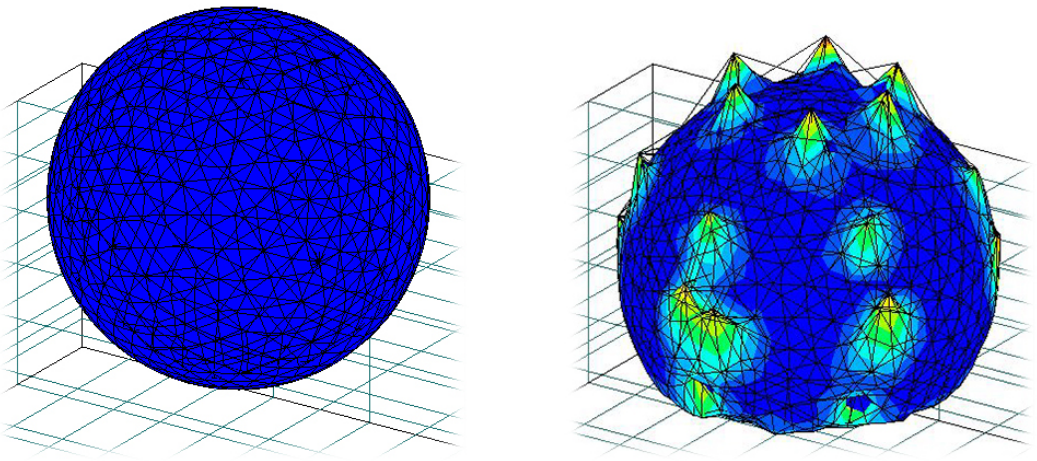

(a) Cell model before deformation. (b) Cell model after 20% of gravity load.

Figure 4.5: Simulation of the cell model on a flat surface with a Young's modulus of 1000 for the membrane, 100 for the cytoplasm and 400 for the nucleus and a Poisson's ratio of 0.49 for all components. The colours indicate Von-Mises stress concentrations.

To obtain more realistic values for mechanical properties of the membrane, cytoplasm and nucleus, the following approach was taken. First, their Poisson's ratio was set to 0.49 because the continuous parts of the cell are assumed incompressible [83, 64, 84]. Then, in Appendix C.1, it can be seen that in most cases the Young's moduli of the membrane, cytoplasm and nucleus have a respective ratio of 1000:100:400. This ratio was multiplied with different factors to evaluate the final shape of the continuous cell model after a gravity load was applied, and then compared to the shape of a cell on a glass substrate after three hours [85]. Here, the rough assumption is made that in three hours the polymers within the cell reshape and relax. The cell takes the shape it would if it was only consisting of a membrane, cytoplasm and nucleus. In Figure 4.6, the results of this analysis are visualized. It can be seen that the multiplication factor of 350 best replicates the experimental cell shape. This results in a Young's modulus of 3.50 $\times 10^5$, 3.50 $\times 10^5$ and 1.40 $\times 10^5$ for respectively the membrane, cytoplasm and nucleus.

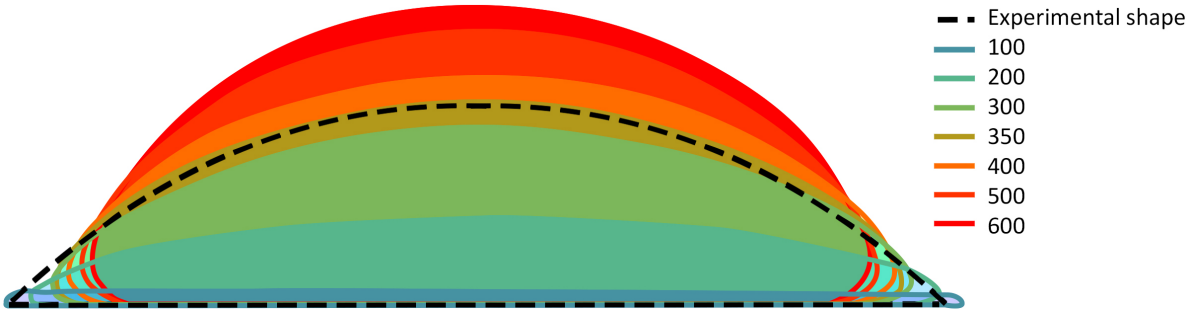

Figure 4.6: Schematic side view of the final steady-state shape of the continuous part of the cell model after gravity load. The membrane, cytoplasm and nucleus all have a Poisson's ratio of 0.49. Their Young's moduli have a ratio of 1000:100:400. The values in the legend are factors with which these moduli have been multiplied. The black dashed line indicates the experimental steady-state shape of a cell after 3h of gravity load [85]. It can be seen that a multiplication factor of 350 gives the best approximation of these experimental values.

For the bulk properties of the CSK, IFs and NSK, a similar approach was taken. The Poisson's ratios were kept at 0.30 for all these components, as in the literature, it does not deviate from this value [74, 63, 75, 77]. To determine the factor with which the Young's moduli had to be multiplied, the following two criteria were set. First, the cell should be able to sit in a hole with a bottom aperture with a 3.5 µm diameter without slipping through [11, 57]. Second, the continuous parts of the cell should not have obvious spikes as in Figure 4.5b. These two criteria led to a multiplication factor of 2, and a final overview of all the bulk properties can be found in Table 4.1. The factor of 2 seems really low compared to the factor of 350 of the continuous cell model. The reason for this is that the cross-sections of the CSK, IFs and NSK are thin, in the order of nm^2, and these elements are therefore barely influenced by the gravity load.

Table 4.1: The material properties of the cell components as determined and used in the FEM-model.

Cell Component	Young's modulus [Pa]	Poisson's ratio [ν]	A [nm^2]	ρ [kg/m^3]
Membrane	3.50×10^5	0.49	Thickness 100 nm	1025
Cytoplasm	3.50×10^4	0.49	Diameter 9800 nm	1025
Nucleus	1.40×10^5	0.49	Diameter 4000 nm	1025
Microtubules	2.40×10^9	0.30	200	1000
Actin filaments	5.20×10^9	0.30	20	1250
Intermediate filaments	4.00×10^9	0.30	79	1000
Nuclear lamina	2.80×10^6	0.30	79	1000
Chromatin	4.88×10^8	0.30	1.13	1000

4.2.6 Modeling the Micropores

The micropores were modeled in NX 12.0. In Figure 2.6b and 3.6 an overview of the micropore was already given with its dimensions. In Figure 4.7, an example of a 3D model how it was used in the simulations is shown. This particular micropore is ablated in the middle from the front is shown. In Figure 4.7b, the positions were the hole were placed in case they were shot on the edge and slope can be seen. The holes on the edges were placed exactly between the middle and the corner of the micropore. The holes on the slopes were placed exactly between the side and the middle of the micropore. The sizes of the hole were modeled in accordance with the experimentally determined dimensions from Table 3.5. The laser ablation hole has a draft of 18°, as can be be measured from [12]. In the same paper, it can be seen that none of the edges are really sharp, especially where a laser hole was ablated. Therefore, to all edges an edge blend with a radius of 0.5 µm was applied. In the simulations, the micropore is modeled as an incompressible element. This was done as the Young's modulus of NOA81 is 1.38×10^9 [86], which is several orders of magnitude high than that of the continuous cell components (Table 4.1). Because of the large difference, the micropore is relatively incompressible. For the model, this means that the micropore does not have to be meshed, and in general it will significantly reduce the simulation time and the chance of the solution not converging.

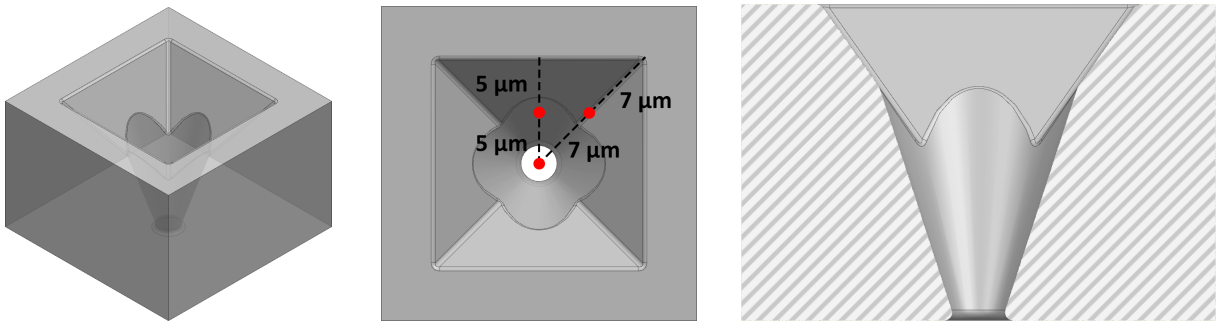

(a) Trimetric view. (b) Top view. (c) Cross section.

Figure 4.7: 3D Model of a micropore ablated in the middle from the front.

4.3 Results

In this Section, the simulation results of the FEM model are given for the structures selected based on Section 3.4.2 will be evaluated numerically. An overview of all simulation results can be found in Appendix D. The configurations are named via the following method: In case of one hole, the name is **XY**, where **X** represents the side from which side the hole is ablated (**F**ront or **R**ear) and **Y** where it is ablated (**M**iddle, **E**dge or **S**lope). In case of two or three holes the name is in the format **XQ_Z**, where **Q** represents the amount of holes and **Z** the configuration number in accordance with Table 3.2 and 3.3. The simulations cover a time span of 30 seconds, within which the model has long reached its steady state. Several *in vitro* cell culture experiments have previously been conducted with micropores ablated from the front, but not for micropores ablated from the rear. Therefore, first the general differences between a micropore ablated from the front and rear are evaluated. Next, the influence of concavity on the cell model will be shown. Then, some criteria are set to be able to evaluate all the 30 configurations on how promising their influence on the cell polarization is expected to be. Finally, the configurations will be divided into different categories and it will become clear which configurations appear the most promising.

4.3.1 Micropores Ablated from the Front versus from the Rear

In Figure 4.8, the simulation results for a micropore in which a hole is ablated either from the front or from the rear of the device can be seen. The colours indicate the Von-Mises stresses. For the cell in the micropore which is ablated from the front, it can be seen that the stresses are symmetrically the highest around the middle of the cell with a maximum value of 2.268 $\times 10^5$ Pa. For the cell in the micropore which is ablated from the rear, there are clear stress concentrations at the edges of the pyramidal shape, with a maximum value of 2.171 $\times 10^5$ Pa. The values for the maximum stresses are very similar in both cases.

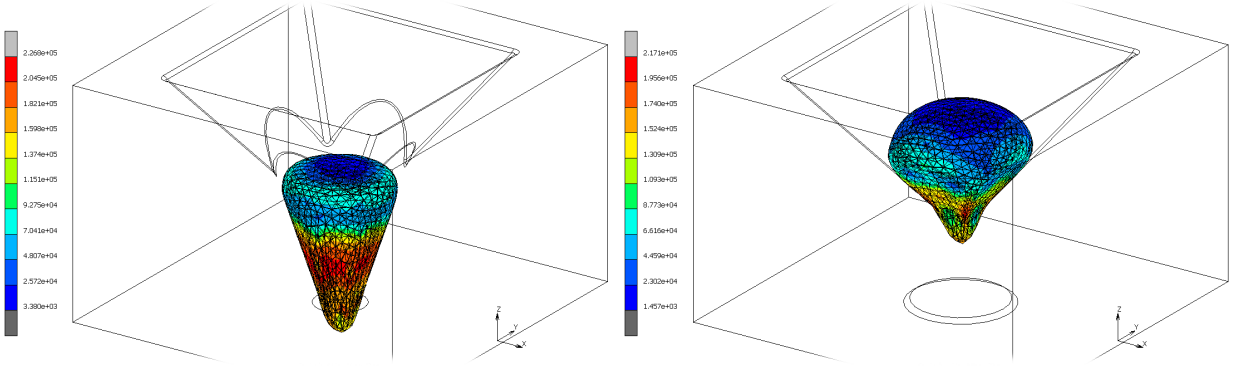

(a) Cell model in micropore ablated from the front. (b) Cell model in micropore ablated from the rear.

Figure 4.8: Comparison of simulations of the cell model under a gravity load in a micropore, ablated from the front and from the rear. The colours represent the Von-Mises stresses.

A clear difference between the two results is that in Figure 4.8a, the cell is positioned entirely within the cone-structure that is created by the laser ablation. In fact, the cell does not even touch the initial pyramidal structure which was fabricated with the double replica molding process. On the other hand, the cell in Figure 4.8b is still almost completely within the pyramidal part of the micropore and has morphology which is closer to spherical. When the cell sits completely within the cone-structure of the laser ablation rather than in the pyramidal structure, then it experiences a symmetric environment from all sides, so no distinct directional mechanical cue is present.

Hooke's law states that stress is equal to:

$$\sigma = E\epsilon \tag{4.1}$$

With σ the stress, E the Young's modulus and ϵ the strain, it depends largely on the Young's modulus of the material. As a result, the highest stresses are very likely to be present in the membrane, as its Young's

modules is 10× larger than that of the cytoplasm and 2.5× larger than that of the nucleus. When reviewing the cross section in Figure 4.9, this is also clearly visible.

Because the hypothesis in this project is that the axon will be defined from the points in the cell with the highest stress, from now on there will be mostly focused on the stresses on the cell membrane.

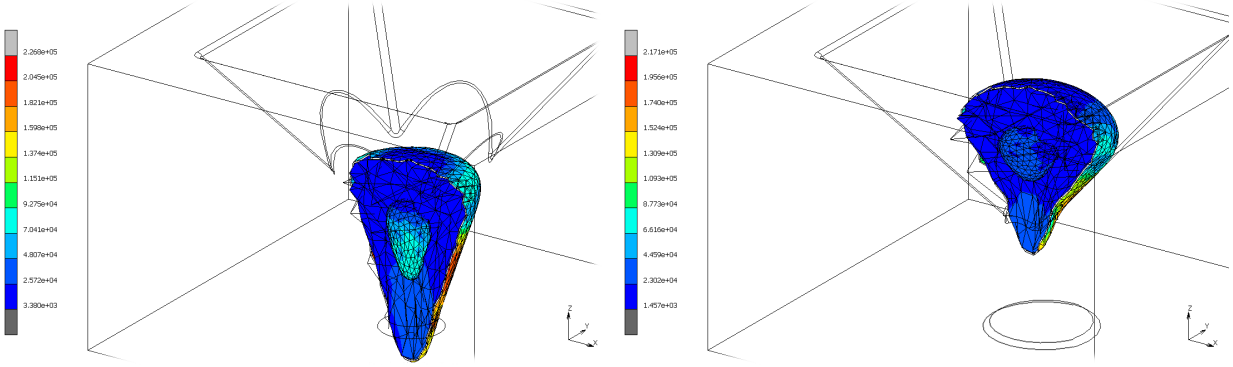

(a) Cell model in micropore ablated from the front. (b) Cell model in micropore ablated from the rear.

Figure 4.9: Cross section comparison of the cell model under a gravity load in a micropore, ablated from the front and from the rear. The colours represent the Von-Mises stresses.

4.3.2 The Tensegrity Structure in Concavity

In some configuration, the cell model will take on the inverted concave shape of the pore. In Figure 4.10, an example for a configuration is shown in which this is the case. When the cell model becomes concave, it can occur that the tensegrity model does not stay within the cell membrane. This is possible because the tensegrity structure is connected to the membrane and can therefore also not have another contact interaction with it. This behaviour only happens in a few of the configurations which were tested and therefore barely. Nevertheless, it is something that should be kept in mind when testing other configurations, as this is not according to the regular cell behaviour.

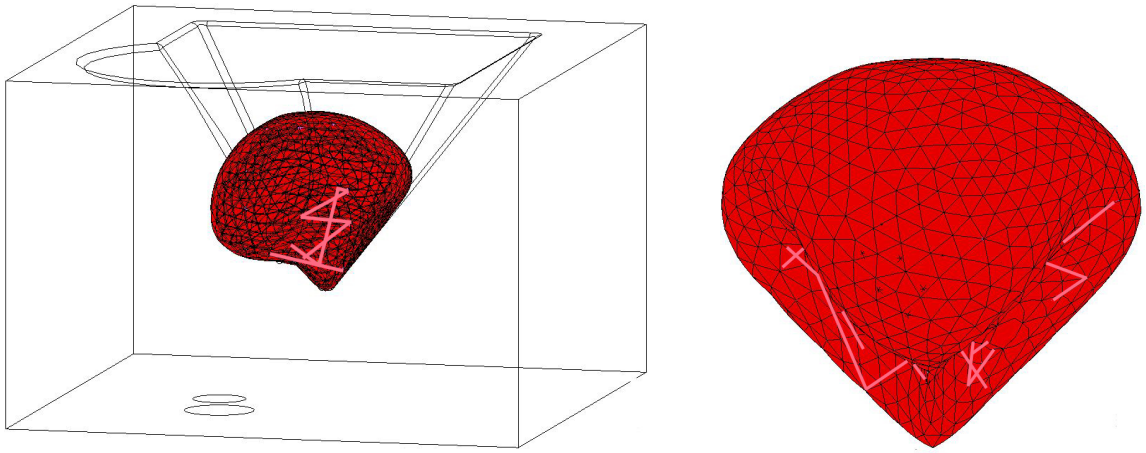

(a) Trimetric view in micropore. (b) Close up view.

Figure 4.10: Example of a configuration where the cell has adopts the partly concave shape of the micropore, with the membrane in red and the actin in violet. Because of the concave shape, the tensegrity model does not stay within the membrane.

4.3.3 Method for Dividing the Configurations

When evaluating the results in Appendix D, it was found that many configurations gave similar results and had similar reasons on why they would not make good configurations for influencing the polarization process of the neurons. Therefore it was decided to divide the results according to these failure mechanisms. Each set of configurations is explained through an example and the result of this division is given in Table 4.2.

Slips Through
In Figure 4.11, the simulation results of configuration R2_2 are shown. This simulation and R3_2 are the only ones that did not run the full 30 seconds. The two holes create one big hole in the micropore (Figure 4.11a), hence, the cell is able to slip through. While doing so, it is so severely and unnaturally deformed that the simulation could not converge.

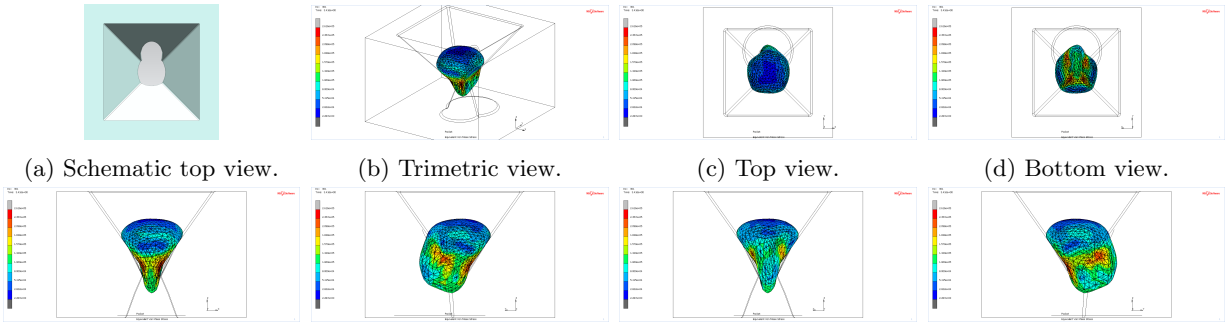

(a) Schematic top view. (b) Trimetric view. (c) Top view. (d) Bottom view.

(e) Front view. (f) Left view. (g) Back view. (h) Right view.

Figure 4.11: Simulation results of configuration R2_2 where the cell **Slips Through**.

Position Uncertain
In Figure 4.12, the simulation results of configuration R2_3 are shown. When there are multiple holes ablated from the front, it is not possible to predict where the cell will come to sit. This can depend on the side from which the cell approaches the pocket during the hydrodynamic flow. Also, the cell seeding process is executed by hand and therefore variable.

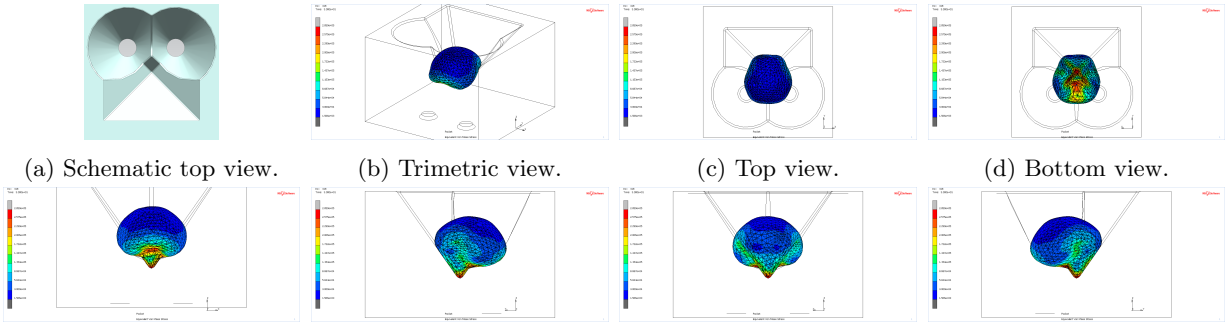

(a) Schematic top view. (b) Trimetric view. (c) Top view. (d) Bottom view.

(e) Front view. (f) Left view. (g) Back view. (h) Right view.

Figure 4.12: Simulation results of configuration R2_3 where the cell **Position is Uncertain**.

In Cone
In Figure 4.8a, it can be seen that in some configurations the entire cell will remain within the cone of the laser ablation. Then, it does not receive any directional mechanical cue.

No Cue Contact
In Figure 4.13, the simulation results of configuration RE are shown. It can be seen that in the configurations where a hole is ablated on the edge from the rear, the cell makes no contact with the mechanical cue from that hole.

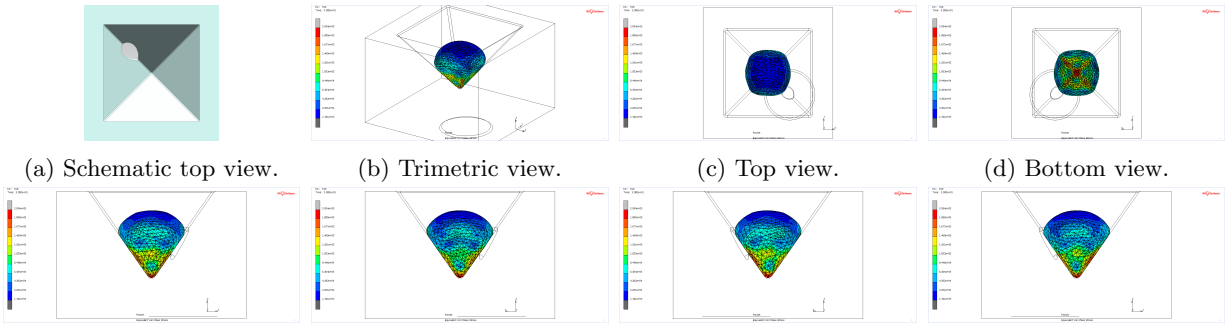

(a) Schematic top view. (b) Trimetric view. (c) Top view. (d) Bottom view.

(e) Front view. (f) Left view. (g) Back view. (h) Right view.

Figure 4.13: Simulation results of configuration RE, where the cell does not **Contact the Cue**.

In Table 4.2, it can be seen that this is the case for quite some configurations. This is because the centers of the holes ablated on the edge were 7 µm from the center of the micropore instead of the 5 µm which is used for the position of the ablations on the edges. Therefore, the configuration FE, R2_1, R2_3, R3_1, R3_3, R3_5 and R3_7 were simulated once more with the ablation on the edge at 5 µm from the center of the micropore. The results are indicated by doubling the F or R (f.e. FFE) and can be found in Appendix D.5 and in Table 4.2.

Not Directional
In Figure 4.14, the simulation results of configuration RS are shown. Especially in Figure 4.14d, it can be seen that although there are clear stresses concentrations, they do not point in one clear direction. In such cases, there still cannot be estimated in which direction the axon would grow.

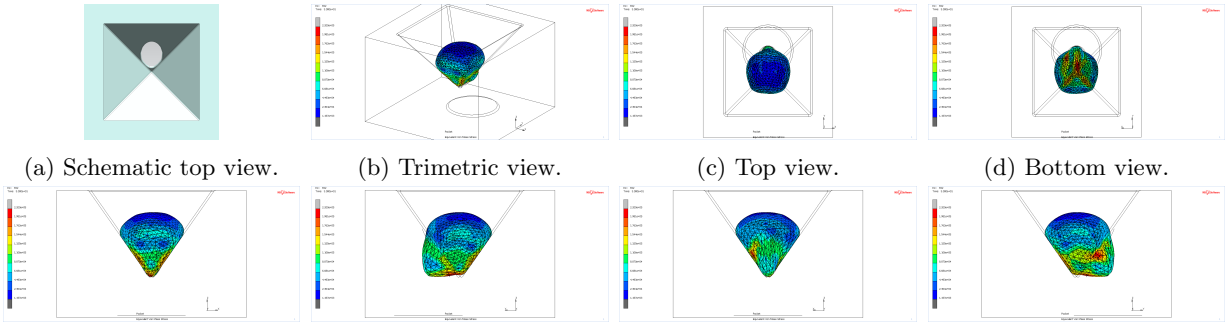

(a) Schematic top view. (b) Trimetric view. (c) Top view. (d) Bottom view.

(e) Front view. (f) Left view. (g) Back view. (h) Right view.

Figure 4.14: Simulation results of configuration RS, where there is **No clear Directional Cue.**

4.3.4 Divided Configurations

The simulated configurations were reviewed based on the failure mechanisms from Section 4.3.3. This was done in the specific order in that Section. The results can be seen in Table 4.2. If a configuration already falls into the category of one failure mechanism, it does not matter if it also falls into another category. That is why each configuration only has a maximum of one X in its row. If the configuration did not comply with any of the failure mechanisms, it was seen as a promising configuration and an X was placed in the last row.

Table 4.2: Division of the simulation results.

	Slips Through	Position Uncertain	In Cone	No Cue Contact	Not Directional	Promising
FM			X			
FE			X			
FS						X
RM					X	
RE				X		
RS					X	
F2_1		X				
F2_2		X				
F2_3		X				
F2_4		X				
R2_1				X		
R2_2	X					
R2_3				X		
R2_4						X
F3_1		X				
F3_2		X				
F3_3		X				
F3_4		X				
F3_5		X				
F3_6		X				
F3_7		X				
F3_8		X				
R3_1				X		
R3_2	X					
R3_3				X		
R3_4					X	
R3_5				X		
R3_6						X
R3_7				X		
R3_8					X	
FFE						X
RRE						X
RR2_1	X					
RR2_3						X
RR3_1	X					
RR3_3					X	
RR3_5					X	
RR3_7					X	

It can be seen that only six configurations have the label "promising" out of the 30 simulated configurations, of which four are ablated from the rear and two from the front. In Figure 4.15, these six configurations are shown, with a red arrow indicating the direction of the mechanical cue. Noticeable is that configuration R2_4 and R3_6 are basically the same configuration, as the ablation on the edge does not even contact the cell. When taking that into account, the configurations are relatively simple, consisting of one or two hole close to each other. It appears that stress concentration on the cell is in all configuration situated on a sharp corner. This is important to consider when designing other configurations. Moreover, the configurations give both horizontal/vertical and diagonal cues, which is useful for creating connections in different directions.

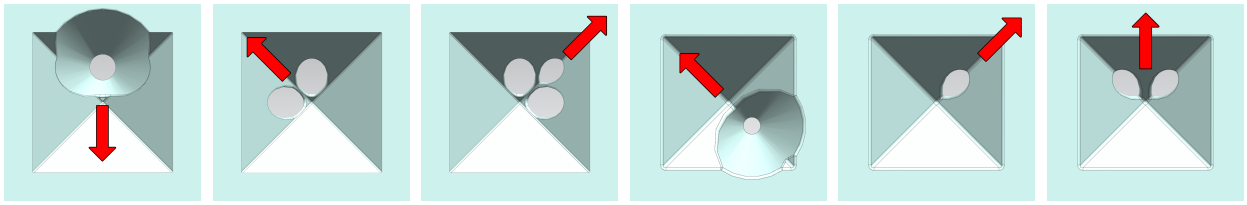

(a) FS. (b) R2_4. (c) R3_6. (d) FFE. (e) RRE. (f) RR2_3

Figure 4.15: The configurations which are deemed most promising for influencing the polarization process of the cell. The red arrow indicated the direction of the mechanical cue.

4.4 Conclusion

A 3D fully dynamic FEM cell model was created, based on semi-3D, semi-dynamic AFM FEM cell models. This model is a hybrid model consisting of a continuous part for the membrane, cytoplasm and nucleus and a tensegrity part for the CSK, NSK and IFs. The continuous part was modeled in NX 12.0 and then imported into Marc Mentat 2018.1.0, where the tensegrity structure was added and the model simulated. The material properties in the AFM FEM models did not incorporate the influence of gravity, so appropriate values for the material properties when gravity is included, were determined using simulation experiments. The micropores were modeled based on the images from Sabahi-Kaviani and Luttge [12] and the experimental results from Section 3.5. The cell model was then simulated for 38 different configurations of ablation holes in the micropore. From these 38 configuration, 6 are expected to give a distinct mechanical cue to the cell, thereby influencing the polarization process. This distinct mechanical cue is in all six cases present on a sharp corner. Moreover, of these configurations two give a horizontal/vertical cue and four a cue in diagonal direction.

5 Application of the Numerical Model

5.1 Introduction

In this Chapter, the numerical model as described in Chapter 4 is applied to a variation of different geometries. The application of the model is definitely not limited to just these geometries, but this overview gives an impression of how the model behaves in different situations. The four types of geometries which are described are: conical, chessboard-like, resembling the Topochip by Hulshof et al. [87] and lastly, grooved based on the work of Xie and Luttge [88].

5.2 Simulation Results

In the simulations, the cell model described in Chapter 4 was used. The model has a diameter of 10 µm and the material properties used are those in Table 4.1. The simulations time is 30 seconds and the two acting forces are gravity and friction. The gravity has an acceleration of 9.81 m/s^2 and is gradually released over a period of 10 seconds, the friction coefficient between the cell membrane of the NOA81 micropore is 0.45.

5.2.1 Conical

The conical shape on which the model was tested has a bottom diameter of 4 µm, a draft angle of 18° and a depth of 20 µm. These dimension were chosen to replicate the shape of a micropore that is currently being developed in another study, which is fabricated through large area display technologies.

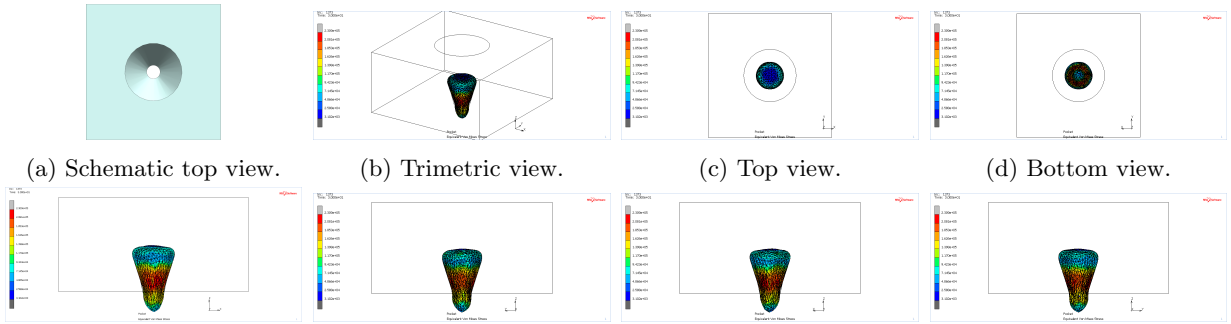

(a) Schematic top view. (b) Trimetric view. (c) Top view. (d) Bottom view.

(e) Front view. (f) Left view. (g) Back view. (h) Right view.

Figure 5.1: Simulation results of the model in a conical micropore.

The results as shown in Figure 5.1, are in line with the results of Section 4.3.1. The cell experiences a symmetric amount of stress all around and does not slip through completely.

5.2.2 Chessboard-like

The model was also tested on chessboard-like structures of 6×6 squares. The sizes of these individual squares were ranged from 2 µm to 20 µm, with steps of 2 µm. All these results can be found in Appendix D.6. Here two of them are highlighted: the geometry with 6×6 µm squares (Figure 5.2) and the geometry with 8×8 µm squares (Figure 5.3).

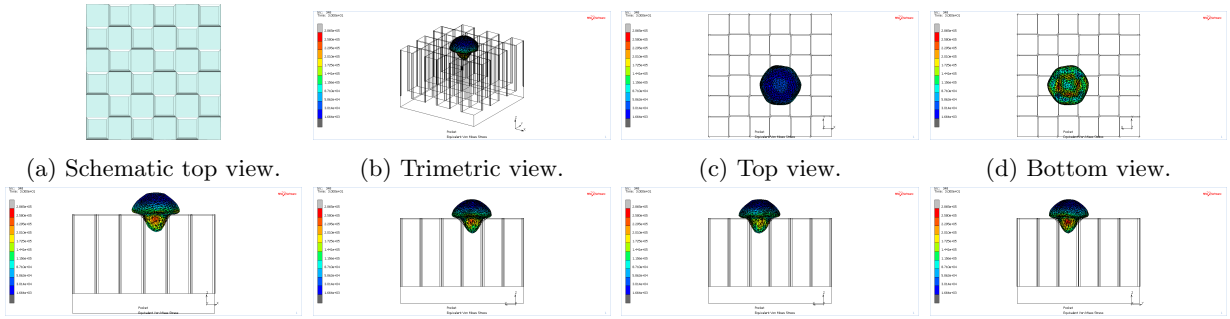

(a) Schematic top view. (b) Trimetric view. (c) Top view. (d) Bottom view.

(e) Front view. (f) Left view. (g) Back view. (h) Right view.

Figure 5.2: Simulation results of the model in chessboard-like layout with 6×6 µm squares.

In Figure 5.2, it can be seen that the cell stays on top of the geometry. The cell was also dropped from a higher distance, to see if with the extra velocity it would slide between the pillars, but the result remained the same. In Figure 5.3, it can be seen that the cell does go between the pillars. The cell takes on a cuboidal morphology, with the exception of its spherical top.

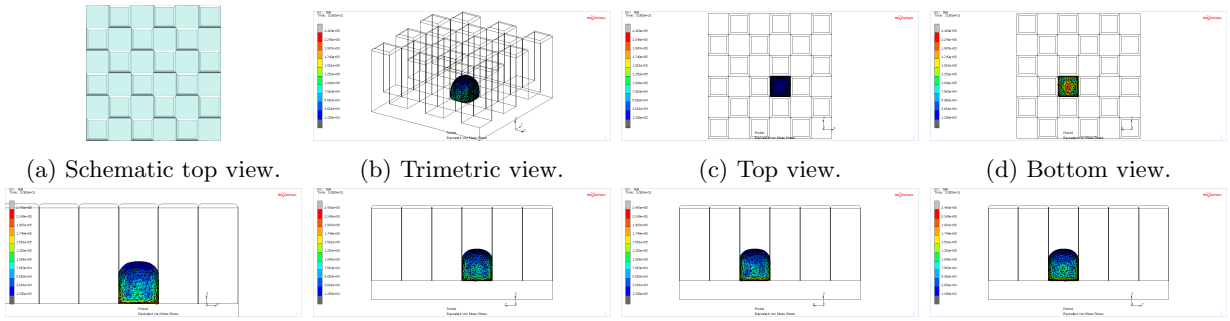

(a) Schematic top view. (b) Trimetric view. (c) Top view. (d) Bottom view.

(e) Front view. (f) Left view. (g) Back view. (h) Right view.

Figure 5.3: Simulation results of the model in chessboard-like layout with 8×8 µm squares.

5.2.3 TopoChip

On the TopoChip [89], 2176 different configurations of geometries are present (B.1.5). Here, for two possible configurations the cell model is tested. In Figure 5.4a, the overview of the complete 3D model can be seen. The upper configuration consists of a 10×10 array of the feature in Figure 5.4b. The lower configuration consists of a 29×29 array of the feature in Figure 5.4c. In the simulations only a small part of the TopoChip was used, as loading the entire 3D model into Marc Mentat 2018.1.0 proved very computationally heavy.

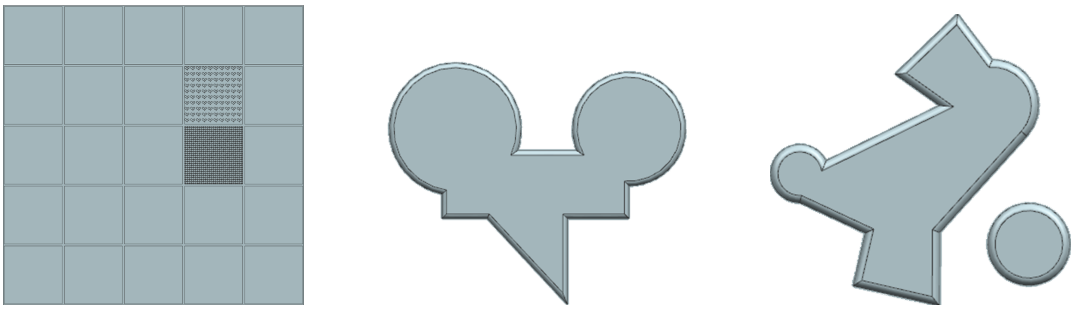

(a) Top view of the model. (b) Feature on the TopoChip (c) Feature on the TopoChip.

Figure 5.4: Overview of the TopoChip and the features on it.

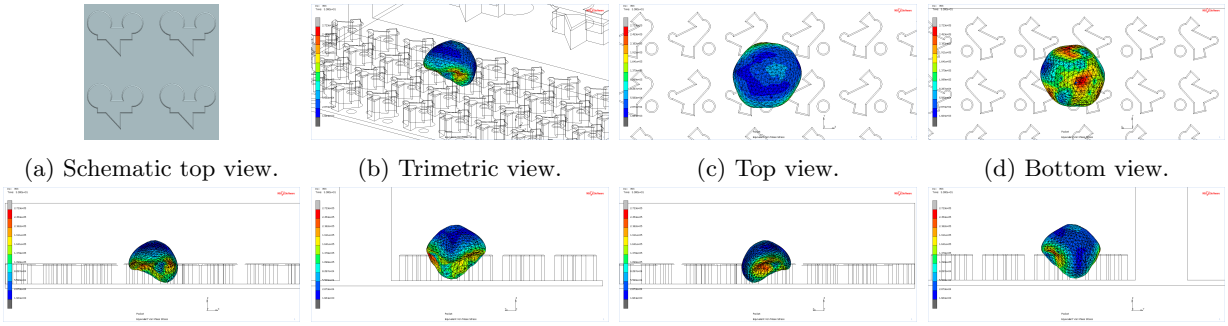

(a) Schematic top view. (b) Trimetric view. (c) Top view. (d) Bottom view.

(e) Front view. (f) Left view. (g) Back view. (h) Right view.

Figure 5.5: Simulation results of the model on the TopoChip.

In Figure 5.5 and 5.6, the simulation results for the cell model on the TopoChip can be seen. The cells take on very different morphologies than in other results. Comparing the numerical cell model on the TopoChip with the experimental results, is likely to be helpful in validation of the model.

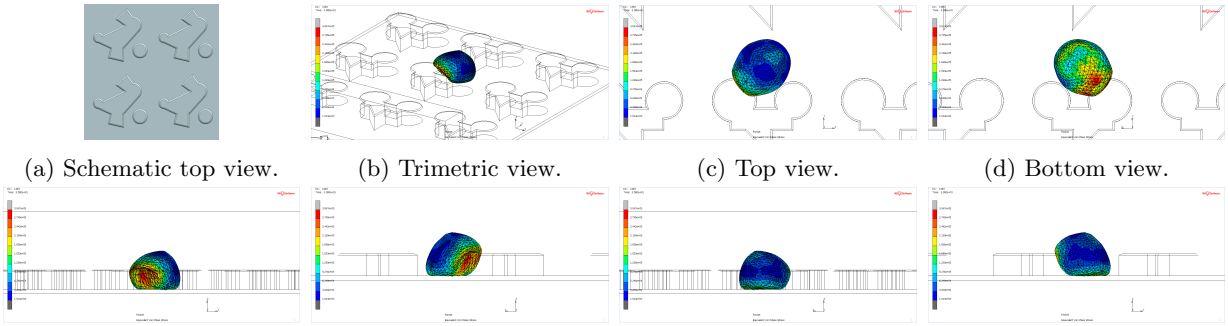

(a) Schematic top view. (b) Trimetric view. (c) Top view. (d) Bottom view.

(e) Front view. (f) Left view. (g) Back view. (h) Right view.

Figure 5.6: Simulation results of the model on the TopoChip.

5.2.4 Grooved Substrate

The final geometry to which the model was applied, is a grooved substrate. The reason this geometry was chosen, is because Heydari et al. [90], used such geometries to validate their cell model. Moreover, Xie and Luttge fabricated nanogrooves on which cells were cultured [88]. Their substrate with nanogrooves was modeled in 3D (Figure 5.7a) and the numerical cell model was applied to it. Here, only the continuous cell model is used, because this represents a cell after a longer period of time on a substrate.

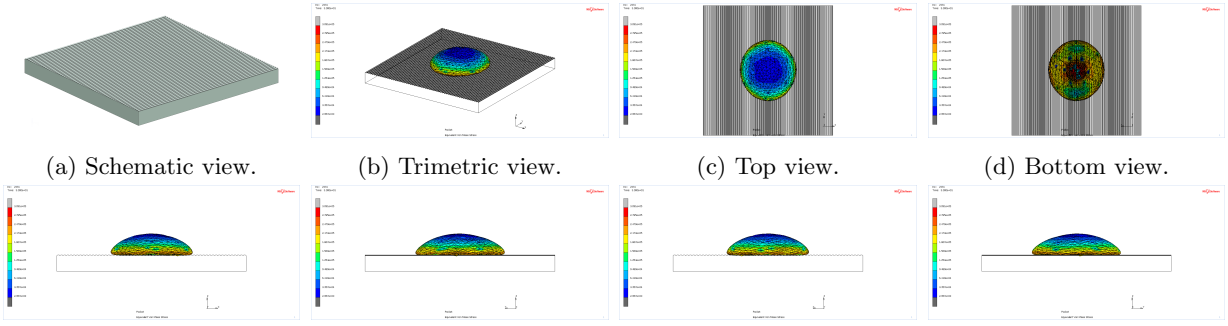

(a) Schematic view. (b) Trimetric view. (c) Top view. (d) Bottom view.

(e) Front view. (f) Left view. (g) Back view. (h) Right view.

Figure 5.7: Simulation results of the model on a substrate with nanogrooves.

In Figure 5.7, the simulation results of the cell on the grooved substrate can be seen. The cell follows the direction of the grooves as its length:width ratio is about 1.1:1. This appears to be in line with the results from Xie and Luttge (Figure 5.8), where primary cells from the rat cortex were cultured on nanogrooves.

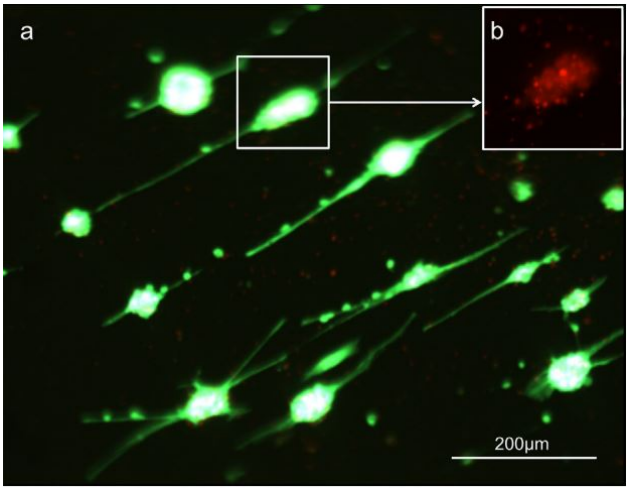

Figure 5.8: Primary cells from the cortex after 8 DIV on nanogrooves [88].

5.3 Conclusion

The numerical model as described in Chapter 4 is successfully applied to a variation of different geometries. In the conical geometry, the cell remained within the cone and had symmetric stresses. The chessboard-like structure caused the cell to either remain on top, or slip between the pillars and take on a cuboidal shape. TopoChip and nanogrooved surface are based on earlier cell culturing experiments and can be used to validate the model.

6 Discussion

6.1 Towards a BoC Device for Single Cell Analysis & Cell Fate Control

Microsieve-like structures have been described in the literature for multiple decades and examples of the first to resemble the shape also incorporated in the µSEA [91] are by van Rijn et al [92] and Kuiper et al. [93], from respectively 1995 and 2000. When it comes to the latest studies related to the microsieve, two lines of research are of importance: those about the fabrication, cell trapping and cell culturing on microsieve(-like) devices as well as the studies on cell fate control by means of mechanical cues through the substrate topography. The findings of these two studies together gives information about how to fabricate a sieve on which cells can be caught and cultured in a way that is repeatable and in which cell fate and network formation can be influenced in a way befitting the experiments

Here, a short overview of the development of the fabrication, cell trapping and cell culturing on microsieve(-like) devices is presented. The microsieve electrode array (µSEA) was developed by Schurink et al. for his PhD studies [39]. In Appendix A.2, more is explained about its workings and fabrication process. This device formed a step forward from the very common microelectrode arrays (MEA). MEAs are (or then were) planar devices and do therefore not support 3D cell culturing [94, 95]. Therefore, cells are also randomly seeded on them, rather than having structured, organised and most of all repeatable culturing possibilities [96]. The µSEA was a step forward as it implemented 3D micropores, which keep the cell's 3D morphology and also organize their positions in relation to each other.

Initially the cells were trapped into the micropores through a process which involved a hand-operated syringe. This method damaged the cells, was uncontrolled in general and the performance varied significantly [97]. The next improvement was trapping the cells in the µSEA through capillary pumping, which is explained in more detail in Appendix A.1. This method provides a controlled manner to trap the cells with a controlled flow velocity, varying from 5 to 10.4 µm/s.

The µSEA fabrication process includes many different and complicated steps. Because of this and the required materials and tools, the fabrication process is not cost-effective at small batch size. Therefore, a replica molding process was developed by Moonen et al. [11]. This fabrication process is described in more detail in Section 3.3. To this type of microsieve, the same capillary pumping method was applied, which resulted in trapping efficiencies of 80% and cell survival rates of 90% after 7 DIV.

The latest two improvements were in the field of the electrode integration and gaining laser ablation fidelity. The former describes a new concept in which the 3D sieving structure and the electrodes are separated [55]. The fabrication of the electrodes and the integration of these into the sieve is the most complicated part of the fabrication process and also makes it expensive. By separating the electrodes from the rest of the sieve, the relatively cheap polymer can be interchanged for each experiment and plugged onto the reusable electrodes. The fabrication and especially the laser ablation process of the NOA81 microsieve were also improved further upon [12]. The fabrication process is made more robust and the influences of the different parameters is quantified. The NOA81 sieve foil can be spin-coated to a defined thickness, which also positively influence the focal depth and pulse count of the laser ablation process. The parameters were determined to create the through hole of the best quality.

6.2 How the Results of this Study can Benefit AD Treatment Development

As mentioned in Section 6.1, there are two lines of research important for the further development of the microsieve. The first is summarized in the previous section. The second, on cell faith control by means of mechanical cues through the substrate topography has been abundantly described in the literature [98, 29, 88, 99, 100, 101, 60, 102, 103]. These *in vitro* experimental studies are valuable when it comes to developing BoC devices, to better understand the workings of the brain and treatments for neurodegenerative diseases for example. However, one approach which could be of immense added value for these *in vitro* experiments, is not yet as present in the literature: *in silico* modeling of cell behaviour.

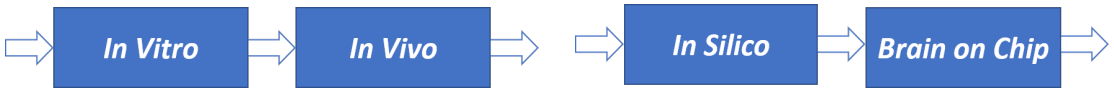

(a) Current workflow. (b) Desirable workflow.

Figure 6.1: The current workflow of the preclinical phase in drug development and the desired workflow.

The current workflow in the preclinical phase of drug development (Figure 6.1a), consist of outdated 2D and 3D *in vitro* cell culturing methods in combination with unreliable, unethical and expensive *in vivo* animal tests. As a result, 99.6% of the drugs for Alzheimer's disease fail in the clinical trial phase [7]. Using BoC devices, it is already better possible to predict the effectiveness of drugs (Figure 6.1b). By combining this approach with *in silico* models to better predict cell response to substrate topographies(, chemicals, biological stimuli, etc.), the design process for appropriate BoC devices can be made more efficient, time- and cost-wise. This would also make it more attractive for pharmaceutical companies to invest in research on, for example, Alzheimer's treatment.

In this study, an *in silico* model was developed to predict cell response to the physical microenvironment of the micropores of a microsieve. The development of this model started with an analysis of the fabrication process of the NOA81 microsieve. From this analysis, it was concluded that the laser ablation process was the most promising step of the fabrication process to fabricate mechanical cues in the 3D micropores. It was found that through the laser ablation process, an almost unlimited amount of different physical microenvironments can be created. For a first exploratory test, a selection of 38 promising configurations was fabricated. With the current settings for the focal height, the micropores ablated from the rear side of the device were the most accurate, followed by the micropores ablated from the front. The micropores ablated from two sides yielded the least accurate geometries and often had overlapping holes. Also, it was found that the holes had different diameters depending on the point of entry of the laser and the position of the hole in the micropore.

Although the holes ablated from the rear of the device gave the most accurate results for the current settings of the focal height, the focal height can definitely be tuned to get results of the same quality for holes ablated from the front. In fact, the settings of the laser should be optimized for each point at which the micropore is ablated. Slight deviations in position and hole size can have a large influence on the mechanical cues on the cell, and eventually the cell behaviour.

Using the results from fabrication experiments, the *in silico* cell model was developed. This model is based on finite element method (FEM) models for atomic force microscopy (AFM) indentations. Such semi-3D, semi-dynamic models consist of two components: the continuous model for the membrane, cytoplasm and nucleus as well as the tensegrity model to describe the cytoskeleton, nucleoskeleton and intermediate filaments. Because the AFM indentation models did not incorporate gravity, the values for the bulk properties of the model had to be redetermined. These values were obtained by evaluating the shape of a cell on a flat surface and in a micropore. However, they still have to be validated further, which is difficult since few similar dynamic 3D cell models exist. The behaviour of the *virtual cell* by Heydari et al. [90], was evaluated by comparing the shape of the model and experimental results on grooved substrates. The same experimental data cannot be used to validate the model developed in this study, as in Heydari et al. mesenchymal cells are used. These are almost twice the size of the cells in the model created in this study and do not necessarily have the same mechanical properties. Nevertheless, a similar approach with SH-SY5Y cells on a grooved substrate could be used to validate the model developed in this study, and to tune the parameters for appropriate response to the substrate. Also, the experimental data from Xie et al. and Bastiaens et al. could be used for this, though neither used a similar cells as in the numerical model [88, 101].

The *in silico* model was used to determine the mechanical cues on cells for 38 different configurations of the geometries in the micropores. The first important result is that cells in micropores ablated from the rear hold their 3D morphology significantly better than those in micropores ablated from the front. A disadvantage of the model that was found during these 38 simulations, is that when the shape of the cell becomes concave, the cytoskeleton can penetrate the membrane. In most configurations, this is not or barely the case, but this

should be kept in mind when evaluating more complex geometries. In the end, six different configurations were found, which are expected to influence the polarization process of a cell significantly.

The 3D model is definitely not perfect at the moment, as the parameters still require further validation. However, it is already a helpful tool to get an idea of how cells will react to different geometries. Especially when working at the microscale, it is sometimes difficult to imagine how things will behave. For example, cells in micropores which are ablated from the front in the middle, maintain their 3D morphology a lot less than assumed by the top view SEM images. Hence, this model should be used to get an idea of how a cell will approximately sit in a certain physical microenvironment. This will help in deciding which geometries to fabricate when developing specific mechanical cues. Moreover, the model is not complete. Many more aspects can be implemented, like the hydrodynamic shear force from the capillary pumping during cell seeding (Appendix A.1), the influence of water pressure and adhesions etc. This model should be seen as a framework which has decent predictive value for mechanical cues in 3D micropores, but can be extended to more accuracy and incorporate more aspects.

6.3 What the Results of this Study Mean for the Future of the Microsieve

In Section 6.1, an overview of the development of the microsieve up and until now is given. In this study, a numerical model was created to evaluate the behaviour of cells under different mechanical cues. This model can be used to take the next step in the development of the microsieve. Currently, only a limited amount of geometries have been tested, which gives basic insight into a cell's response to different mechanical cues.

By studying a larger variety of geometries, more meaningful conclusions can be drawn. This could include an extended study of the through hole size, positions and draft angle. Such a study could help determine fabrication tolerances of the microsieve when trying to achieve a certain mechanical cue. In Chapter 5, the numerical was already applied to a variance of geometries, some of which have already been used in cell experiments. Comparing the outcomes of these experiments is also an important step in further understanding the influence of mechanical cues on cells.

7 Conclusion & Recommendations

A 3D, fully dynamic cell model capable of predicting a cell's response to different substrate topographies was developed. This model consists of a continuous part for the membrane, cytoplasm and nucleus as well as a tensegrity model to represent the cytoskeleton, nucleoskeleton and intermediate filaments. This model was used to simulate the behaviour of a cell in a NOA81 microsieve. By changing the physical microenvironment within such a microsieve, the mechanical cues that a cell experiences can be influenced, and thereby the polarization and network formation process.

The fabrication process of the NOA81 microsieve was analysed and it was found that the physical microenvironment of the micropores could best be altered through the laser ablation step of the process. A set of 38 promising configurations of laser ablation holes in the micropore was then selected. These were fabricated and the optical microscopy images of the results were used to model the micropores in 3D, so that they could be used in the simulation model.

From the simulations of these 38 configurations, multiple things were found. First, there is a clear difference in cell morphology between holes ablated from the front or rear side of the device. In the case of the latter, the cells keep their 3D morphology much better. The second point that resulted from the simulations, is that the model gives less accurate results if large parts of the cell have a concave morphology. This causes the tensegrity model to go outside of the membrane and thereby give an unrealistic cell morphology. Finally, from the 38 configurations which were tested, six gave a distinct directional mechanical cue to the cell. In all these six configurations, this cue is present on a sharp corner in the micropore. Moreover, of the six promising configurations two give a horizontal/vertical and four a diagonal cue.

Those six configurations comprise the answer to the research questions, which is how we can control the micromechanics in the micropore to control cell fate of the NOA81 microsieve. However, these configurations still have to be validated by means of a biological experiment. With these results, not only the research question is answered, but the model also provides a framework for a cell model which can help with the development of other BoC or even other OoC devices. Nevertheless, the model can currently give some insight into the mechanics of a cell in different physical microenvironments. Further experimental validation and tuning of the mechanical properties of the model is necessary, however. A good approach for this would be to conduct experiments with cells on different substrate topographies and analyse their behaviour, then comparing the results to the *in silico* simulation model.

In conclusion, the numerical model for predicting a cell's response that was developed, was used to select six configurations that showed the most promising results for controlling cell fate. Even though the model still has to be validated, it already provides better understanding of a cell's response to specific mechanical cues.

Bibliography

[1] World Alzheimer Report, "World Alzheimer Report 2019, Attitudes to dementia," *Alzheimer's Disease International: London*, pp. 1–15, 2019.

[2] Alzheimer's Disease International, "68% 2050 9.4," 2015.

[3] R. Brookmeyer, E. Johnson, K. Ziegler-Graham, and H. M. Arrighi, "Forecasting the global burden of Alzheimer's disease," *Alzheimer's and Dementia*, vol. 3, no. 3, pp. 186–191, 2007.

[4] P. Scommegna, "Dementia Cases Expected to Triple by 2050 as World Population Ages," Tech. Rep. November 2012, Population Reference Bureau, 2012.

[5] A. Wimo, B. Winblad, and L. Jönsson, "The worldwide societal costs of dementia: Estimates for 2009," *Alzheimer's and Dementia*, vol. 6, no. 2, pp. 98–103, 2010.

[6] H. Hippius and G. Neundörfer, "The discovery of Alzheimer's disease.pdf," *Dialogue in Clinical Neuroscience*, vol. 5, no. 1, pp. 101–108, 2003.

[7] J. Cummings, "Lessons Learned from Alzheimer Disease: Clinical Trials with Negative Outcomes," *Clinical and Translational Science*, vol. 11, no. 2, pp. 147–152, 2018.

[8] A. E. Oxford, E. S. Stewart, and T. T. Rohn, "Clinical Trials in Alzheimer's Disease: A Hurdle in the Path of Remedy," *International Journal of Alzheimer's Disease*, vol. 2020, 2020.

[9] Kshitiz, J. Park, P. Kim, W. Helen, A. J. Engler, A. Levchenko, and D. H. Kim, "Control of stem cell fate and function by engineering physical microenvironments," *Integrative Biology (United Kingdom)*, vol. 4, no. 9, pp. 1008–1018, 2012.

[10] B. Ladoux, R. M. Mège, and X. Trepat, "Front-Rear Polarization by Mechanical Cues: From Single Cells to Tissues," *Trends in Cell Biology*, vol. 26, no. 6, pp. 420–433, 2016.

[11] E. Moonen, R. Luttge, and J. P. Frimat, "Single cell trapping by capillary pumping using NOA81 replica moulded stencils," *Microelectronic Engineering*, vol. 197, no. October 2017, pp. 1–7, 2018.

[12] R. Sabahi-Kaviani and R. Luttge, "Gaining micropattern fidelity in an noa81 microsieve laser ablation process," *Micromachines*, vol. 12, no. 1, pp. 1–13, 2021.

[13] Y. Seto and M. Eiraku, "Toward the formation of neural circuits in human brain organoids," *Current Opinion in Cell Biology*, vol. 61, pp. 86–91, 2019.

[14] I. Raimondi, L. Izzo, M. Tunesi, M. Comar, D. Albani, and C. Giordano, "Organ-On-A-Chip in vitro Models of the Brain and the Blood-Brain Barrier and Their Value to Study the Microbiota-Gut-Brain Axis in Neurodegeneration," *Frontiers in Bioengineering and Biotechnology*, vol. 7, no. January, 2020.

[15] A. P. Haring and B. N. Johnson, "Brain-on-a-chip systems for modeling disease pathogenesis," in *Organ-on-a-chip: Engineered Microenvironments for Safety and Efficacy Testing*, pp. 215–232, Elsevier Inc., 2019.

[16] A. Woodruff, "What is a neuron? - Queensland Brain Institute - University of Queensland."

[17] T. Takano, C. Xu, Y. Funahashi, T. Namba, and K. Kaibuchi, "Neuronal polarization," *Development (Cambridge)*, vol. 142, no. 12, pp. 2088–2093, 2015.

[18] M. Schelski and F. Bradke, "Neuronal polarization: From spatiotemporal signaling to cytoskeletal dynamics," *Molecular and Cellular Neuroscience*, vol. 84, pp. 11–28, 2017.

[19] O. Kilic, D. Pamies, E. Lavell, P. Schiapparelli, Y. Feng, T. Hartung, A. Bal-Price, H. T. Hogberg, A. Quinones-Hinojosa, H. Guerrero-Cazares, and A. Levchenko, "Brain-on-a-chip model enables analysis of human neuronal differentiation and chemotaxis," *Lab on a Chip*, vol. 16, no. 21, pp. 4152–4162, 2016.

[20] "cytoskeleton — Description, Structure, & Function — Britannica."

[21] D. A. Fletcher and R. D. Mullins, "Cell mechanics and the cytoskeleton," jan 2010.

[22] S. A. Adam, "The nucleoskeleton," *Cold Spring Harbor Perspectives in Biology*, vol. 9, no. 2, 2017.

[23] S. I. Jeong, J. H. Kwon, J. I. Lim, S. W. Cho, Y. Jung, W. J. Sung, S. H. Kim, Y. H. Kim, Y. M. Lee, B. S. Kim, C. Y. Choi, and S. J. Kim, "Mechano-active tissue engineering of vascular smooth muscle using pulsatile perfusion bioreactors and elastic PLCL scaffolds," *Biomaterials*, vol. 26, no. 12, pp. 1405–1411, 2005.

[24] C. M. Lo, H. B. Wang, M. Dembo, and Y. L. Wang, "Cell movement is guided by the rigidity of the substrate," *Biophysical Journal*, vol. 79, no. 1, pp. 144–152, 2000.

[25] S. Kapur, D. J. Baylink, and K. H. Lau, "Fluid flow shear stress stimulates human osteoblast proliferation and differentiation through multiple interacting and competing signal transduction pathways," *Bone*, vol. 32, no. 3, pp. 241–251, 2003.

[26] K. M. Yamada and E. Cukierman, "Modeling Tissue Morphogenesis and Cancer in 3D," *Cell*, vol. 130, no. 4, pp. 601–610, 2007.

[27] J.-P. Frimat, S. Xie, A. Bastiaens, B. Schurink, F. Wolbers, J. den Toonder, and R. Luttge, "Advances in 3D neuronal cell culture," *Journal of Vacuum Science & Technology B, Nanotechnology and Microelectronics: Materials, Processing, Measurement, and Phenomena*, vol. 33, no. 6, p. 06F902, 2015.

[28] H. Wolfenson, B. Yang, and M. P. Sheetz, "Steps in Mechanotransduction Pathways that Control Cell Morphology," *Annual Review of Physiology*, vol. 81, pp. 585–605, 2019.

[29] S. Xie, B. Schurink, F. Wolbers, R. Luttge, and G. Hassink, "Nanoscaffold's stiffness affects primary cortical cell network formation," *Journal of Vacuum Science & Technology B, Nanotechnology and Microelectronics: Materials, Processing, Measurement, and Phenomena*, vol. 32, no. 6, pp. 06FD03–01 – 06FD03–05, 2014.

[30] A. Higuchi, Q. D. Ling, Y. Chang, S. T. Hsu, and A. Umezawa, "Physical cues of biomaterials guide stem cell differentiation fate," *Chemical Reviews*, vol. 113, no. 5, pp. 3297–3328, 2013.

[31] C. Matellan and A. E. Del Río Hernández, "Where No Hand Has Gone Before: Probing Mechanobiology at the Cellular Level," *ACS Biomaterials Science and Engineering*, vol. 5, no. 8, pp. 3703–3719, 2019.

[32] G. McKhann, D. Drachman, M. Folstein, and R. Katzman, "views & reviews Clinical diagnosis of Alzheimer ' s disease :," *Neurology*, vol. 34, no. 7, p. 939, 1984.

[33] A. Francke, I. van der Heide, S. de Bruin, R. Gijsen, R. Poos, M. Veerbeek, T. Wiegers, and B. Willemse, "Een samenhangend beeld van dementie en dementiezorg: kerncijfers, behoeften, zorgaanbod en impact," tech. rep., Staat van Volksgezondheid en Zorg, 2018.

[34] D. J. Selkoe, "Alzheimer ' s Disease : Genes , Proteins , and Therapy," *Physiological Reviews*, vol. 81, no. 2, pp. 741–766, 2001.

[35] "What is Alzheimer's Disease? Symptoms & Causes — alz.org."

[36] "What Happens to the Brain in Alzheimer's Disease? — National Institute on Aging."

[37] v. W. C. BruceBlaus, CC BY-SA 4.0 <https://creativecommons.org/licenses/by-sa/4.0>, "Neuron_Alzheimer."

[38] F. Pistollato, E. L. Ohayon, A. Lam, G. R. Langley, T. J. Novak, D. Pamies, G. Perry, E. Trushina, R. S. Williams, A. E. Roher, T. Hartung, S. Harnad, N. Barnard, M. C. Morris, M. C. Lai, R. Merkley, and P. Charukeshi Chandrasekera, "Alzheimer disease research in the 21st century: Past and current failures, new perspectives and funding priorities," *Oncotarget*, vol. 7, no. 26, pp. 38999–39016, 2016.

[39] B. Schurink, *Microfabrication and microfluidics for 3D brain-on-chip*. PhD thesis, University of Twente, 2016.

[40] L. S. Schneider, M. Sano, and A. Dement Author manuscript, "Current Alzheimer's disease clinical trials: Methods and placebo outcomes NIH Public Access Author Manuscript," *Alzheimers Dement*, vol. 5, no. 5, pp. 388–397, 2009.

[41] E. Zenaro, G. Piacentino, and G. Constantin, "The blood-brain barrier in Alzheimer's disease," *Neurobiology of Disease*, vol. 107, pp. 41–56, 2017.

[42] F. Mangialasche, A. Solomon, B. Winblad, P. Mecocci, and M. Kivipelto, "Alzheimer's disease: clinical trials and drug development," *The Lancet Neurology*, vol. 9, no. 7, pp. 702–716, 2010.

[43] A. Kumar, A. Singh, and Ekavali, "A review on Alzheimer's disease pathophysiology and its management: An update," *Pharmacological Reports*, vol. 67, no. 2, pp. 195–203, 2015.

[44] A. Mencattini, F. Mattei, G. Schiavoni, A. Gerardino, L. Businaro, C. Di Natale, and E. Martinelli, "From petri dishes to organ on chip platform: The increasing importance of machine learning and image analysis," *Frontiers in Pharmacology*, vol. 10, no. February, pp. 1–4, 2019.

[45] J. Hoeng, D. Bovard, and M. C. Peitsch, *Organ-on-a-chip: Engineered microenvironments for safety and efficacy testing*. Academic Press, Elsevier, 2019.

[46] M. F. Hasan and Y. Berdichevsky, "Neural circuits on a chip," *Micromachines*, vol. 7, no. 9, pp. 1–15, 2016.

[47] M. Jorfi, C. D'Avanzo, R. E. Tanzi, D. Y. Kim, and D. Irimia, "Human Neurospheroid Arrays for In Vitro Studies of Alzheimer's Disease," *Scientific Reports*, vol. 8, no. 1, pp. 1–13, 2018.

[48] C. Frantz, K. M. Stewart, and V. M. Weaver, "The extracellular matrix at a glance," *Journal of Cell Science*, vol. 123, no. 24, pp. 4195–4200, 2010.

[49] T. Kolenda, M. Kapałczyńska, W. Przybyła, M. Zajączkowska, A. Teresiak, V. Filas, M. Ibbs, R. Bliźniak, Ł. Łuczewski, and K. Lamperska, "2D and 3D cell cultures-a comparison of different types of cancer cell cultures," *State of the art paper*, vol. 14, no. 4, pp. 910–919, 2016.

[50] S. N. Bhatia and D. E. Ingber, "Microfluidic organs-on-chips," *Nature Biotechnology*, vol. 32, no. 8, pp. 760–772, 2014.

[51] Thomassen, "Organ on Chip in Development (ORCHID)," Tech. Rep. 766884, ORCHID, 2018.

[52] F. Zheng, F. Fu, Y. Cheng, C. Wang, Y. Zhao, and Z. Gu, "Organ-on-a-Chip Systems: Microengineering to Biomimic Living Systems," *Small*, vol. 12, no. 17, pp. 2253–2282, 2016.

[53] D. Huh, G. A. Hamilton, and D. E. Ingber, "From 3D cell culture to organs-on-chips," *Trends in Cell Biology*, vol. 21, no. 12, pp. 745–754, 2011.

[54] B. Schurink, J. W. Berenschot, R. M. Tiggelaar, and R. Luttge, "Highly uniform sieving structure by corner lithography and silicon wet etching," *Microelectronic Engineering*, vol. 144, pp. 12–18, 2015.

[55] Y. Demircan Yalcin and R. Luttge, "3D-electrode integrated microsieve structure as a rapid and cost-effective single neuron detector," *Journal of Vacuum Science & Technology B*, vol. 38, no. 6, p. 063202, 2020.

[56] A. Gross, J. Schoendube, S. Zimmermann, M. Steeb, R. Zengerle, and P. Koltay, "Technologies for single-cell isolation," *International Journal of Molecular Sciences*, vol. 16, no. 8, pp. 16897–16919, 2015.

[57] B. Schurink, R. M. Tiggelaar, J. G. Gardeniers, and R. Luttge, "Fabrication and characterization of microsieve electrode array (μSEA) enabling cell positioning on 3D electrodes," *Journal of Micromechanics and Microengineering*, vol. 27, no. 1, 2017.

[58] S. Halldorsson, E. Lucumi, R. Gómez-Sjöberg, and R. M. Fleming, "Advantages and challenges of microfluidic cell culture in polydimethylsiloxane devices," *Biosensors and Bioelectronics*, vol. 63, pp. 218–231, 2015.

[59] P. Wägli, A. Homsy, and N. F. De Rooij, "Norland optical adhesive (NOA81) microchannels with adjustable surface properties and high chemical resistance against IR-transparent organic solvents," *Procedia Engineering*, vol. 5, pp. 460–463, 2010.

[60] A. Bastiaens, S. Xie, and R. Luttge, "Nanogroove-enhanced hydrogel scaffolds for 3D neuronal cell culture: An easy access brain-on-chip model," *Micromachines*, vol. 10, no. 10, 2019.

[61] J. Xie, W. Liu, M. R. MacEwan, Y. C. Yeh, S. Thomopoulos, and Y. Xia, "Nanofiber Membranes with Controllable Microwells and Structural Cues and Their Use in Forming Cell Microarrays and Neuronal Networks," *Small (Weinheim an der Bergstrasse, Germany)*, vol. 4, no. 10, pp. 293–297, 2008.

[62] H. V. Unadkat, M. Hulsman, K. Cornelissen, B. J. Papenburg, R. K. Truckenmuller, G. F. Post, M. Uetz, M. J. Reinders, D. Stamatialis, C. A. Van Blitterswijk, and J. De Boer, "An algorithm-based topographical biomaterials library to instruct cell fate," *Proceedings of the National Academy of Sciences of the United States of America*, vol. 108, no. 40, pp. 16565–16570, 2011.

[63] F. Xue, A. B. Lennon, K. K. McKayed, V. A. Campbell, and P. J. Prendergast, "Effect of membrane stiffness and cytoskeletal element density on mechanical stimuli within cells: an analysis of the consequences of ageing in cells," *Computer Methods in Biomechanics and Biomedical Engineering*, vol. 18, no. 5, pp. 468–476, 2015.

[64] J. Mao, W. Ruan, M. Chen, Y. Wang, and H. Yang, "Finite element modeling of mechanical properties of cancer cells," *SPIE*, vol. 1119038, no. November 2019, p. 118, 2019.

[65] H. Bowne-Anderson, M. Zanic, M. Kauer, and J. Howard, "Microtubule dynamic instability: A new model with coupled GTP hydrolysis and multistep catastrophe," *BioEssays*, vol. 35, no. 5, pp. 452–461, 2013.

[66] N. B. Gudimchuk, E. V. Ulyanov, E. O'Toole, C. L. Page, D. S. Vinogradov, G. Morgan, G. Li, J. K. Moore, E. Szczesna, A. Roll-Mecak, F. I. Ataullakhanov, and J. Richard McIntosh, "Mechanisms of microtubule dynamics and force generation examined with computational modeling and electron cryotomography," *Nature Communications*, vol. 11, no. 1, pp. 1–15, 2020.

[67] M. P. Van Veen and J. Van Pelt, "NEURITIC GROWTH RATE DESCRIBED BY MODELING MICROTUBULE DYNAMICS," *Pergamon Bulletin of Mathematical Biology*, vol. 56, no. 2, pp. 249–273, 1994.

[68] F. Zubler and R. Douglas, "A framework for modeling the growth and development of neurons and networks," *Frontiers in Cellular Neuroscience*, vol. 10, no. 02, 2009.

[69] J. E. Lugo, R. Doti, K. Ray, S. L. Kothari, G. S. Withers, and J. Faubert, "A simple dynamic model that accounts for regulation of neuronal polarity," *Journal of Integrative Neuroscience*, vol. 17, no. 4, 2018.

[70] J. Chen and G. Lu, "Finite element modelling of nanoindentation based methods for mechanical properties of cells," *Journal of Biomechanics*, vol. 45, no. 16, pp. 2810–2816, 2012.

[71] N. Caille, O. Thoumine, Y. Tardy, and J. J. Meister, "Contribution of the nucleus to the mechanical properties of endothelial cells," *Journal of Biomechanics*, vol. 35, no. 2, pp. 177–187, 2002.

[72] P. K. Purohit, "Tension Dependent Growth and Retraction of Neurites," *Procedia IUTAM*, vol. 12, pp. 185–192, 2015.

[73] J. Zhao, F. Manuchehrfar, and J. Liang, "Cell–substrate mechanics guide collective cell migration through intercellular adhesion: a dynamic finite element cellular model," *Biomechanics and Modeling in Mechanobiology*, vol. 19, no. 5, pp. 1781–1796, 2020.

[74] L. Wang, L. Wang, L. Xu, and W. Chen, "Finite Element Modelling of Single Cell Based on Atomic Force Microscope Indentation Method," *Computational and Mathematical Methods in Medicine*, vol. 2019, 2019.

[75] J. G. McGarry, P. J. Prendergast, B. Ashton, and J. Klein-Nulend, "A three-dimensional finite element model of an adherent eukaryotic cell," *European Cells and Materials*, vol. 7, no. 2000, pp. 27–34, 2004.

[76] E. Gladilin, P. Gonzalez, and R. Eils, "Dissecting the contribution of actin and vimentin intermediate filaments to mechanical phenotype of suspended cells using high-throughput deformability measurements and computational modeling," *Journal of Biomechanics*, vol. 47, no. 11, pp. 2598–2605, 2014.

[77] G. De Santis, A. B. Lennon, F. Boschetti, B. Verhegghe, P. Verdonck, and P. J. Prendergast, "How can cells sense the elasticity of a substrate? an analysis using a cell tensegrity model," *European Cells and Materials*, vol. 22, pp. 202–213, 2011.

[78] M. Arvidsson, L. Ringstad, L. Skedung, K. Duvefelt, and M. W. Rutland, "Feeling fine - the effect of topography and friction on perceived roughness and slipperiness," *Biotribology*, vol. 11, no. January, pp. 92–101, 2017.

[79] Z. Javanbakht and A. Öchsner, "Advanced finite element simulation with MSC marc: Application of user subroutines," *Advanced Finite Element Simulation with MSC Marc: Application of User Subroutines*, no. May, pp. 1–333, 2017.

[80] D. Stamenović, J. J. Fredberg, N. Wang, J. P. Butler, and D. E. Ingber, "A microstructural approach to cytoskeletal mechanics based on tensegrity," *Journal of Theoretical Biology*, vol. 181, no. 2, pp. 125–136, 1996.

[81] P. J. G. Schreurs, "One-Dimensional Material Behavior," tech. rep., TU Eindhoven, 2015.

[82] J. H. Snoeijer, A. Pandey, M. A. Herrada, and J. Eggers, "The relationship between viscoelasticity and elasticity: Viscoelasticity and elasticity," 2020.

[83] M. M. Terzi, M. Deserno, and J. F. Nagle, "Mechanical properties of lipid bilayers: A note on the Poisson ratio," *Soft Matter*, vol. 15, no. 44, pp. 9085–9092, 2019.

[84] S. Heyden and M. Ortiz, "Investigation of the influence of viscoelasticity on oncotripsy," *Computer Methods in Applied Mechanics and Engineering*, vol. 314, pp. 314–322, 2017.

[85] T. Frisch and O. Thoumine, "Predicting the kinetics of cell spreading," *Journal of Biomechanics*, vol. 35, no. 8, pp. 1137–1141, 2002.

[86] Norland, "NOA81."

[87] F. Hulshof, J. de Boer, and D. F. Stamatialis, "TopoChip: technology for instructing cell fate and morphology via designed surface topography," 2016.

[88] S. Xie and R. Luttge, "Imprint lithography provides topographical nanocues to guide cell growth in primary cortical cell culture," *Microelectronic Engineering*, vol. 124, pp. 30–36, 2014.

[89] F. F. Hulshof, Y. Zhao, A. Vasilevich, N. R. Beijer, M. de Boer, B. J. Papenburg, C. van Blitterswijk, D. Stamatialis, and J. de Boer, "NanoTopoChip: High-throughput nanotopographical cell instruction," *Acta Biomaterialia*, vol. 62, pp. 188–198, 2017.

[90] T. Heydari, M. Heidari, O. Mashinchian, M. Wojcik, K. Xu, M. J. Dalby, M. Mahmoudi, and M. R. Ejtehadi, "Development of a Virtual Cell Model to Predict Cell Response to Substrate Topography," *ACS Nano*, vol. 11, no. 9, pp. 9084–9092, 2017.

[91] B. Schurink, R. M. Tiggelaar, J. G. Gardeniers, and R. Luttge, "Fabrication and characterization of microsieve electrode array (μSEA) enabling cell positioning on 3D electrodes," *Journal of Micromechanics and Microengineering*, vol. 27, no. 1, 2017.

[92] C. J. van Rijn and M. C. Elwenspoek, "Micro filtration membrane sieve with silicon micro machining for industrial and biomedical applications," *Proceedings of the IEEE Micro Electro Mechanical Systems*, no. January, pp. 83–87, 1995.

[93] S. Kuiper, *Development and application of microsieves.* PhD thesis, University of Twente, 2000.

[94] U. Egert and T. Meyer, "Heart on a chip - Extracellular multielectrode recordings from cardiac myocytes in vitro," *Practical Methods in Cardiovascular Research*, no. March 2014, pp. 432–453, 2005.

[95] F. O. Morin, Y. Takamura, and E. Tamiya, "Investigating neuronal activity with planar microelectrode arrays: Achievements and new perspectives," *Journal of Bioscience and Bioengineering*, vol. 100, no. 2, pp. 131–143, 2005.

[96] S. Xie, B. Schurink, E. J. W. Berenschot, R. M. Tiggelaar, H. J. G. E. Gardeniers, and R. Luttge, "Displacement Talbot lithography nanopatterned microsieve array for directional neuronal network formation in brain-on-chip," *Journal of Vacuum Science & Technology B, Nanotechnology and Microelectronics: Materials, Processing, Measurement, and Phenomena*, vol. 34, no. 6, p. 06KI02, 2016.

[97] J.-P. Frimat, B. Schurink, and R. Luttge, "Passive pumping for the parallel trapping of single neurons onto a microsieve electrode array," *Journal of Vacuum Science & Technology B, Nanotechnology and Microelectronics: Materials, Processing, Measurement, and Phenomena*, vol. 35, no. 6, p. 06GA01, 2017.

[98] J.-P. Frimat, S. Xie, A. Bastiaens, B. Schurink, F. Wolbers, J. den Toonder, and R. Luttge, "Advances in 3D neuronal cell culture," *Journal of Vacuum Science & Technology B, Nanotechnology and Microelectronics: Materials, Processing, Measurement, and Phenomena*, vol. 33, no. 6, p. 06F902, 2015.

[99] A. J. Bastiaens, J. P. Frimat, T. van Nunen, B. Schurink, E. F. Homburg, and R. Luttge, "Advancing a MEMS-Based 3D Cell Culture System for in vitro Neuro-Electrophysiological Recordings," *Frontiers in Mechanical Engineering*, vol. 4, no. December, pp. 1–10, 2018.

[100] A. J. Bastiaens, S. Xie, and R. Luttge, "Investigating the interplay of lateral and height dimensions influencing neuronal processes on nanogrooves," *Journal of Vacuum Science & Technology B*, vol. 36, no. 6, p. 06J801, 2018.

[101] A. J. Bastiaens, S. Xie, D. A. Mustafa, J. P. Frimat, J. M. den Toonder, and R. Luttge, "Validation and optimization of an image-based screening method applied to the study of neuronal processes on nanogrooves," *Frontiers in Cellular Neuroscience*, vol. 12, no. 2018, pp. 1–14, 2018.

[102] A. Bastiaens, R. Sabahi-Kaviani, and R. Luttge, "Nanogrooves for 2D and 3D Microenvironments of SH-SY5Y Cultures in Brain-on-Chip Technology," *Frontiers in Neuroscience*, vol. 14, pp. 1–11, jun 2020.

[103] A. Bastiaens, J.-P. Frimat, T. van Nunen, and R. Luttge, "Exploiting nanogroove-induced cell culture anisotropy to advance in vitro brain models," *Journal of Vacuum Science & Technology B*, vol. 37, no. 6, p. 061802, 2019.

[104] J.-P. Frimat, B. Schurink, and R. Luttge, "Passive pumping for the parallel trapping of single neurons onto a microsieve electrode array," *Journal of Vacuum Science & Technology B, Nanotechnology and Microelectronics: Materials, Processing, Measurement, and Phenomena*, vol. 35, no. 6, p. 06GA01, 2017.

[105] A. D. Castiaux, D. M. Spence, and R. S. Martin, "Review of 3D cell culture with analysis in microfluidic systems," *Analytical Methods*, vol. 11, no. 33, pp. 4220–4232, 2019.

[106] E. J. Berenschot, N. Burouni, B. Schurink, J. W. Van Honschoten, R. G. Sanders, R. Truckenmuller, H. V. Jansen, M. C. Elwenspoek, A. A. Van Apeldoorn, and N. R. Tas, "3D nanofabrication of fluidic components by corner lithography," *Small*, vol. 8, no. 24, pp. 3823–3831, 2012.

[107] S. W. Moore and M. P. Sheetz, "Differentiation and Repair," *Developmental Neurbiology*, vol. 71, no. 11, pp. 1090–1101, 2012.

A Appendix A

A.1 Hydrodynamics

The hydrodynamic flow through the microsieve can be induced by different hydrodynamic effects. In Figure A.1, a microsieve is shown under which first a droplet free of cells is placed into a petri dish. Then a drop containing the to-trap cells (pumping drop) is placed on top of the sieve.

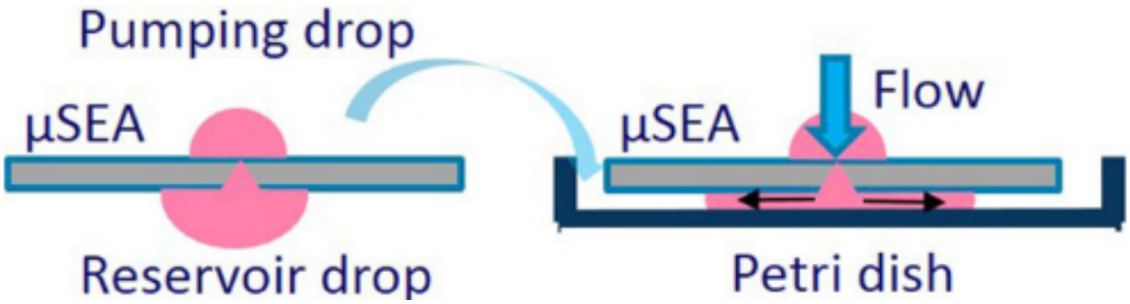

Figure A.1: Capillary pumping in a μSEA [104]. The pumping drop start to flow through the sieve due to i) gravity ii) capillary force as a result of the material wettability iii) pressure differences between drops [11].

In this case, three different effects induce flow from the top drop through the pores. First and most straightforward, there is gravity. Then there are the capillary forces, which are induced by the intermolecular forces between the liquid and the sieve material. Finally, there is the passive pumping, as visualized in Figure A.2.

This collective pumping method is simple, fast (between 8.6 and 13.3 μm/s) and does not require pumping equipment, which reduces cost and footprint [104]. Trapping efficiencies are approximately 80% and the cell survival rate after a week is 90%, though this second number may actually be higher as it is also possible already dead neurons were trapped. Moreover, the passive behaviour of the pumping method ensures that cell damage is minimized and that cells do not deform and go through the pores as a result of the applied pressure.

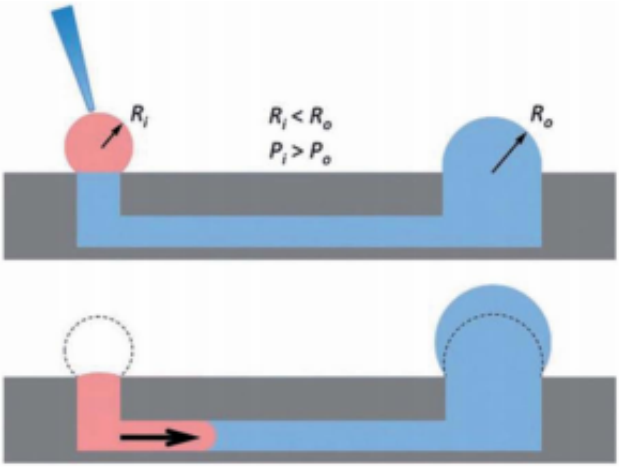

Figure A.2: The passive pumping mechanism. This mechanism is based on the size difference of two droplets. Due to the capillary forces within a drop, the pressure in a small drop will be higher than in a larger drop. Because of this pressure difference flow is induced [105].

A.2 Microsieve Electrode Array

By trapping individual cells in the pores, single cell analysis within a network of communicating neurons is facilitated. This can give valuable information as cell populations are not homogeneous. Moreover, it makes detection of rare events possible, which can be the cause of disorders. Furthermore, it can be used to do research on the effects of a single cell to a cell population. A specific device can also be used to link multiple neurons to measure their activity (Figure A.3). Such a type of BoC is called a microsieve electrode array (μSEA) [11, 57].

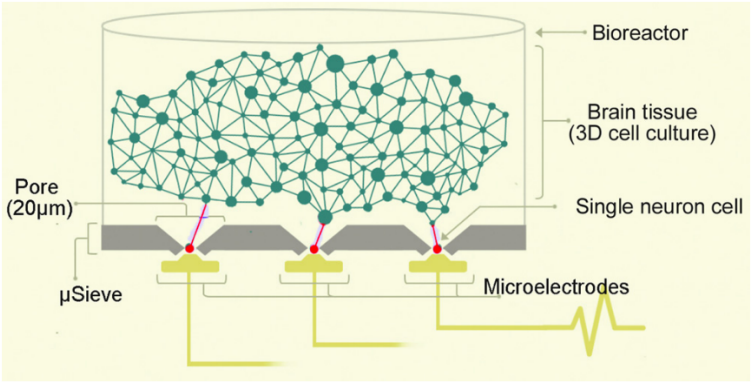

Figure A.3: Schematic overview of a μSEA [11]

The shape of the silicon in this device is created using corner lithography. This is a micro- or nanofabrication technique, which can be used to form structures on sharp corners and edges. There it can e.g. be used to locally create thin films or apertures [106].

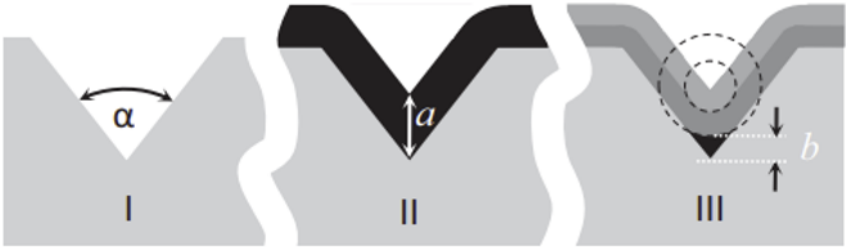

Figure A.4: Schematic overview of corner lithography [106].

In Figure A.4, the process of corner lithography is shown for an inverted pyramidal structure. The structure in this example was created using anisotropic etching of $< 100 >$ silicon applying a square mask opening (Figure A.4(I)). Using low pressure chemical vapor deposition (LPCVD) a layer of silicon nitride of thickness t is deposited. At the corner, the film then gets a thickness:

$$a = \frac{t}{\sin(\frac{\alpha}{2})} \tag{A.1}$$

which in this case is equal to $\sqrt{3}t$ in the corner and $\frac{1}{2}\sqrt{6}t$ in the ribs (Figure A.4(II)). Next the silicon is etched in HF. Depending on the etching time either a microwire structure remains along the ribs, or only a microdot remains in the corner of thickness b (Figure A.4(III)). The process of corner lithography can also be extended to create an aperture in the tip of the pyramid (Figure A.5).

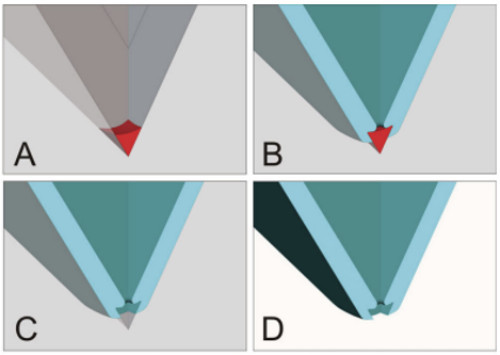

Figure A.5: Further processing of the microdot created by corner lithography to create an aperture. A) There is a microdot present in the tip of the pyramid. B) The silicon is locally oxidized (LOCOS), for a free-standing pyramid. C) Selective etching of the microdot using HF. D) Optional selective etching of the silicon mould [106].

In Figure A.6 the fabrication process steps for a μ-SEA are described. Steps a) to f) in Figure A.6 are performed using corner lithography. In g) the silicon is etched away into a diamond-like shape. At h) the oxide is etched away and subsequently a layer of silicon nitride is deposited and the backside is etched.

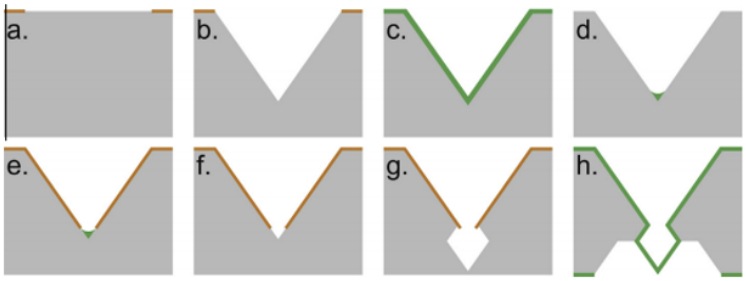

Figure A.6: Fabrication process of a microsieve using back etching [54].

Rather than just doing a back-etch directly after step f) in Figure A.6, first the diamond-shaped cavity is created. The motivation for this is uniform pore size. In Figure A.7, above it can be seen that when the etch plane is somewhat round, the pore size varies significantly. Below the diamond shape cavity is implemented and uniform pore size is achieved.

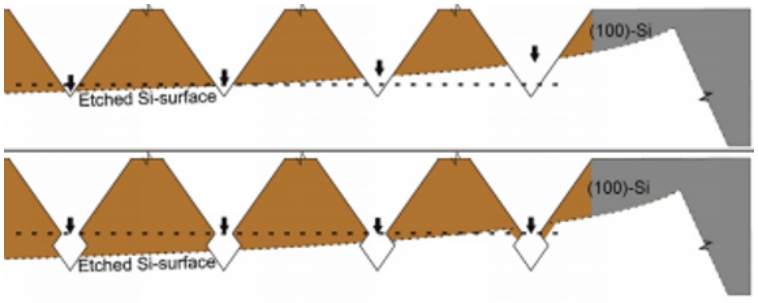

Figure A.7: Effect of back etching for uniform pore size [54].

With the silicon structure finished, the sensors can be integrated into the microsieve to create the final µSEA. This process is described by Schurink et al. [57].

A.3 Alternative Methods for Electrical Measurements in Microsieves

Trapping efficiencies of the NOA81 microsieve are in the order of 80%. However, this value can always deviate. Moreover, it is interesting to know the distribution of the cells among the sieve. Doing this optically is a cumbersome way of determining a go/no-go for further experimentation using the microsieve [55].

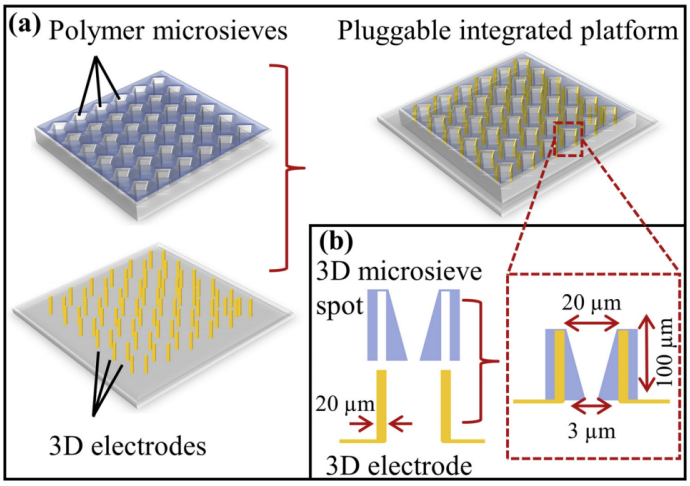

Figure A.8: Schematic overview of a pluggable μSEA, with the general overview (a) and zooming in on one pore (b) [55].

In Figure A.8, the concept for a two-part μSEA is shown as designed by Demircan-Yalcin et al. [55]. The underlying idea is that the microsieve is made using a cost effective method for one time use only and that the electrode array is more robust. The polymer microsieves can then be plugged onto the electrode array for evaluation of the cell distribution in the sieve. Thereby, a go/no-go decision on further experimentation can be made easily.

B Appendix B

B.1 Cell Fate Control in Practice

In the literature, different setups can be found, which are used to control neuronal network formation. These setups are based on but not limited to adhesion, physical confinement, physical cues and neurospheroids [46, 107]. Here, an overview of these setups will be given.

B.1.1 Nanogrooves

Bastiaens et al. used nanogrooves to steer neurite outgrowths (Figure B.1). It was found that the results were similar when using hard (silicon, GPa range) and soft (PDMS, kPa-MPA range) materials for the substrate (respectively 85% and 90% alignment). This gives the impression that the topography has a larger influence on guiding axons than substrate stiffness. On the other hand, substrate stiffness influences the geno- and phenotype of cells and their morphology and function. However, there was also found that the nanogrooves have to be optimized for specific cell types [100].

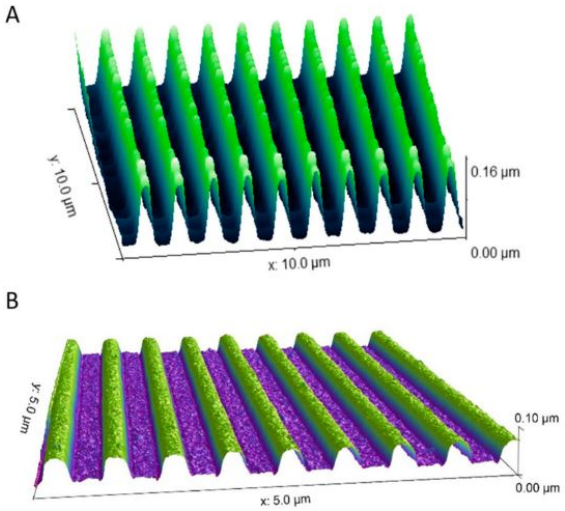

Figure B.1: AFM measurements visualization of nanogrooves with different dimensions [60].

B.1.2 Patterning of Cell Adhesion Molecules

Using a PDMS stamp, cell-adhesive islands can be created on a substrate (Figure B.2). On these islands, neurons can be captured for spatial control. Also, they prefer to grow over these adhesive zones. An important finding here was that neurons with a high amount of potential partners choose many weak connections over a few strong ones [46].

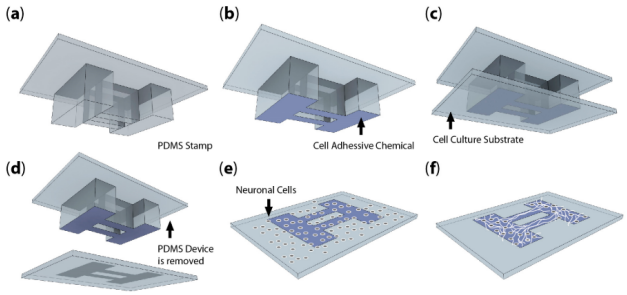

Figure B.2: The fabrication steps for a device which guides neurites outgrowth through adhesion [46].

B.1.3 Physical Confinement

In the brain, connections are usually asymmetrical, i.e. the connection strength from A to B is different than from B to A. Using physical confinements neuronal outgrowths can be steered (Figure B.3). It can be seen that three different methods were applied. In a) there are large openings at the emitting side, while at the receiving side there are smaller. Therefore, there is an increased chance that the desired directionality is achieved. In b) the entrances are the same side, but the receiving side is more likely to turn left or right and thereby grow back towards its origin. In c) barbed channels only slightly influence the emitting side, but form obstacles when growing from right to left because of the stiffness of the axons.

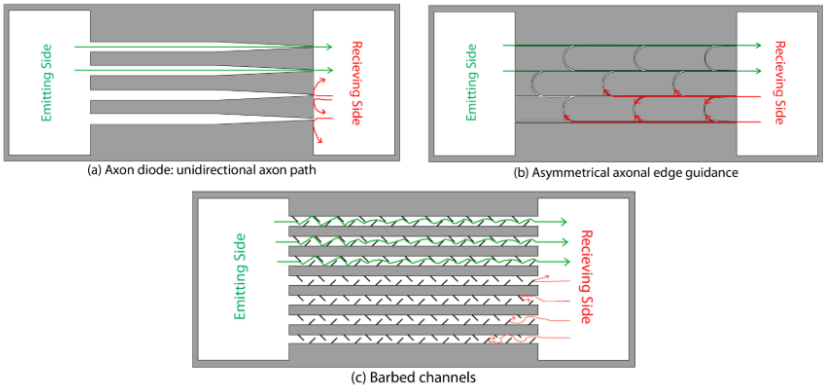

Figure B.3: Axon guidance through physical confinement [46].

B.1.4 Aligned Nanofibers

Using electrospinning, substrates can be made with locally aligned nanofibers (Figure B.4). Cells are sensitive to this alignment as can be seen in Figure B.4b and their outgrowths align well with it in early days of culturing [61]. Unfortunately, this method does not facilitate controlled 3D culturing or single cell analysis.

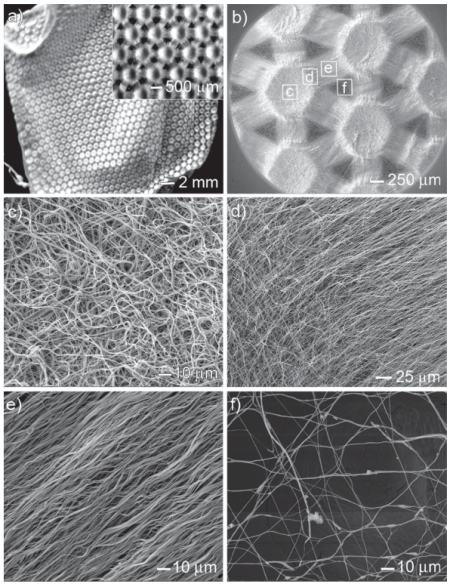

(a) The substrate made of nanofibers without cells seeded onto it.

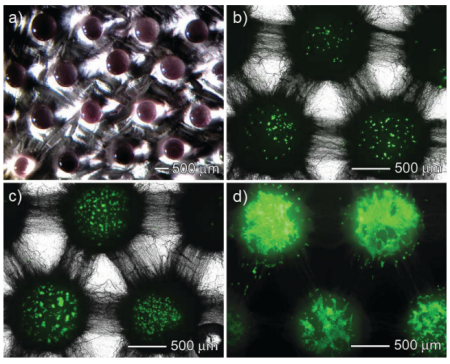

(b) a) seeding of the cells in droplets b) Fluorescence microscopy after one day c) Same as b) with increased cell density d) Three days of incubation of c)

Figure B.4: Guidance of neurite outgrowths using aligned nanofibers [61].

B.1.5 Topochip

The TopoChip is a device for researching cell response to different topographies. The TopoChip consists of a 2x2 cm area on which 4356 so-called TopoUnits are present, 66x66 of these units. These 290x290 µm TopoUnits are separated by 20 µm high and 10 µm wide walls [62].

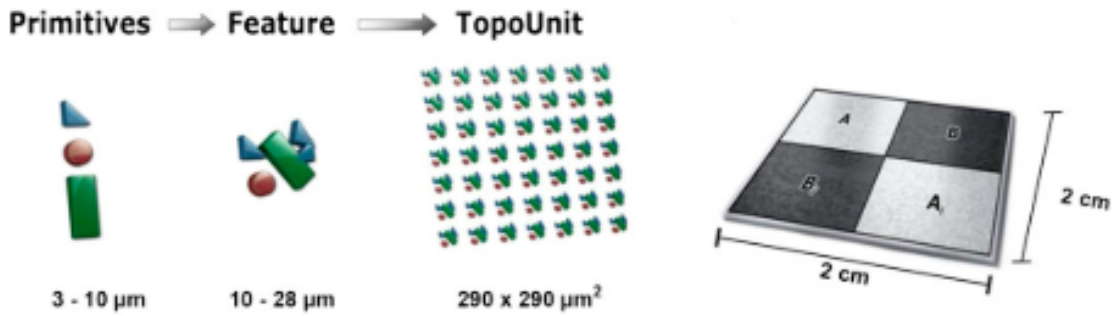

Figure B.5: Overview of the topochip [62].

In the chip 2176 different surface topographies can be researched at once. Each topography is executed twice (in Figure B.5 X and X' are the same), to exclude position effects from influencing the experiment. Then there are also 4 empty TopoUnits as a control test.

The topographies are created using three different types of primitives: triangles, circles and squares. These are combined into features (with a size of 10x10, 20x20 or 28x28 μm) which are executed multiple times within one TopoUnit. Cells are then seeded in a homogeneous way, so that the effects of the topography can be evaluated.

The advantage of this device is that many different topographies can be researched at once. However, it is still difficult to research the exact effects on one cell. First of all, a cell does not always position itself on the same place on the topography, as one TopoUnit is much larger than one cell. Moreover, this also creates a situation in which multiple parameters can change in an experiment: the amount of cells in the TopoUnit, their positions and their positions relative to each other. Also, the cells in one TopoUnit cannot interact with that of another TopoUnit, when the interaction and network formation is of importance.

B.2 Micropatterning the Substrate Surface

In the literature, many different other topographies and methods can be found to pattern substrates in order to influence cell morphology and behaviour. Contrary to the microsieve, these other methods rarely include capturing of single cells. Moreover, in most cases because a surface is patterned, this means that there is only 2D culturing possible, not 3D.

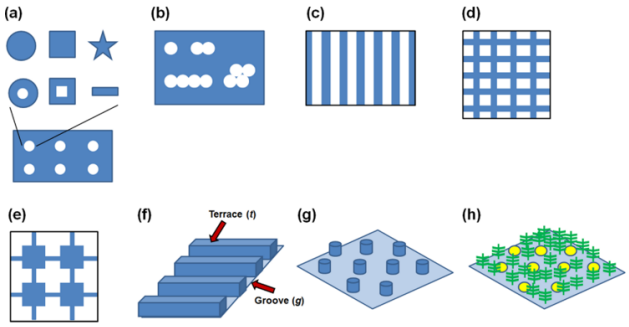

Figure B.6: Overview of micropatterned substrates found in literature for influencing cell morphology and behaviour [30].

B.3 Lab-Scale Manufacturing Process Overview

Here in word, the fabrication process steps as described by Sabahi-Kaviani and Luttge [12].

1. Cleaning the master mold
   (a) Blow clean µSEA using a N_2 gun
2. Creating the PDMS negative replica
   (a) Mix PDMS base and cross-linking agent 10:1
   (b) Degas in vacuum desiccator for 20 min
   (c) Pour 500µm layer onto µSEA
   (d) Cure on a 95 °C for 10 minutes
   (e) Peel of the master mold
   (f) Cut into 2x2 cm2 square
3. Plasma treatment of the PDMS negative replica
   (a) Plasma oxidation at 10 W for 30 s with plasma asher, to make surface hydrophilic
4. Spin coating the NOA81 positive replica
   (a) 500 rpm for 30 s with an acceleration of 200 rpm/s
   (b) Speed for final thickness for 30 s with an acceleration of 300 rpm/s
   (c) Deceleration of 300 rpm/s until stop
5. Cure the NOA81 positive replica
   (a) Place mold in UV-LED exposure system with intensity of 15mW/cm2
6. Peeling of the NOA81 positive replica
   (a) Feel of NOA81 positive directly after exposure
   (b) Place on flat surface cured again at the same settings
   (c) Measure thickness using a profilometer
7. Mounting the NOA81 positive replica on PMMA ring
   (a) Apply small amount of NOA81 to PMMA ring
   (b) Assemble and cured using previous exposure settings
8. Through-hole laser ablation
   (a) Ablate laser hole using KrF-laser for 1500 pulses at 150 Hz.

B.4 Manufacturing Process Time Estimates

Here, a schematic overview of the manufacturing steps given in word above is given, see Table B.1. Also, an estimate of the time each manufacturing step is given.

Table B.1: Rough indication of the time required for execution of each manufacturing step.

Manufacturing Step	Sub-Step	Time (min)
1. Silicon μSEA Master	1.1 Start with Silicon μSEA Master	0
	1.2 Blown-clean using N2 gun	2
2. PDMS Negative Replica	2.1 Mix PDMS-Base and cross-linking agent 10:1	5
	2.2 Degas in vacuum desiccator	20
	2.3 Pour onto the μSEA master	2
	2.4 Cure on hotplate	15
	2.5 Peel of the master mold	5
	2.6 Cut into 2x2 cm2 square	5
3. Plasma treatment PDMS	3.1 Oxidation at 10 W	2
4. Spin coating NOA81	4.1 Pour NOA81 in excess	2
	4.2 i. 500R 30s 200R/s	2
	4.3 ii. 30s 300R/s	
	4.4 iii. 300R/s till stop	
5. Curing the NOA81	5.1 Place mold in UV-led exposure system	1
	5.2 Expose at 15mW/cm2 dos of 2100 mJ/cm2	2
6. Peeling of the NOA81	6.1 Peel of NOA81 after exposure	5
	6.2 Cure at same settings	2.3
7. Mounting to PMMA ring	7.1 Apply small amount of NOA81 with sharp tip	7.5
	7.2 Assemble and cure again	
8. Laser ablation	8.1 Place the sieve in the setup	1
	8.2 Laser Ablation	15 sec/hole
	Lead time without ablation (min)	78.8

A rough estimate of the raw process time of one microsieve is 78.8 minutes. This does not take laser ablation into account, which for 912 holes would add 3.8 hours to the total time. Moreover, are some other important things to note:

- This is a rough estimate.
- This does not take into account executing multiple steps in parallel.
- This does not take into account batch processing in, for example the pouring, curing and exposure steps.
- This considers only one workline.
- Some products can be used more than once e.g. extra PDMS can be made for more than one sieve and the PDMS negative can be used about three times.

B.5 Production Units

In total, there are 20 steps in the manufacturing process as can be seen in Figure B.7. These manufacturing process steps can be subdivided into different Production Units (PUs), indicated by color coding in Figure B.7. This is useful when implementing parallel and batch processing and improving the lead time overall. PUs consist of process steps that are linked together in the production process and can or should not be done separately.

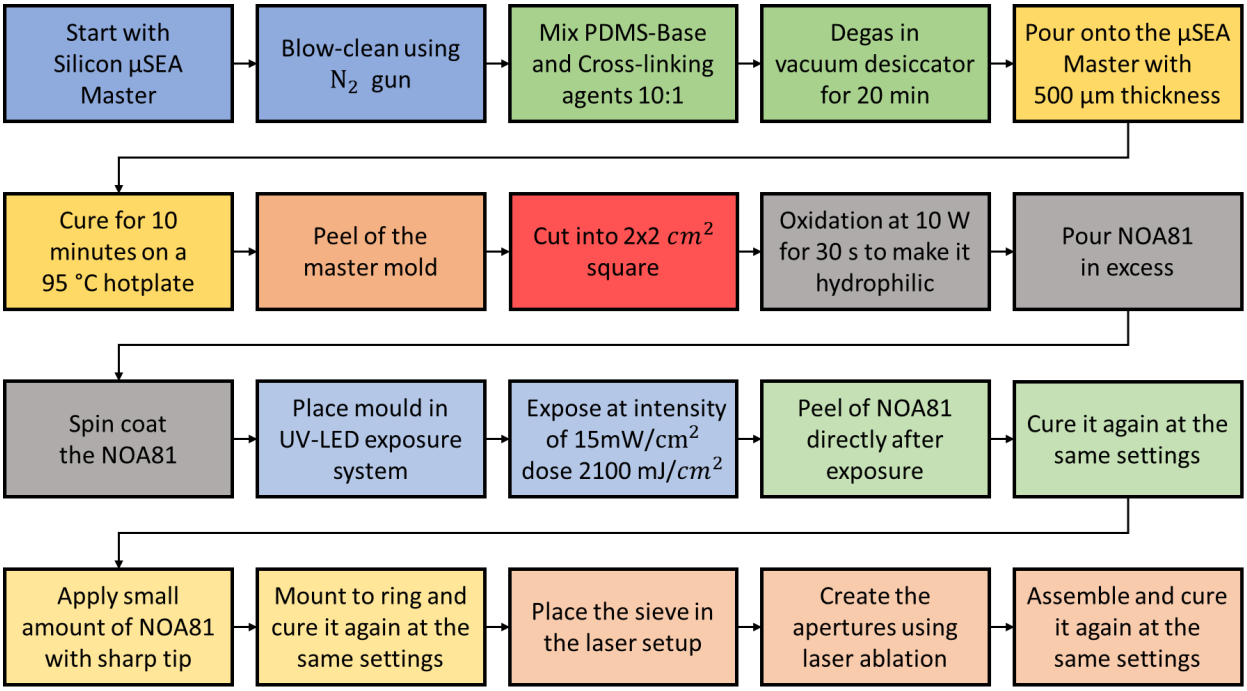

Figure B.7: Overview of fabrication steps

In Figure B.8, the manufacturing process can be seen condensed into the eight PUs.

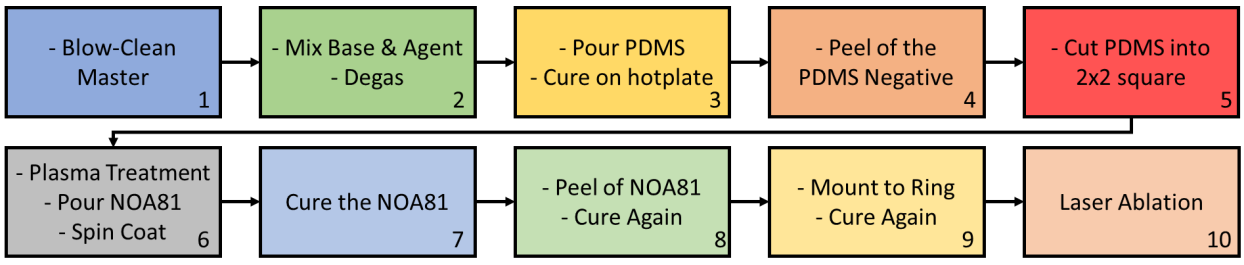

Figure B.8: Overview of production units

Because the steps within one PU have to be executed after one another, when trying to improve the lead time, each PU has to be considered as a whole rather than in their individual steps. Hence in Table B.2, the time is given for each PU as a whole.

Table B.2

PU	Manufacturing Steps	Estimated Time (min)
1	Blow-clean master	2
2	Mix Base and agent	25
	Degas	
3	Pour PDMS on master	17
	Cure on hotplate	
4	Peel PDMS negative from master mould	5
5	Cut PDMS into 2x2 square	5
6	Plasma treatment	6
	Pour NOA81	
	Spin coat NOA81	
7	Curing the NOA81	3
8	Peeling of the NOA81	7.3
	Cure the NOA81 again	
9	Mount to PMMA ring	7.50
	Cure again	
10	Laser ablation	Dependent on amount
Total (min)		78.8

In total there are 20 manufacturing steps, of which 4 little steps as placing a half-product in the laser setup are not taken into account. The 16 remaining steps have been divided into 10 PUs, based on which steps have to be done together. PUs:

1. The blowing clean of the master is completely separate of the other steps (if it should be included as a step at all).
2. The PDMS preparation is probably best done in one continuous step, as it requires similar equipment and it seems inefficient to mix the PDMS without placing it in vacuum desiccator straight thereafter.
3. The pouring of the PDMS together with the curing forms the preparation of the PDMS negative. This has to be done together in one step.
4. The peeling can be seen as a different PU. The master mould becomes available again when this is completed.
5. The cutting of the PDMS is completely separate of the other steps. Although in practice it will probably often be done after the previous step.
6. The plasma treatment is only effective for a limited time span. Therefore, it has to be in one PU together with the pouring and spin coating.
7. A separate step is the curing of the NOA81
8. Peeling and curing again have to be combined, otherwise the NOA81 might lose its proper shape.
9. Mounting and curing has to be combined to successfully attach the NOA81 to the PMMA ring.
10. The last laser ablation step is completely separate again.

C Appendix C

C.1 Material Properties in Literature

C.1.1 Membrane

Table C.1: Material properties of the cell membrane in the literature.

Young's modulus [Pa]	Poisson's ratio [-]	Thickness [nm]	ρ [kg/m^3]	Source
1000 - 8000	0.30	100 - 500	-	[74]
1000	0.30	6	-	[75]
-	0.30	-	-	[63]
3500	0.49	-	1025	[64]
1000	0.30	6	-	[77]

C.1.2 Cytoplasm

Table C.2: Material properties of the cytoplasm in the literature.

Young's modulus [Pa]	Poisson's ratio [-]	ρ [kg/m^3]	Source
100	0.37	-	[74]
100	0.37	-	[75]
-	0.37	-	[63]
3500	0.49	1025	[64]
100	0.37	-	[77]

C.1.3 Nucleus

Table C.3: Material properties of the nucleus in the literature

Young's modulus [Pa]	Poisson's ratio [-]	ρ [kg/m^3]	Source
400	0.37	-	[74]
400	0.37	-	[75]
-	0.37	-	[63]
5000	0.49	1250	[64]
400	0.37	-	[77]

C.1.4 Microtubules

Table C.4: Material properties of the microtubules in the literature

Young's modulus [Pa]	Poisson's ratio [-]	Area [nm^2	ρ [kg/m^3]	Source
1.2 $\times 10^9$	0.30	190	-	[74]
1.2 $\times 10^9$	0.30	190	-	[75]
1.2 $\times 10^9$	0.30	113	-	[63]
1.2 $\times 10^9$	0.30	-	1000	[64]
1.2 $\times 10^9$	-	200	-	[77]

C.1.5 Actin Filaments

Table C.5: Material properties of the actin in the literature

Young's modulus [Pa]	Poisson's ratio [-]	Area [nm^2	ρ [kg/m^3]	Source
2.6 $\times 10^9$	0.30	19 nm2	-	[74]
2.6 $\times 10^9$	0.30	18 nm2	-	[75]
3.4 $\times 10^5$	0.30	250 nm	-	[63]
3.4 $\times 10^5$	0.30	-	1000	[64]
1.0 $\times 10^9$	-	20 nm2	-	[77]

C.1.6 Intermediate Filaments

Table C.6: Material properties of the intermediate filaments in the literature

Young's modulus [Pa]	Poisson's ratio [-]	Area [nm^2]	Source
2 $\times 10^9$	0.30	100	[74]
-	-	-	[75]
7.6 $\times 10^6$	0.30	79	[63]
-	-	-	[64]
-	-	-	[77]

C.1.7 Nuclear Lamina

Table C.7: Material properties of the lamina in the literature

Young's modulus [Pa]	Poisson's ratio [-]	Area [nm^2]	Source
-	-	-	[74]
-	-	-	[75]
1.4 $\times 10^6$	0.30	79	[63]
-	-	-	[64]
-	-	-	[77]

C.1.8 Chromatin

Table C.8: Material properties of the chromatin in the literature

Young's modulus [Pa]	Poisson's ratio [-]	Area [nm^2]	Source
-	-	-	[74]
-	-	-	[75]
2.44 $\times 10^6$	0.30	1.13	[63]
-	-	-	[64]
-	-	-	[77]

D Appendix D

D.1 Micropore Without Ablation

D.1.1 Unablated Configuration

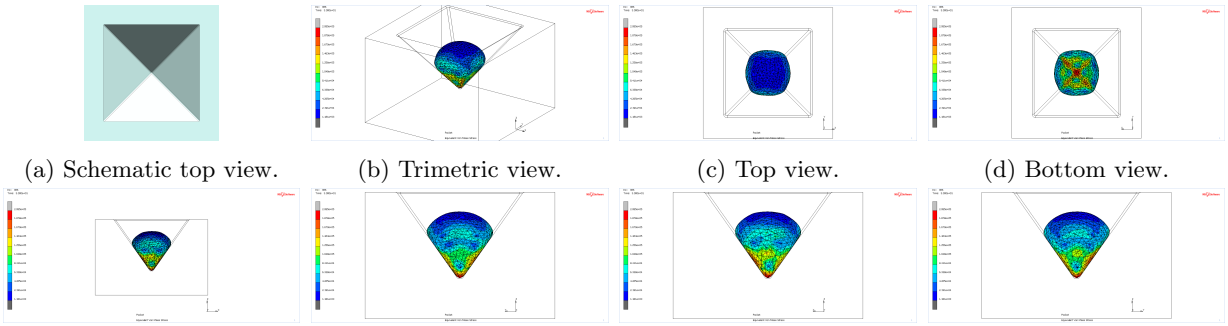

(a) Schematic top view. (b) Trimetric view. (c) Top view. (d) Bottom view.

(e) Front view. (f) Left view. (g) Back view. (h) Right view.

Figure D.1: Simulation results of an unablated micropore.

D.2 Micropores with One Ablation

D.2.1 Configuration FM

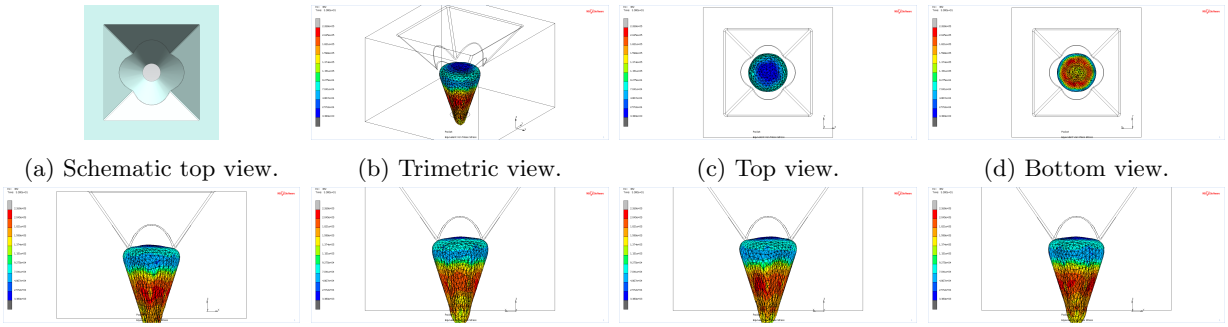

(a) Schematic top view. (b) Trimetric view. (c) Top view. (d) Bottom view.

(e) Front view. (f) Left view. (g) Back view. (h) Right view.

Figure D.2: Simulation results of configuration FM, a micropore ablated in the middle from the front.

D.2.2 Configuration FE

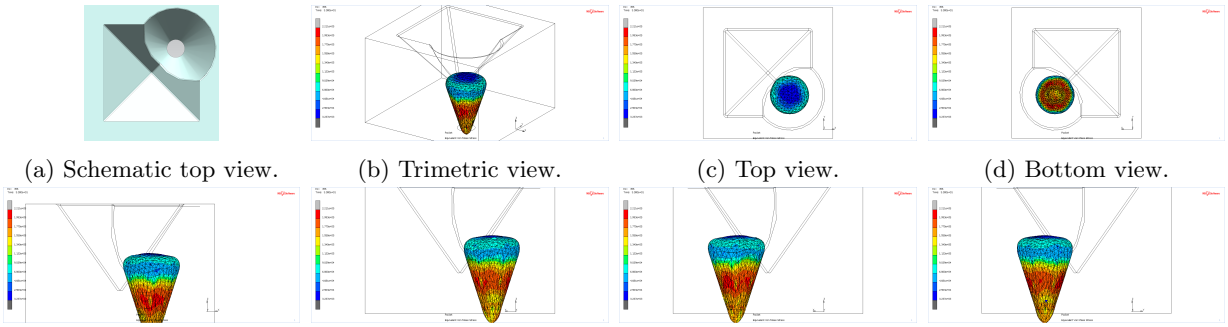

(a) Schematic top view. (b) Trimetric view. (c) Top view. (d) Bottom view.

(e) Front view. (f) Left view. (g) Back view. (h) Right view.

Figure D.3: Simulation results of configuration FE, a micropore ablated on the edge from the front.

D.2.3 Configuration FS

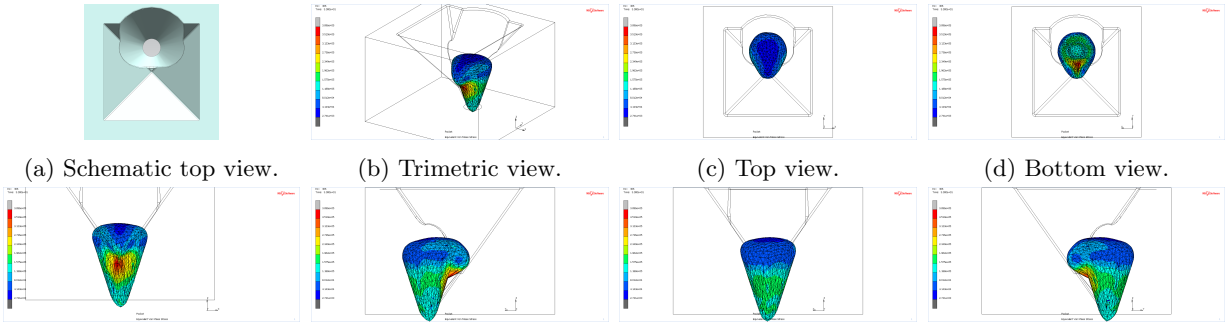

(a) Schematic top view. (b) Trimetric view. (c) Top view. (d) Bottom view.

(e) Front view. (f) Left view. (g) Back view. (h) Right view.

Figure D.4: Simulation results of configuration FS, a micropore ablated on the slope from the front.

D.2.4 Configuration RM

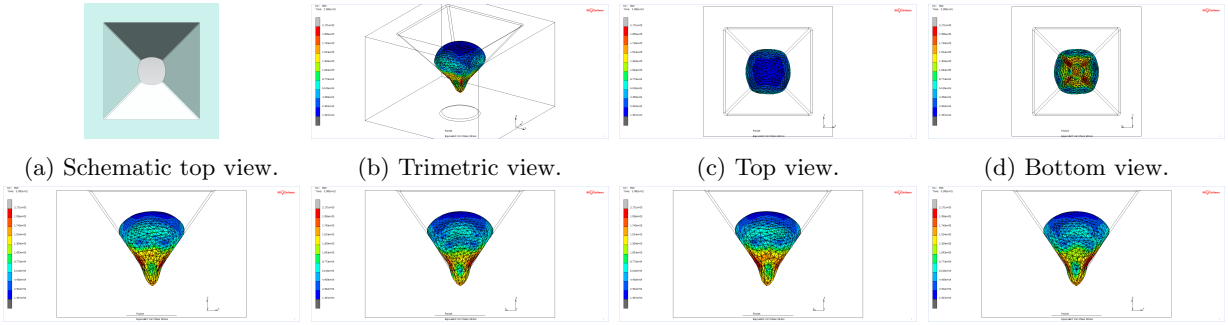

(a) Schematic top view. (b) Trimetric view. (c) Top view. (d) Bottom view.

(e) Front view. (f) Left view. (g) Back view. (h) Right view.

Figure D.5: Simulation results of configuration RM, a micropore ablated in the middle from the rear.

D.2.5 Configuration RE

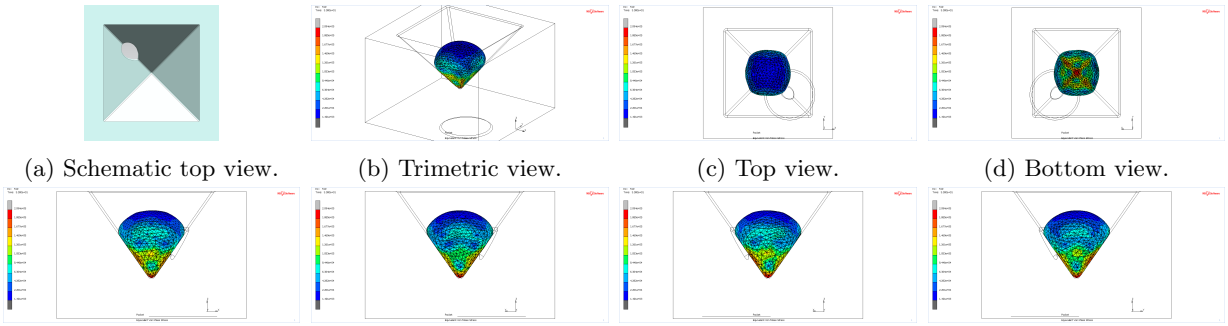

(a) Schematic top view. (b) Trimetric view. (c) Top view. (d) Bottom view.

(e) Front view. (f) Left view. (g) Back view. (h) Right view.

Figure D.6: Simulation results of configuration RE, a micropore ablated on the edge from the rear.

D.2.6 Configuration RS

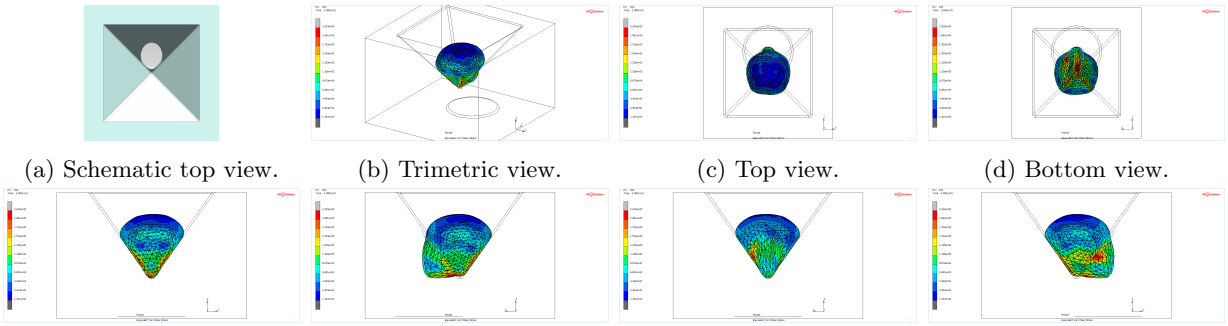

(a) Schematic top view. (b) Trimetric view. (c) Top view. (d) Bottom view.

(e) Front view. (f) Left view. (g) Back view. (h) Right view.

Figure D.7: Simulation results of configuration RS, a micropore ablated on the slope from the rear.

D.3 Micropores with Two Ablations

D.3.1 Configuration F2_1

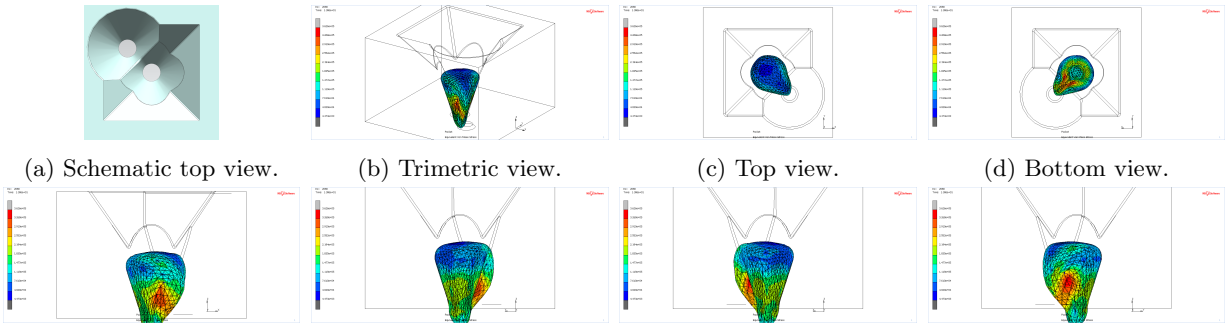

(a) Schematic top view. (b) Trimetric view. (c) Top view. (d) Bottom view.

(e) Front view. (f) Left view. (g) Back view. (h) Right view.

Figure D.8: Simulation results of configuration F2_1, a micropore ablated in the middle and on the edge from the front.

D.3.2 Configuration F2_2

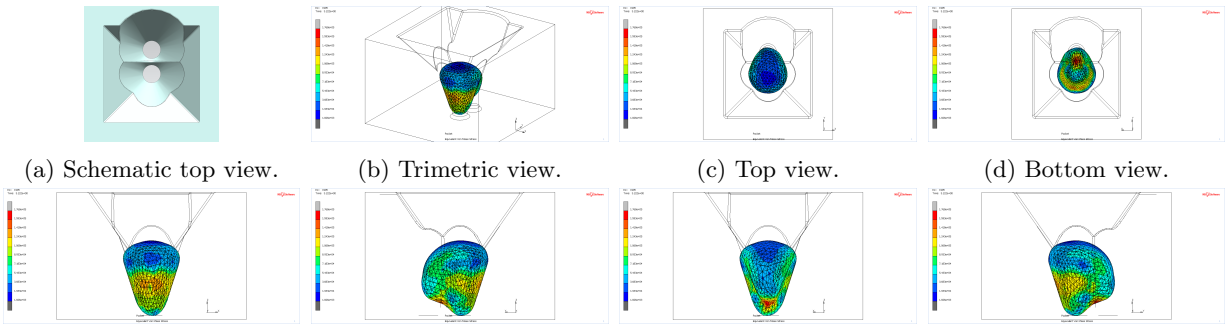

(a) Schematic top view. (b) Trimetric view. (c) Top view. (d) Bottom view.

(e) Front view. (f) Left view. (g) Back view. (h) Right view.

Figure D.9: Simulation results of configuration F2_2, a micropore ablated in the middle and on the slope from the front.

D.3.3 Configuration F2_3

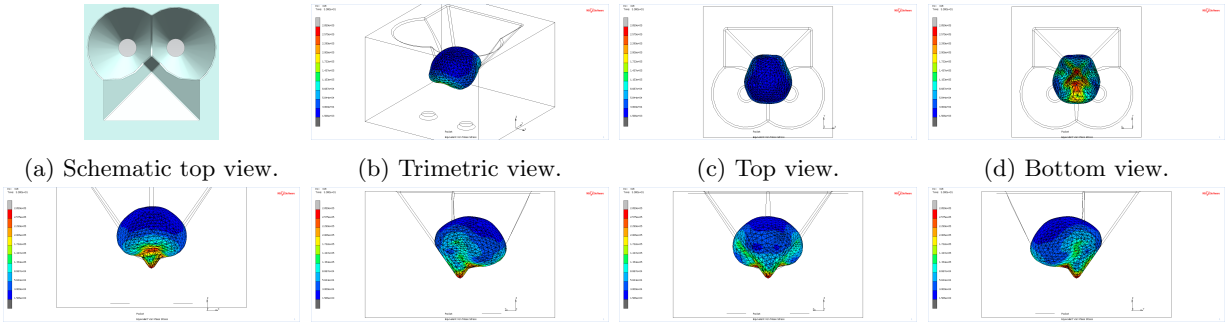

(a) Schematic top view. (b) Trimetric view. (c) Top view. (d) Bottom view.

(e) Front view. (f) Left view. (g) Back view. (h) Right view.

Figure D.10: Simulation results of configuration F2_3, a micropore ablated on two edges from the front.

D.3.4 Configuration F2_4

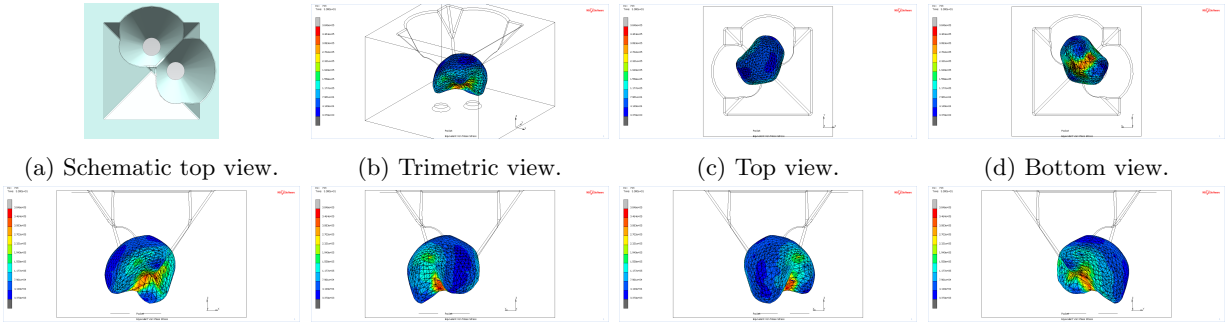

(a) Schematic top view. (b) Trimetric view. (c) Top view. (d) Bottom view.

(e) Front view. (f) Left view. (g) Back view. (h) Right view.

Figure D.11: Simulation results of configuration $F2_4$, a micropore ablated on two slopes from the front.

D.3.5 Configuration R2_1

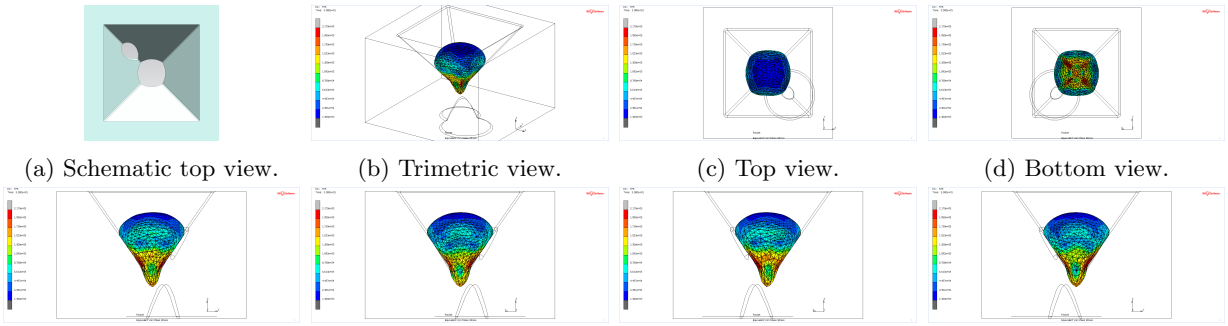

(a) Schematic top view. (b) Trimetric view. (c) Top view. (d) Bottom view.

(e) Front view. (f) Left view. (g) Back view. (h) Right view.

Figure D.12: Simulation results of configuration $R2_1$, a micropore ablated in the middle and on the edge from the rear.

D.3.6 Configuration R2_2

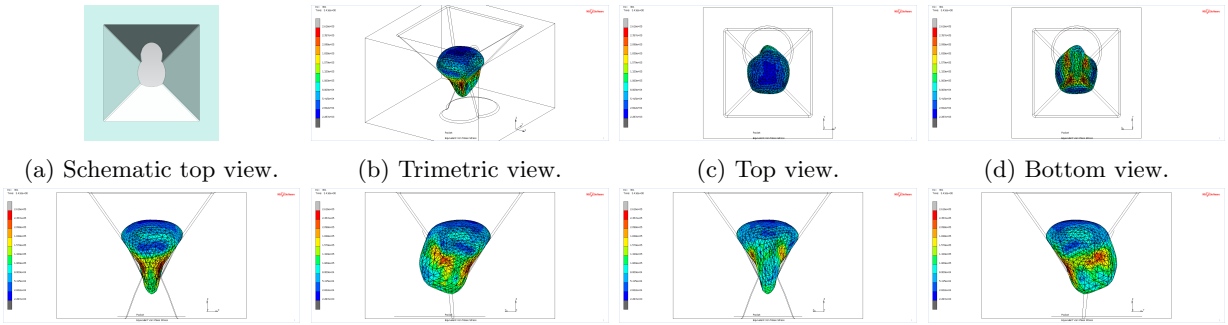

(a) Schematic top view. (b) Trimetric view. (c) Top view. (d) Bottom view.

(e) Front view. (f) Left view. (g) Back view. (h) Right view.

Figure D.13: Simulation results of configuration R2_2, a micropore ablated in the middle and on the slope from the rear.

D.3.7 Configuration R2_3

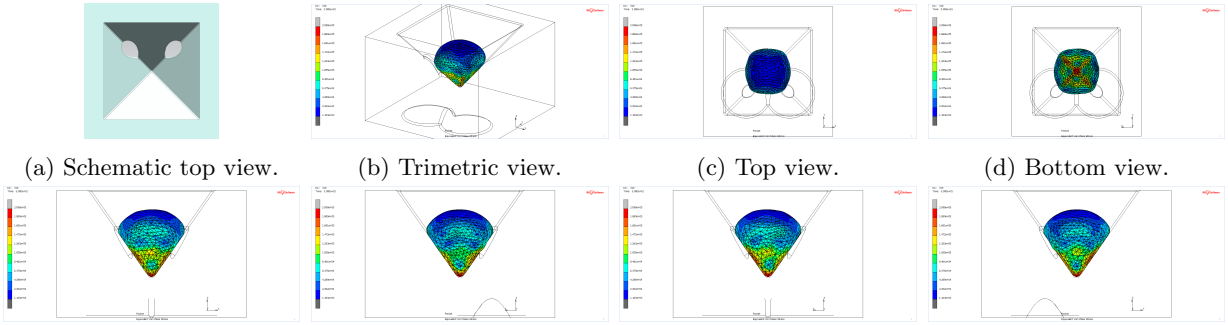

(a) Schematic top view. (b) Trimetric view. (c) Top view. (d) Bottom view.

(e) Front view. (f) Left view. (g) Back view. (h) Right view.

Figure D.14: Simulation results of configuration R2_3, a micropore ablated on two edges from the rear.

D.3.8 Configuration R2_4

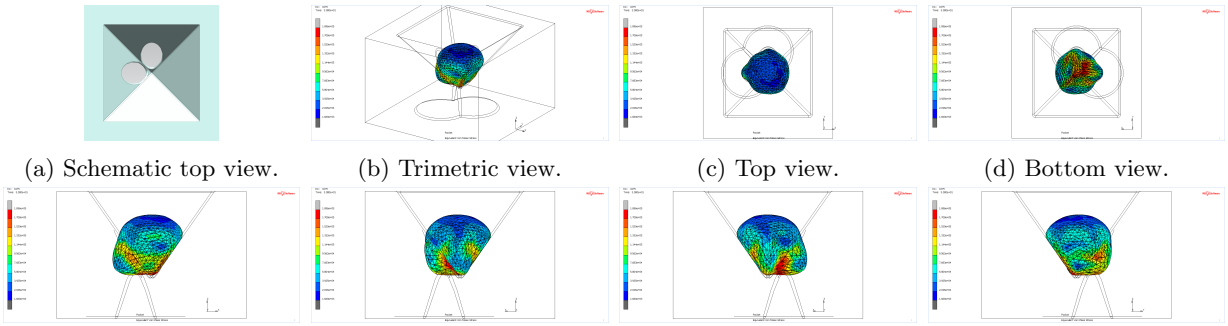

(a) Schematic top view. (b) Trimetric view. (c) Top view. (d) Bottom view.

(e) Front view. (f) Left view. (g) Back view. (h) Right view.

Figure D.15: Simulation results of configuration R2_4, a micropore ablated on two slopes from the rear.

D.4 Micropores with Three Ablations

D.4.1 Configuration F3_1

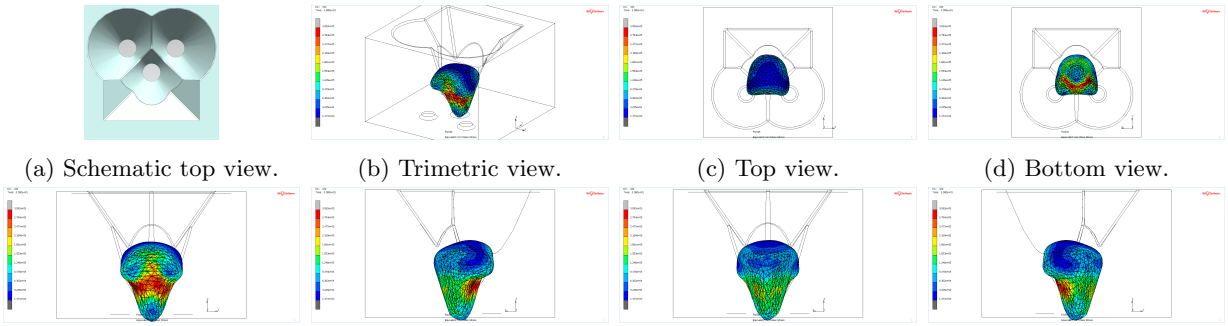

(a) Schematic top view. (b) Trimetric view. (c) Top view. (d) Bottom view.

(e) Front view. (f) Left view. (g) Back view. (h) Right view.

Figure D.16: Simulation results of configuration F3_1, a micropore ablated in the middle and two edges from the front.

D.4.2 Configuration F3_2

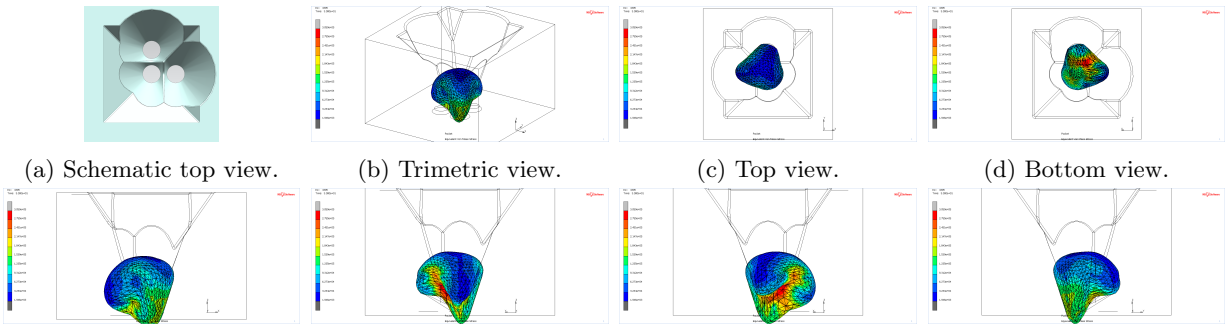

(a) Schematic top view. (b) Trimetric view. (c) Top view. (d) Bottom view.

(e) Front view. (f) Left view. (g) Back view. (h) Right view.

Figure D.17: Simulation results of configuration F3_2, a micropore ablated in the middle and on two slopes from the front.

D.4.3 Configuration F3_3

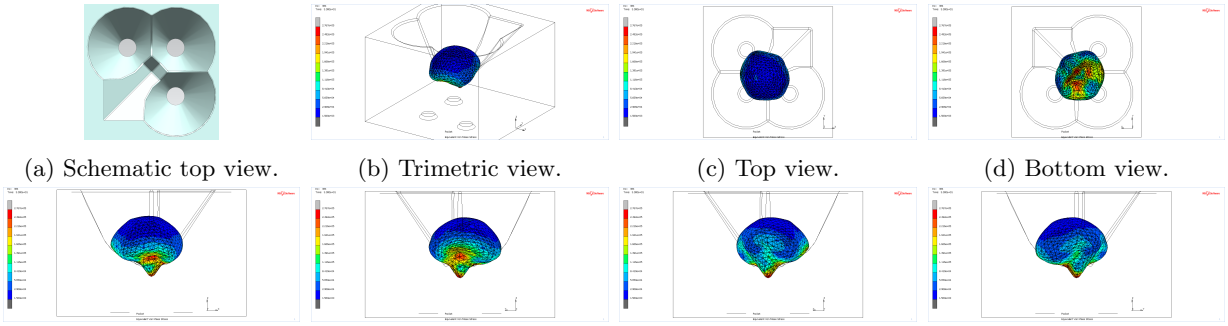

(a) Schematic top view. (b) Trimetric view. (c) Top view. (d) Bottom view.

(e) Front view. (f) Left view. (g) Back view. (h) Right view.

Figure D.18: Simulation results of configuration F3_3, a micropore ablated on three edges from the front.

D.4.4 Configuration F3_4

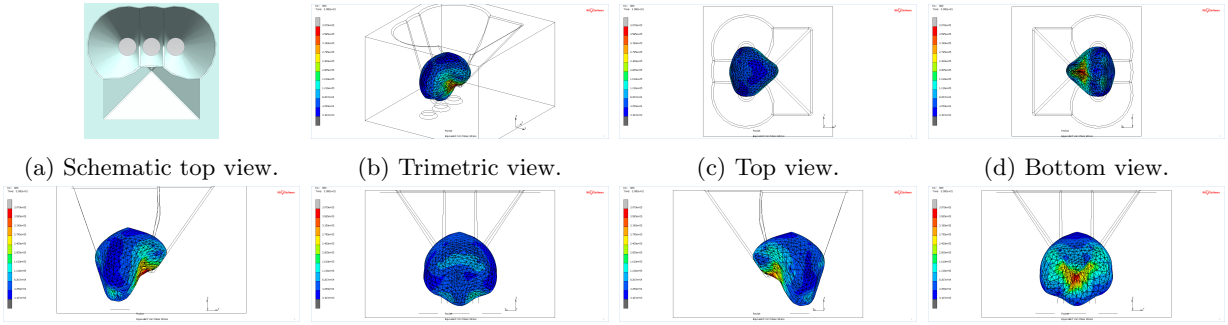

(a) Schematic top view. (b) Trimetric view. (c) Top view. (d) Bottom view.

(e) Front view. (f) Left view. (g) Back view. (h) Right view.

Figure D.19: Simulation results of configuration F3_4, a micropore ablated on one slope and two edges from the front.

D.4.5 Configuration F3_5

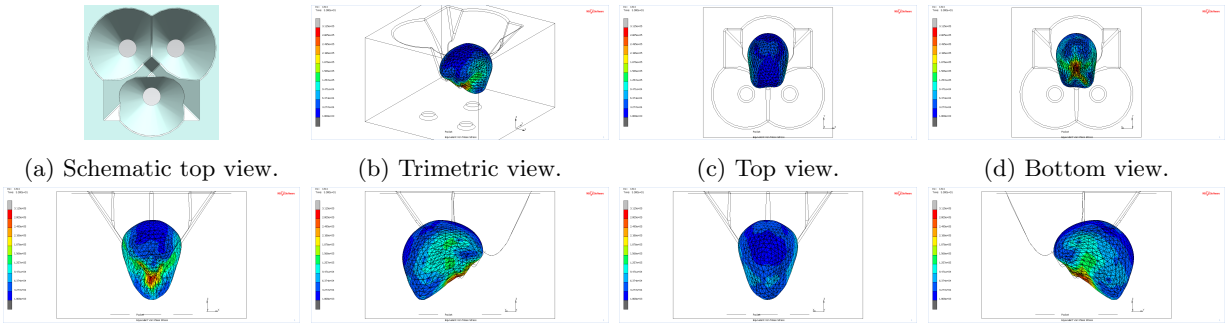

(a) Schematic top view. (b) Trimetric view. (c) Top view. (d) Bottom view.

(e) Front view. (f) Left view. (g) Back view. (h) Right view.

Figure D.20: Simulation results of configuration F3_5, a micropore ablated on one slope and two edges from the front.

D.4.6 Configuration F3_6

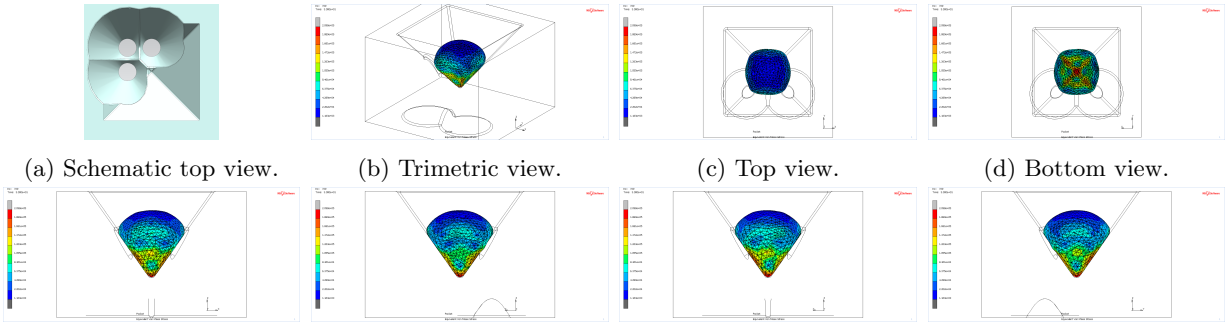

(a) Schematic top view. (b) Trimetric view. (c) Top view. (d) Bottom view.

(e) Front view. (f) Left view. (g) Back view. (h) Right view.

Figure D.21: Simulation results of configuration F3_6, a micropore ablated on one edge and two slopes from the front

D.4.7 Configuration F3_7

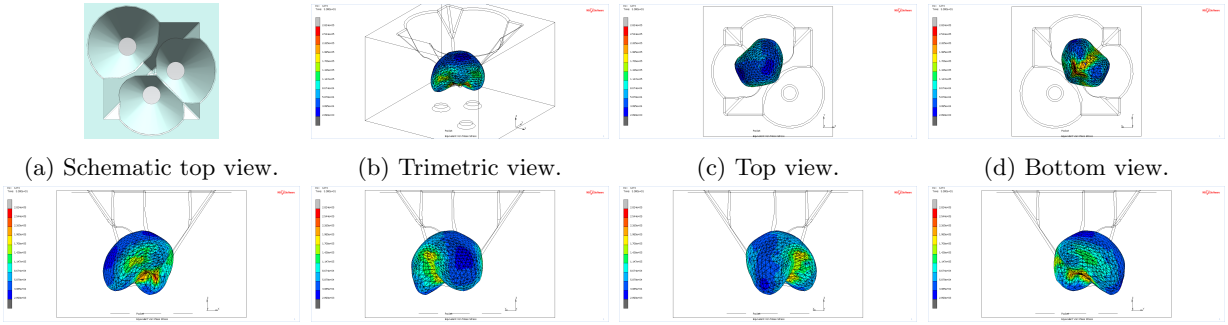

(a) Schematic top view. (b) Trimetric view. (c) Top view. (d) Bottom view.

(e) Front view. (f) Left view. (g) Back view. (h) Right view.

Figure D.22: Simulation results of configuration F3_7, a micropore ablated on one edge and two slopes from the front.

D.4.8 Configuration F3_8

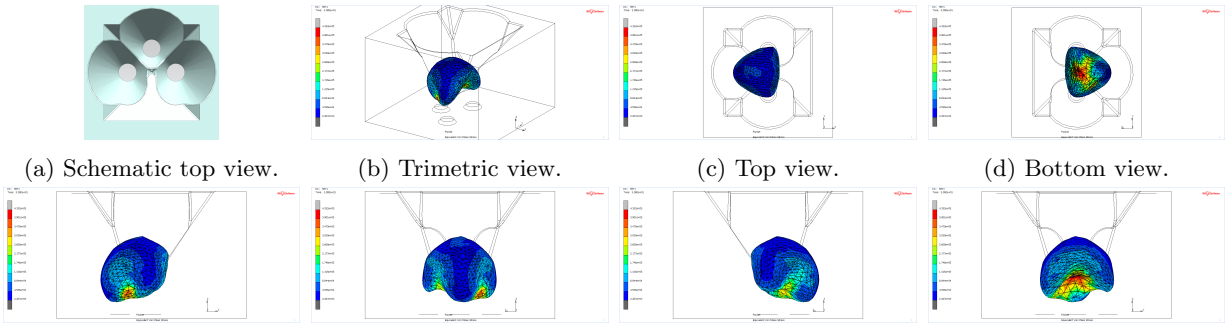

(a) Schematic top view. (b) Trimetric view. (c) Top view. (d) Bottom view.

(e) Front view. (f) Left view. (g) Back view. (h) Right view.

Figure D.23: Simulation results of configuration F3_8, a micropore ablated on three slopes from the front.

D.4.9 Configuration R3_1

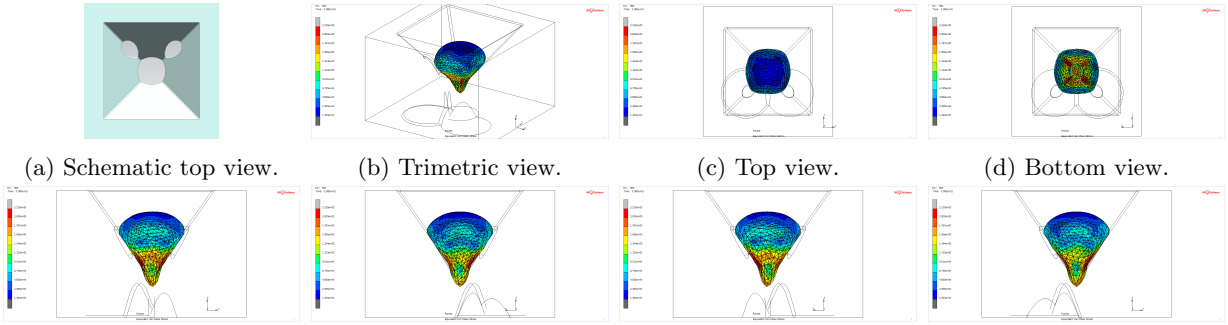

(a) Schematic top view. (b) Trimetric view. (c) Top view. (d) Bottom view.

(e) Front view. (f) Left view. (g) Back view. (h) Right view.

Figure D.24: Simulation results of configuration R3_1, a micropore ablated in the middle and on two edges from the rear.

D.4.10 Configuration R3_2

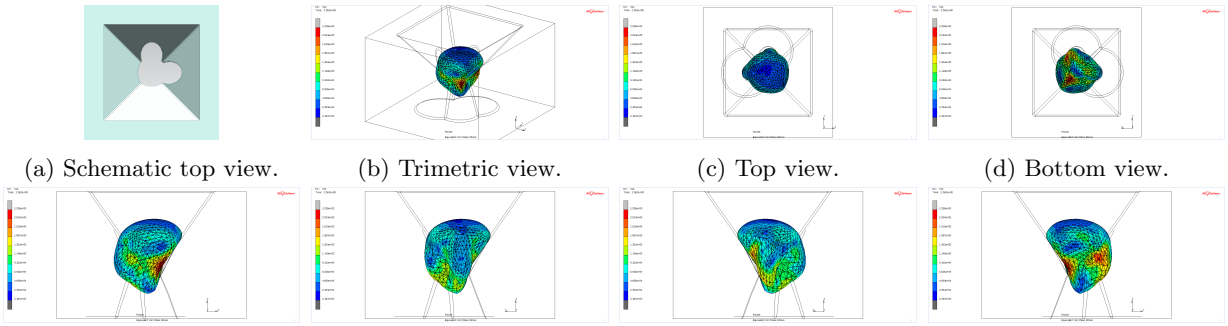

(a) Schematic top view. (b) Trimetric view. (c) Top view. (d) Bottom view.

(e) Front view. (f) Left view. (g) Back view. (h) Right view.

Figure D.25: Simulation results of configuration R3_2 a micropore ablated in the middle and on two slopes from the rear.

D.4.11 Configuration R3_3

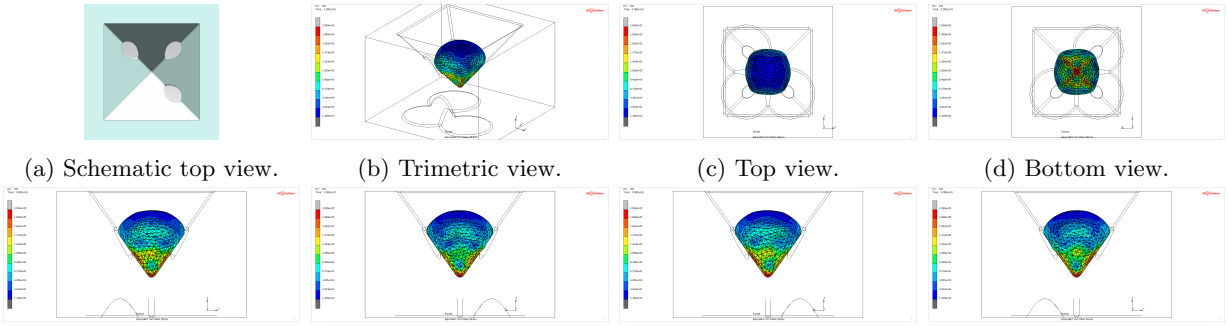

(a) Schematic top view. (b) Trimetric view. (c) Top view. (d) Bottom view.

(e) Front view. (f) Left view. (g) Back view. (h) Right view.

Figure D.26: Simulation results of configuration R3_3, , a micropore ablated on three edges from the rear.

D.4.12 Configuration R3_4

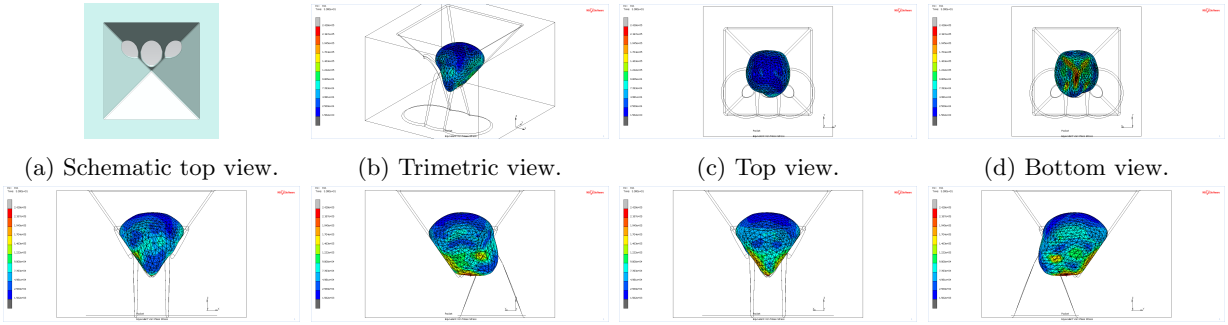

(a) Schematic top view. (b) Trimetric view. (c) Top view. (d) Bottom view.

(e) Front view. (f) Left view. (g) Back view. (h) Right view.

Figure D.27: Simulation results of configuration R3_4, a micropore ablated on one slope and two edges from the rear.

D.4.13 Configuration R3_5

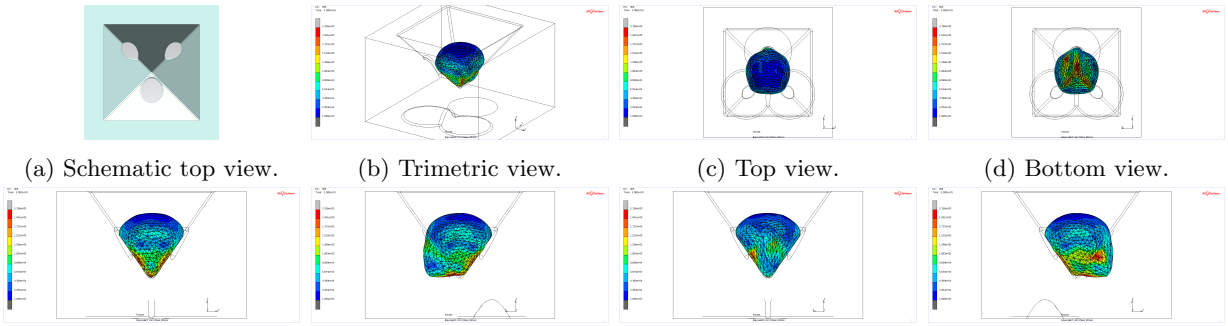

(a) Schematic top view. (b) Trimetric view. (c) Top view. (d) Bottom view.

(e) Front view. (f) Left view. (g) Back view. (h) Right view.

Figure D.28: Simulation results of configuration R3_5, a micropore ablated on one slope and two edges from the rear.

D.4.14 Configuration R3_6

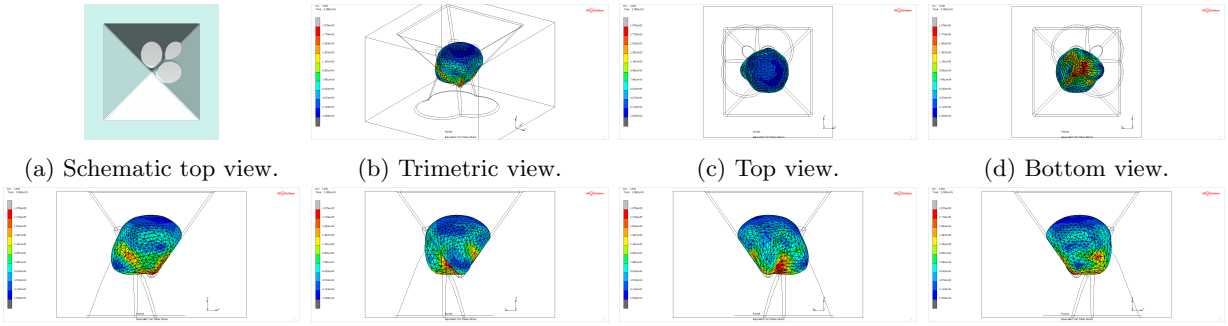

(a) Schematic top view. (b) Trimetric view. (c) Top view. (d) Bottom view.

(e) Front view. (f) Left view. (g) Back view. (h) Right view.

Figure D.29: Simulation results of configuration R3_6 a micropore ablated on two slopes and one edge from the rear.

D.4.15 Configuration R3_7

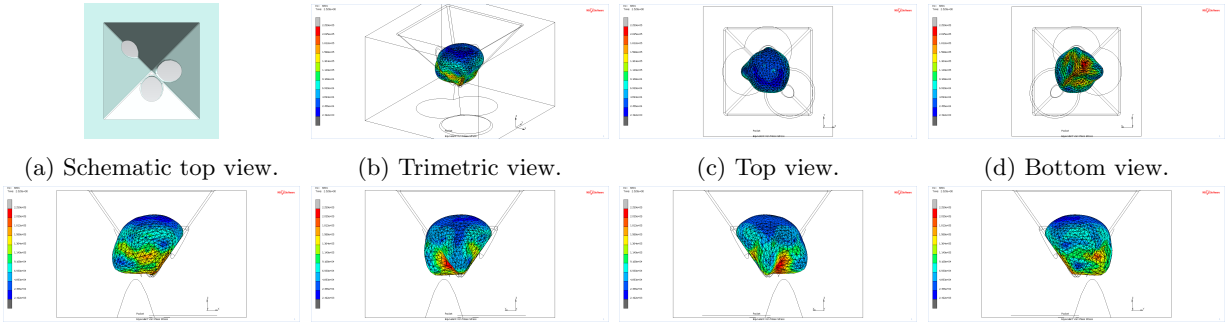

(a) Schematic top view. (b) Trimetric view. (c) Top view. (d) Bottom view.

(e) Front view. (f) Left view. (g) Back view. (h) Right view.

Figure D.30: Simulation results of configuration R3_7, a micropore ablated on two slopes and one edge from the rear.

D.4.16 Configuration R3_8

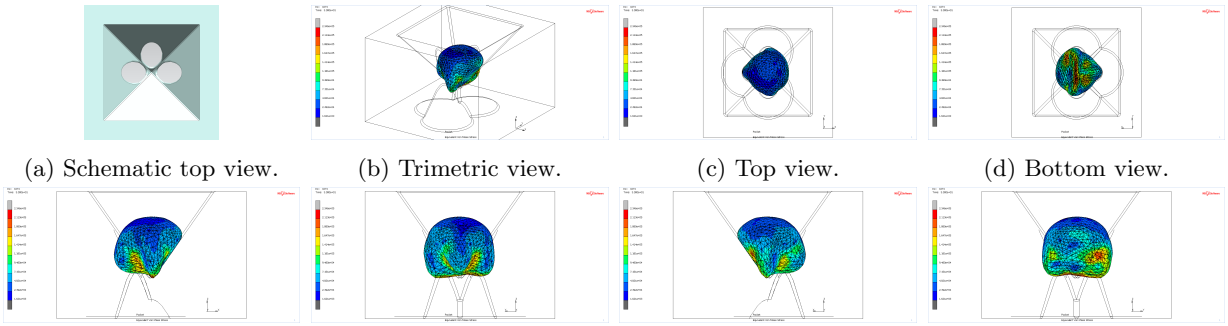

(a) Schematic top view. (b) Trimetric view. (c) Top view. (d) Bottom view.

(e) Front view. (f) Left view. (g) Back view. (h) Right view.

Figure D.31: Simulation results of configuration R3_8, a micropore ablated on three slopes from the rear.

D.5 Micropores with Adjusted Position of the Edge Ablation

D.5.1 Configuration FFE

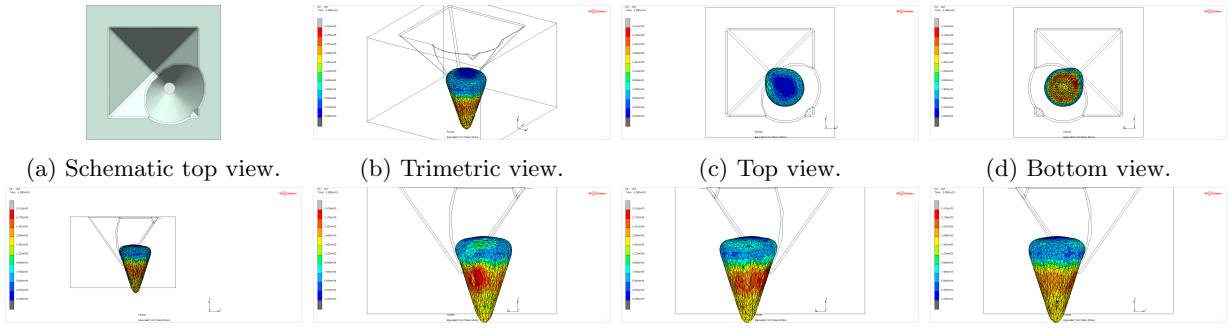

(a) Schematic top view. (b) Trimetric view. (c) Top view. (d) Bottom view.

(e) Front view. (f) Left view. (g) Back view. (h) Right view.

Figure D.32: The renewed simulation results of configuration FFE.

D.5.2 Adjusted Configuration RRE

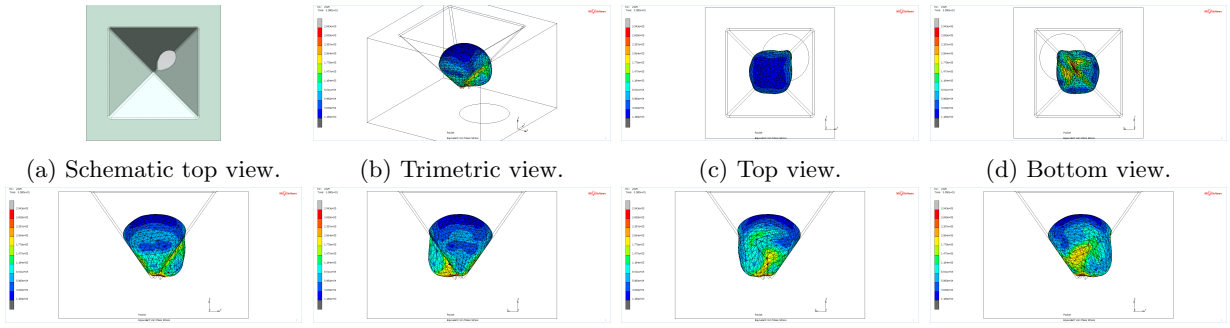

(a) Schematic top view. (b) Trimetric view. (c) Top view. (d) Bottom view.

(e) Front view. (f) Left view. (g) Back view. (h) Right view.

Figure D.33: The renewed simulation results of configuration RRE.

D.5.3 Configuration RR2_1

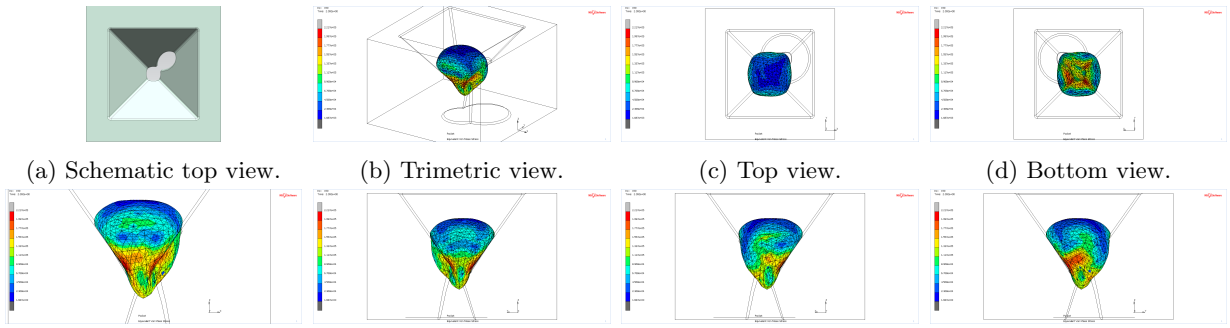

(a) Schematic top view. (b) Trimetric view. (c) Top view. (d) Bottom view.

(e) Front view. (f) Left view. (g) Back view. (h) Right view.

Figure D.34: The renewed simulation results of configuration RR2_1.

D.5.4 Configuration R2_3

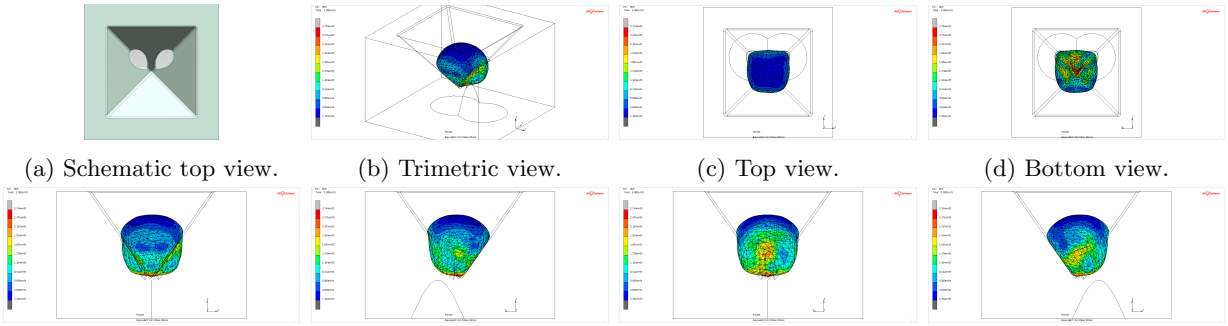

(a) Schematic top view. (b) Trimetric view. (c) Top view. (d) Bottom view.

(e) Front view. (f) Left view. (g) Back view. (h) Right view.

Figure D.35: The renewed simulation results of configuration RR2_3.

D.5.5 Configuration R3_1

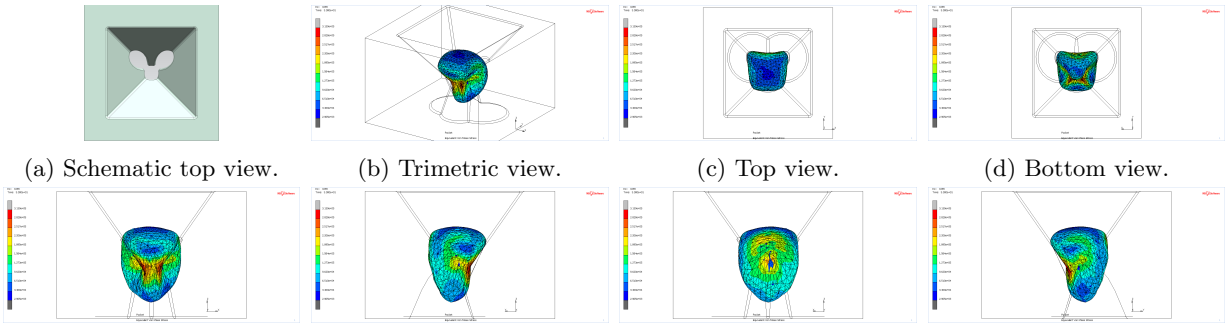

(a) Schematic top view. (b) Trimetric view. (c) Top view. (d) Bottom view.

(e) Front view. (f) Left view. (g) Back view. (h) Right view.

Figure D.36: The renewed simulation results of configuration RR3_1.

D.5.6 Configuration R3_3

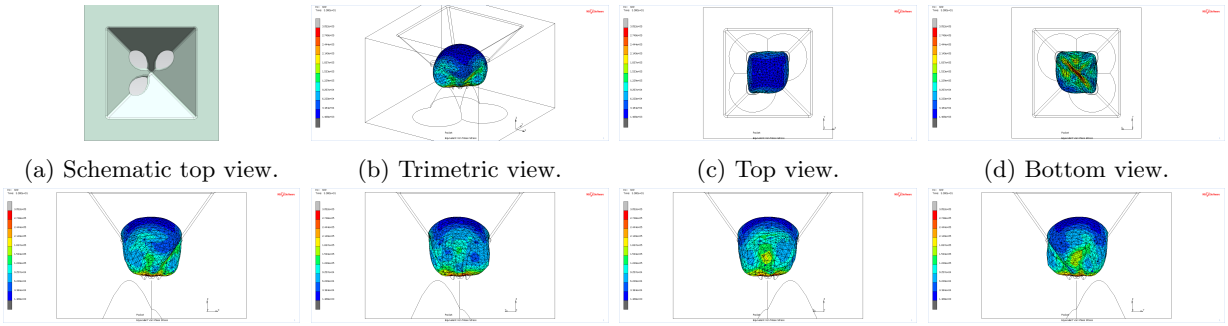

(a) Schematic top view. (b) Trimetric view. (c) Top view. (d) Bottom view.

(e) Front view. (f) Left view. (g) Back view. (h) Right view.

Figure D.37: The renewed simulation results of configuration RR3_3.

D.5.7 Configuration RR3_5

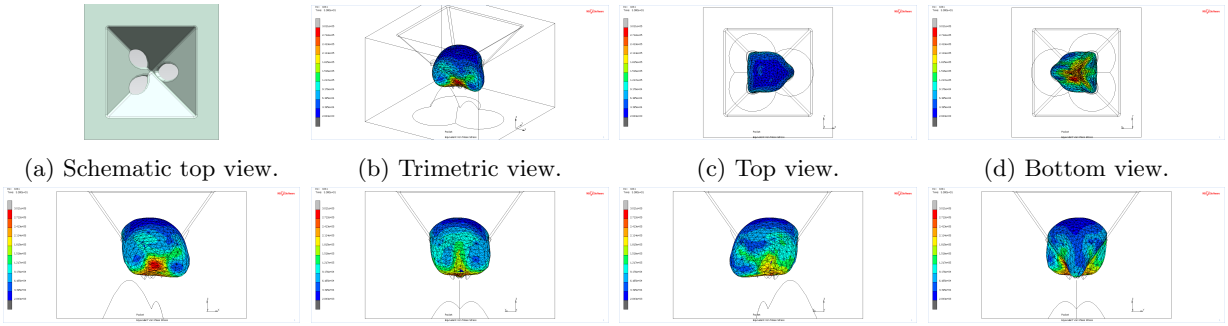

(a) Schematic top view. (b) Trimetric view. (c) Top view. (d) Bottom view.

(e) Front view. (f) Left view. (g) Back view. (h) Right view.

Figure D.38: The renewed simulation results of configuration RR3_5.

D.5.8 Configuration RR3_7

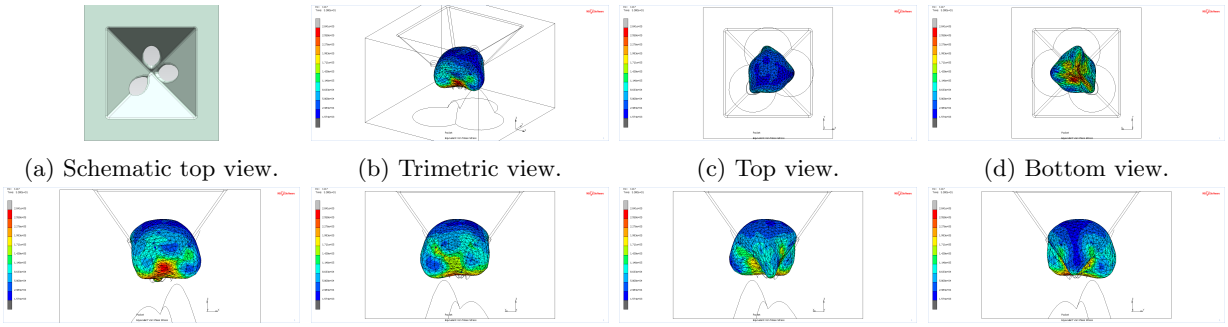

(a) Schematic top view. (b) Trimetric view. (c) Top view. (d) Bottom view.

(e) Front view. (f) Left view. (g) Back view. (h) Right view.

Figure D.39: The renewed simulation results of configuration RR3_7.

D.6 Chessboard-like Topographies

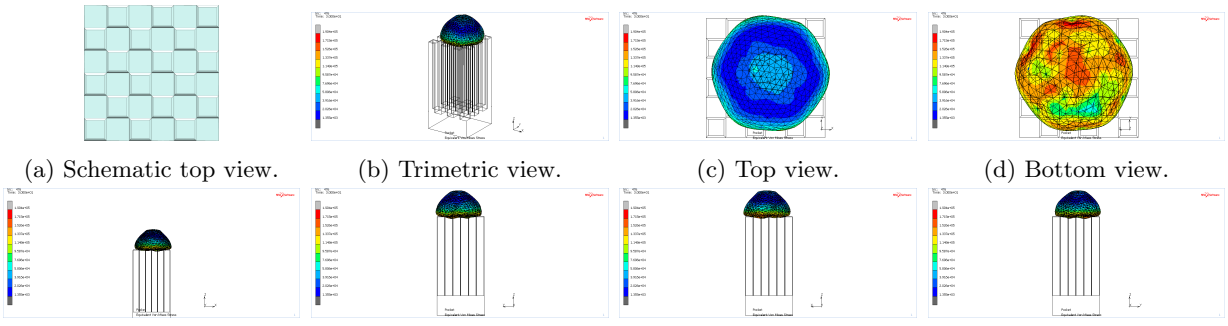

(a) Schematic top view. (b) Trimetric view. (c) Top view. (d) Bottom view.

(e) Front view. (f) Left view. (g) Back view. (h) Right view.

Figure D.40: Simulation results of the model in chessboard-like layout with 2×2 µm squares.

D.6.1 ch4

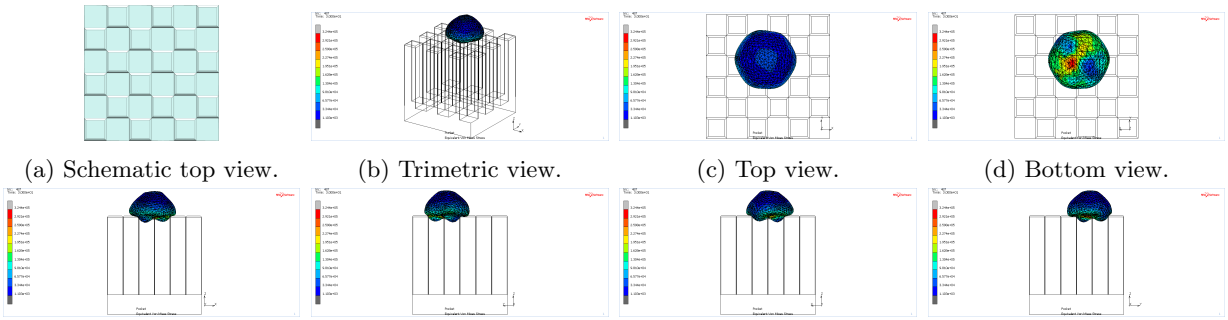

(a) Schematic top view. (b) Trimetric view. (c) Top view. (d) Bottom view.

(e) Front view. (f) Left view. (g) Back view. (h) Right view.

Figure D.41: Simulation results of the model in chessboard-like layout with 4×4 µm squares.

D.6.2 ch10

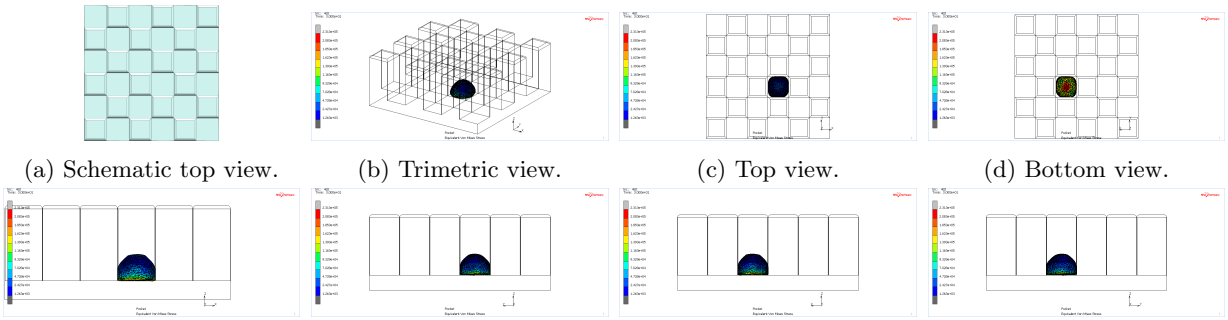

(a) Schematic top view. (b) Trimetric view. (c) Top view. (d) Bottom view.

(e) Front view. (f) Left view. (g) Back view. (h) Right view.

Figure D.42: Simulation results of the model in chessboard-like layout with 10×10 µm squares.

D.6.3 ch12

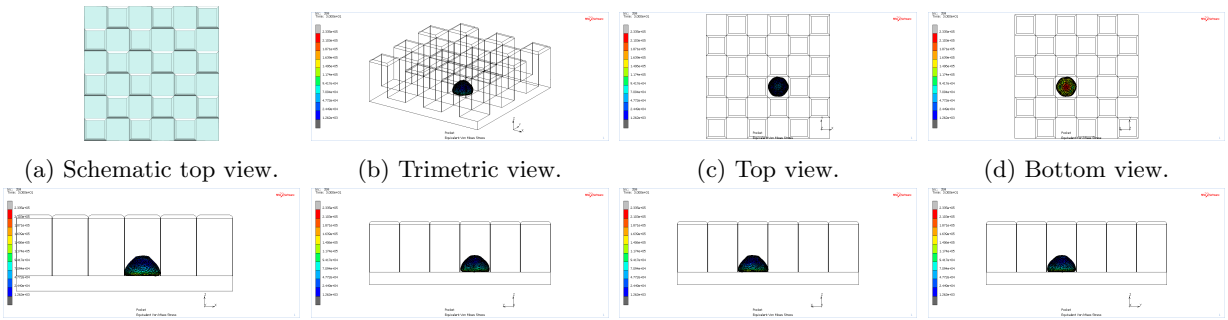

(a) Schematic top view. (b) Trimetric view. (c) Top view. (d) Bottom view.

(e) Front view. (f) Left view. (g) Back view. (h) Right view.

Figure D.43: Simulation results of the model in chessboard-like layout with 12×12 µm squares.

D.6.4 ch14

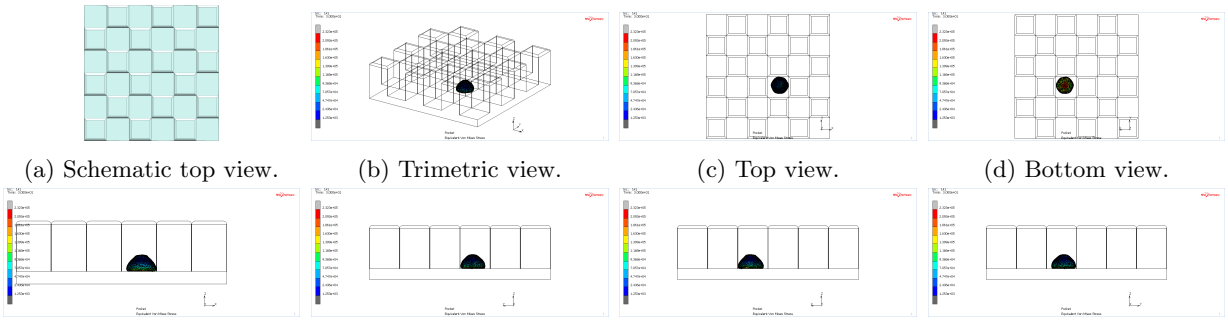

(a) Schematic top view. (b) Trimetric view. (c) Top view. (d) Bottom view.

(e) Front view. (f) Left view. (g) Back view. (h) Right view.

Figure D.44: Simulation results of the model in chessboard-like layout with 14×14 µm squares.

D.6.5 ch16

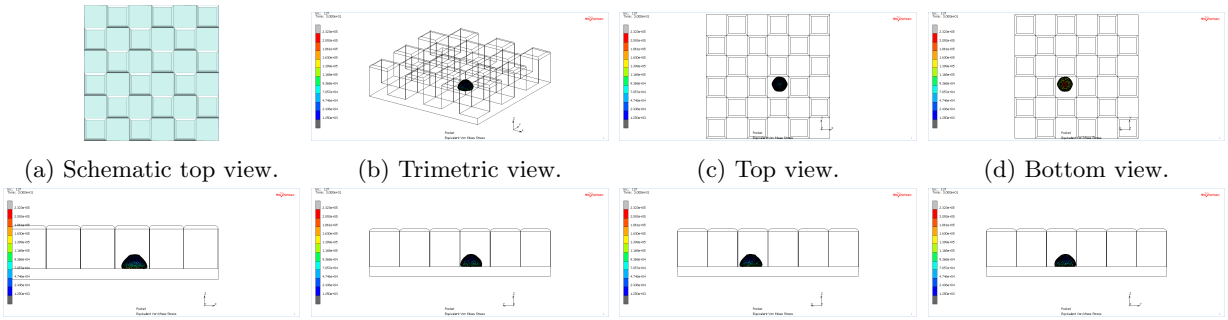

(a) Schematic top view. (b) Trimetric view. (c) Top view. (d) Bottom view.

(e) Front view. (f) Left view. (g) Back view. (h) Right view.

Figure D.45: Simulation results of the model in chessboard-like layout with 16×16 µm squares.

D.6.6 ch18

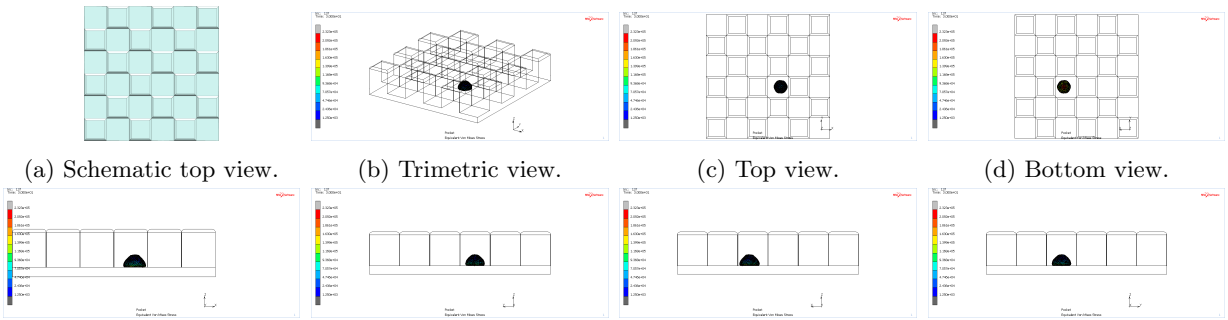

(a) Schematic top view. (b) Trimetric view. (c) Top view. (d) Bottom view.

(e) Front view. (f) Left view. (g) Back view. (h) Right view.

Figure D.46: Simulation results of the model in chessboard-like layout with 18×18 µm squares.

D.6.7 ch20

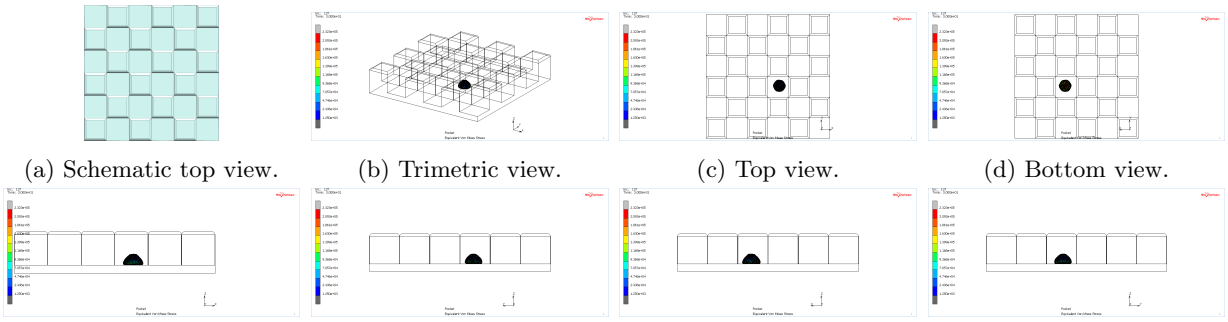

(a) Schematic top view. (b) Trimetric view. (c) Top view. (d) Bottom view.

(e) Front view. (f) Left view. (g) Back view. (h) Right view.

Figure D.47: Simulation results of the model in chessboard-like layout with 20×20 µm squares.